ADA058196

LEVEL II

AD

A037481

(12)

AMMRC TR 78-28

ELECTROSLAG REMELTING

June 1978
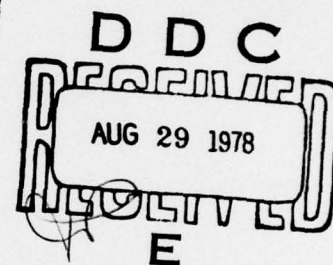
DDC
RECEIVED
AUG 29 1978
E

D. R. Poirier, S. Kou, T. Fujii, and M. C. Flemings

Massachusetts Institute of Technology
Cambridge, Massachusetts 02139

Final Report, Contract Number DAAG46-74-C-0120

Approved for public release; distribution unlimited.

Prepared for

ARMY MATERIALS AND MECHANICS RESEARCH CENTER
Watertown, Massachusetts 02172

78 08 28 039

The findings in this report are not to be construed as an official Department of the Army position, unless so designated by other authorized documents.

Mention of any trade names or manufacturers in this report shall not be construed as advertising nor as an official indorsement or approval of such products or companies by the United States Government.

(6) ELECTROSLAG REMELTING

Final Technical Report by

(10) D. R. Poirier, S. Kou, T. Fujii, and M. C. Flemings

Massachusetts Institute of Technology

Cambridge, Massachusetts   02139

(12) 127 p.   (11) Jun 78

(9) Final Technical Report, 1 Dec 74 - 30 Nov 77,

Contract Number DAAG46-74-C-0120, D/A Project

(15)

(16) 1L162105AH84

Approved for public release; distribution unlimited.

Prepared for

ARMY MATERIALS AND MECHANICS RESEARCH CENTER
Watertown, Massachusetts   02172

78 08 28 039

409 463

FOREWORD

This report was prepared by the Casting and Solidification Research Group in the Department of Materials Science and Engineering, Massachusetts Institute of Technology.   The report is entitled "Electroslag Remelting"; the contract was administered under the technical supervision of G. Bruggeman, R. H. Frost, and F. C. Quigley of the Army Materials and Mechanics Research Center, Watertown, Massachusetts.

TABLE OF CONTENTS

ABSTRACT

This report describes research on macrosegregation in ingots produced by the electroslag remelting (ESR) process. The work is on determining the severity of segregation in small experimental ingots, and comparing the segregation with calculations using macrosegregation theory.

Most experimental ingots were produced in an apparatus which simulates the solidification of an ESR ingot but does not employ slag. The unit comprises a source of melt droplets, a cooled mold, and a heat source to simulate the heat input of the ESR process. This apparatus was also modified so that rotation occurred during ingot solidification. In these studies ingots of Sn-15% Pb and Sn-12% Pb with a diameter of 8 cm were studied. In addition, results of experiments on an apparatus used to produce ingots of Al-4% Cu with a diameter of 7 cm are given. This apparatus consisted of a DC power source, a water cooled mold, consumable electrodes, and a slag layer as in conventional ESR processing.

Equations for predicting flow of interdendritic liquid and macrosegregation in ESR ingots are given and used in a computer model to numerically calculate the macrosegregation. Agreement between calculations and the experimental ESR ingots of Al-Cu and Sn-Pb alloys, described above, is excellent. The influence of important parameters such as the shape and depth of the mushy zone and the local solidification time on the macrosegregation across the ESR ingots is quantitatively demonstrated. The

important effect of the dimensionless group, $(\vec{v} \cdot \nabla T)/\varepsilon$, on the different types of macrosegregation observed is also discussed.

The most important finding is that the computer model can be modified to predict the effect of rotation on macrosegregation in ESR ingots and that prediction agrees with experiment.

Microsegregation theory and macrosegregation theory are applied to a multicomponent commercial steel. In this work, an ESR ingot of maraging steel of a cross-section, 20 cm x 20 cm, with rounded corners was studied.

Chapter I

INTRODUCTION

Background

The Casting and Solidification Research Group at the Massachusetts Institute of Technology has studied solidification of steel under Army Sponsorship for about seventeen years[1-13]. Since 1973 the casting work under Army Sponsorship has been directed to electroslag refining.[12,13]

Under this contract, an interim technical report[13] described a small scale ESR unit which was used to study macrosegregation in Al-4% Cu alloy. Results showed that severe-localized segregates, sometimes called "freckles" in large commercial ingots, could not be produced using this alloy cast in the small-scale ESR molds. Modest segregation in the form of surface to center compositional variations were produced, however, enabling a comparison of experiment and calculations using macrosegregation theory. In order to study more severe segregation, a simulated ESR apparatus was built and used to cast Pb-15% Sn alloy. The interim report described initial experiments which were very successful. In these initial experiments, it was shown that not only a wide variation in surface to center composition could be produced on a laboratory scale but also "freckles" were readily formed. There was also excellent agreement between calculations of macrosegregation and the macrosegregation in these experimental ingots. With these encouraging results, work continued using tin-lead alloys as a model alloy which was cast in the simulated ESR apparatus.

This final report summarizes that work presented in the interim report[13] along with the results on subsequent small-scale ingots including a number of ingots which were rotated during solidification. In addition to the experiments, a number of computer calculations were carried out which 1) enabled comparison of experiment and theory and 2) predicted the effects of rotation, alloy density variations, and thermal parameters on macrosegregation and minimizing macrosegregation. All of these results are described in Chapters II and III of this report which are comprised of two papers to be published individually, elsewhere.[14,15]

This report also includes a third phase of our macrosegregation studies which is reported in Chapter IV. In Chapter IV, the structure of an ESR ingot of maraging steel produced at AMMRC is studied with emphasis on segregation. Macrosegregation theory is extended to treat the multicomponent alloy to demonstrate the application of macrosegregation theory to a larger size ingot than could be produced in the laboratories at the Massachusetts Institute of Technology.

Overview of Experimental Work

Subsequent chapters give details of each of the various types of experimental ingots produced under this contract. Here we discuss only one of the apparati employed as an example of the basic approach throughout the program.

An apparatus employed is one which simulated solidification behavior of the ESR process but did so without a consumable electrode or slag. This unit was comprised of a source of molten metal droplets, a cooled mold, and a heat source to simulate ESR heat input, Figure 1. This unit was used for experimental work on a Sn-15% Pb alloy.

In this apparatus, liquidus and solidus shape and movement could be varied significantly and made to closely simulate the behavior of actual ESR ingots. For example, Figure 2a shows the shapes of isotherms during solidification of an ingot of Sn-15% Pb. In the ingot, significant segregation was found. Figure 2c shows that the segregation varied from about 11% at the surface to 28% in the center. In other ingots of Sn-15% Pb the segregation was significantly severe that gross segregation, commonly called "freckles" formed.

Overview of Analytical Work

An underlying concept of this work is that macrosegregation, such as that shown in Figure 2c, can be understood and quantitatively analyzed using theories developed at M.I.T. over the last decade.[16-22] The cause of the segregation is the slow creeping flow of liquid between dendrite arms; that flow is driven primarily by 1) gravity induced convection, and 2) solidification shrinkage.

In this work, the basic equations, developed earlier, were applied to the ESR process and computer analyses developed to solve for the fluid

flow and resulting segregation behavior in ESR ingots. As *examples* of the computer output, Figure 2b shows the calculated interdendritic fluid flow in the ingot referred to earlier. With flow curves such as those of Figure 2b, calculations of macrosegregation were readily made. Figure 2c compares the experimental results of the Sn-15% Pb ingot with theory. Agreement is excellent considering the large number of variables in the complex segregation process. Detailed discussion is given in this report of comparison between experiment and theory, as well as of the choice of the adjustable parameter, the "permeability", of the mushy zone.

In addition to the comparison of theory with experiment described above, it should be noted that the macrosegregation theory predicts when "freckles" appear, and this theory correctly predicts the presence of the freckles in several ingots which are discussed in Chapters II and III of this report.

REFERENCES

1.   M. C. Flemings, R. V. Barone, S. Z. Uram, H. F. Taylor,
     "Solidification of Steel Castings and Ingots", Trans. AFS, v. 69,
     1961, pp. 422-435.

2.   G. E. Nereo, R. F. Polich, M. C. Flemings, "Unidirectional
     Solidification of Steel Castings", Trans. AFS, v. 73, 1965,
     pp. 1-13.

3.   R. F. Polich, M. C. Flemings, "Mechanical Properties of Unidirectional
     Steel Castings", Trans. AFS, v. 73, 1965, pp. 28-33.

4.   T. Z. Kattamis, M. C. Flemings, "Dendrite Morphology, Microsegregation
     and Homogenization of Low Alloy Steel", Trans. Met. Soc. AIME, v. 233,
     1965, pp. 992-999.

5.   "Casting Process and Apparatus for Obtaining Unidirectional
     Solidification", Patent No. 3,204,301, M. C. Flemings, H. F. Taylor,
     October 24, 1960.

6.   M. C. Flemings, "Directional Solidification and Composite Structures",
     Surfaces and Interface II, Ed. J. Burke et al., Syracuse University
     Press, 1968, pp. 313-352.

7.   L. K. Bigelow, M. C. Flemings, "Sulfide Inclusions in Steel", U.S.
     Army Materials and Mechanics Research Center, Contract No.
     DAAG46-68-C-0043, Report for the period January 1, 1968 to December
     31, 1969.

8.   M. Myers, M. C. Flemings, "Behavior of Silica Inclusions during
     Solidification of an Iron Base Alloy", U.S. Army Materials and
     Mechanics Research Center, Contract No. DAAG46-68-C-0044, Final Report
     for the period January 1, 1968 to December 31, 1969.

9.   D. S. Gnanamuthu, M. Basaran, T. Z. Kattamis, R. Mehrabian, M. C.
     Flemings, "Investigation of Solidification of High Strength Steel",
     U.S. Army Materials and Mechanics Research Center, Contract No.
     DAAG46-68-C-0043, Report for the period January 1, 1970 to December
     31, 1970.

10. D. S. Gnanamuthu, M. Basaran, T. Z. Kattamis, R. Mehrabian, M. C.
     Flemings, "Investigation of Solidification of High Strength Steel",
     U.S. Army Materials and Mechanics Research Center, Contract No.
     DAAG46-68-C-0043, July 1972.

11.   E. F. Fascetta, T. Z. Kattamis, R. Mehrabian, M. C. Flemings, "Investigation of Solidification of High Strength Steel", U.S. Army Materials and Mechanics Research Center, Contract No. DAAG46-68-C-0043, October 1973.

12.   M. Basaran, T. Z. Kattamis, R. Mehrabian, M. C. Flemings, "A Study of the Heat and Fluid Flow in Electroslag Remelting", U.S. Army Materials and Mechanics Research Center, Contract No. DAAG46-73-C-0088, April 1974.

13.   D. R. Poirier, S. Kou, R. Furlong, and M. C. Flemings, "Electroslag Remelting", U.S. Army Materials and Mechanics Research Center, Contract No. DAAG46-74-C-0120, Interim Technical Report, December 1976.

14.   S. Kou, D. R. Poirier, M. C. Flemings, "Macrosegregation in Electroslag Remelted Ingots", to be published in Proceedings of the Electric Furnace Conference, Iron and Steel Society of AIME, December 1977.

15.   S. Kou, D. R. Poirier, M. C. Flemings, "Macrosegregation in Rotated Electroslag Remelted Ingots", submitted for publication to Met. Trans.

16.   M. C. Flemings, G. E. Nereo, "Macrosegregation, Part I", Trans. Met. Soc. AIME, v. 239, 1967, pp. 1449-1461.

17.   M. C. Flemings, R. Mehrabian, G. E. Nereo, "Macrosegregation, Part II", Trans. Met. Soc. AIME, v. 242, 1968, pp. 41-49.

18.   M. C. Flemings, G. E. Nereo, "Macrosegregation, Part III", Trans. Met. Soc. AIME, v. 242, 1968, pp. 50-55.

19.   R. Mehrabian, M. C. Flemings, "Macrosegregation in Ternary Alloys", Met. Trans., v. 1, 1970, pp. 455-464.

20.   R. Mehrabian, M. A. Keane, M. C. Flemings, "Interdendritic Fluid Flow and Macrosegregation; Influence of Gravity", Met. Trans., v. 1, 1970, pp. 1209-1220.

21.   R. Mehrabian, M. A. Keane, M. C. Flemings, "Experiments on Macrosegregation and Freckle Formation", Met. Trans., v. 1, 1970, pp. 3238-3241.

22.   M. A. Keane, Sc.D. Thesis, Department of Materials Science and Engineering, Massachusetts Institute of Technology, 1973.
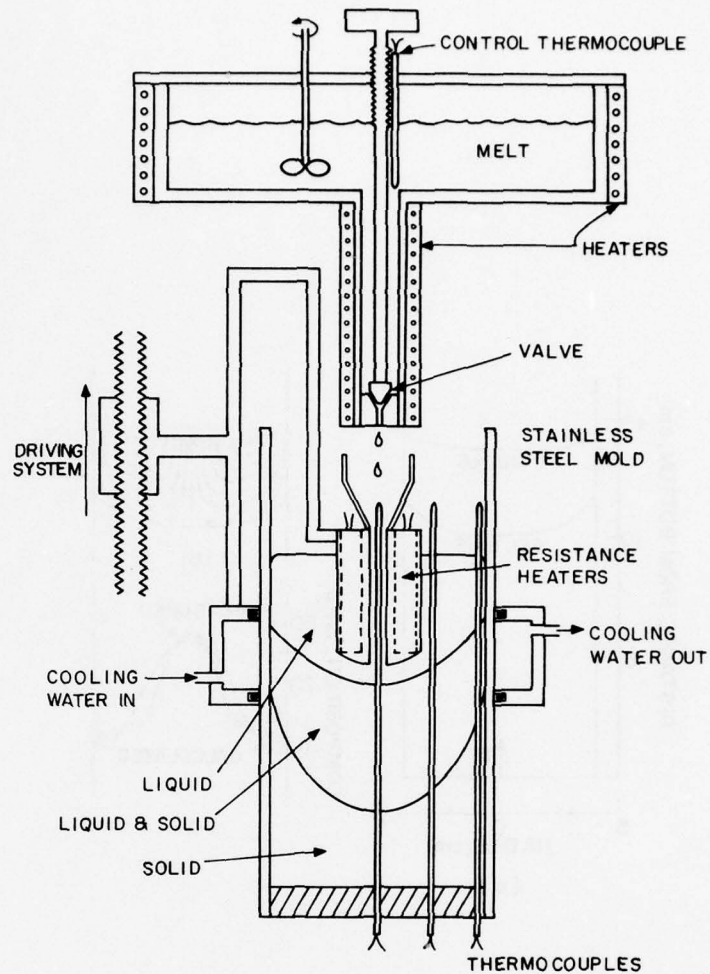
Figure 1-1:   Apparatus used as an analog ESR process to produce
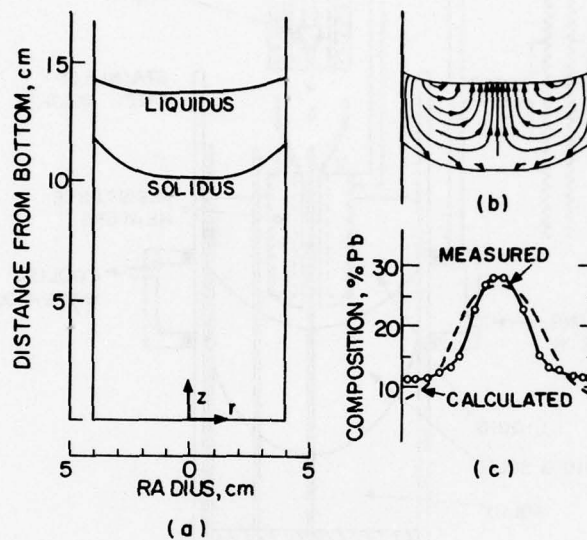Sn-15%Pb ingots.

Figure 1-2: Results obtained for ingot of Sn-15% Pb.
(a) Liquidus and solidus isotherms; (b) flow
lines of interdendritic liquid; (c) macro-
segregation as measured (solid curve) and
calculated (broken curve).

Chapter II

MACROSEGREGATION IN ELECTROSLAG REMELTED INGOTS

This Chapter will be published as part of the Proceedings of the
Electric Furnace Conference, Iron and Steel Society of AIME, December 1977.

Abstract

Equations for predicting flow of interdendritic liquid and
macrosegregation in ESR ingots are derived, and a computer model based on
these equations is used to numerically calculate the macrosegregation.
Agreement between calculations and experimental results is excellent.
Experiments are on simulated ESR ingots of Al-Cu and Sn-Pb alloys. The
influence of the important solidification parameters such as the shape and
depth of the mushy zone and the local solidification time on the
macrosegregation across the ESR ingots is quantitatively demonstrated.
The important effect of the dimensionless group, $(\vec{v}\cdot\nabla T)/\varepsilon$, on the different
types of macrosegregation observed is also discussed.

INTRODUCTION

Theoretical heat flow models have been developed to relate the operating parameters in the ESR process to solidification parameters such as shape and depth of the mushy zone and the solidification rate[1-3]. However, quantitative studies have not been done for ESR ingots on how these solidification parameters in turn affect macrosegregation. In this paper, we derive equations for quantitatively predicting macrosegregation in ESR ingots. Based on these equations, a computer model is then employed to predict macrosegregation from measured solidification parameters.

The basic concept employed is that macrosegregation in ESR ingots is caused by interdendritic fluid flow, as described earlier for other types of ingots by Flemings and Nereo[4], and by Mehrabian, Keane and Flemings[5]. In the latter work, equations were derived for the pressure distribution, and hence interdendritic flow, inside the planar mushy zone of a unidirectionally solidifying ingot, using D'Arcy's Law for the interdendritic fluid flow, and taking both gravity and solidification shrinkage as driving forces for the flow. A simplified, and somewhat approximate method was used for solving these interdependent equations. In this paper, we (1) simultaneously solve the relevant equations more exactly, and (2) describe the pressure distribution, flow behavior, and macrosegregation in cylindrical coordinates for the conditions of solidifying ESR ingots.

A schematic summary of the analytic work to be described herein is given in Figure 1. Figure 1a shows an ESR ingot during solidification. Liquidus and solidus isotherms are presumed known by calculation, or by thermal measurement. Properties of the semisolid alloy are known (density, solidification shrinkage, etc.) so interdendritic flow behavior can be calculated, as shown in Figure 1b. Solidification theory is then employed to calculate macrosegregation, as shown in Figure 1c. More precisely, as noted in the previous paragraph, the equations for flow behavior and segregation must be solved simultaneously.

Finally, it should be emphasized that although macrosegregation in the ESR processes is analyzed in this study, the basic equations can be equally applied to other casting processes such as continuous casting, VAR process, etc.

ANALYSIS OF MACROSEGREGATION

Within the mushy zone, we apply the local solute redistribution
equation, previously given by Flemings and Nereo[4], to account for the
partitioning of solute which takes place during dendritic freezing of a
volume element of alloy in the mushy zone. That equation is:

$$\frac{\partial g_L}{\partial t} = -\left(\frac{1-\beta}{1-k}\right)\left(1 + \frac{\vec{v}\cdot\nabla T}{\epsilon}\right)\left(\frac{g_L}{C_L}\right)\left(\frac{\partial C_L}{\partial t}\right) \tag{1}$$

where β is the solidification shrinkage, k is the equilibrium partition
ratio, ϵ is the cooling rate, C_L is the liquid composition, T is the
temperature, $\vec{v}$ is the velocity of interdendritic liquid, g_L is volume
fraction liquid, and t is time. The convection of the interdendritic
liquid is according to D'Arcy's Law, as applied to a dendritic structure
by Mehrabian et al[5], with the specific permeability, K, given as

$$K = \gamma g_L^2 \tag{2}$$

where γ is a constant. The equation of continuity in the mushy zone
combined with D'Arcy's Law is

$$\nabla \cdot \left(\frac{K\rho_L}{\mu}\nabla P + \frac{K\rho_L^2 g\vec{z}}{\mu}\right) = \left(\rho_L - \rho_S\right)\left(\frac{\partial g_L}{\partial t}\right) + g_L\left(\frac{\partial \rho_L}{\partial t}\right) \tag{3}$$

where ρ_S and ρ_L are the densities of solid and liquid, P is pressure,
μ is viscosity of the interdendritic liquid, g is acceleration due

to gravity, and $\vec{z}$ is the unit vector in the vertical direction. In Equation (3) ρ_S is assumed constant and, for the alloys considered herein, this assumption is reasonable (e.g., see Figure 2).

In the "local solute redistribution equation", it is assumed that equilibrium exists at the interface between the interdendritic liquid and the solid phase[4]. Therefore, the temperature of a solidifying alloy is dictated by the liquidus line on the corresponding phase diagram, and the composition of interdendritic liquid is a function of temperature only, so

$$\frac{\partial C_L}{\partial t} = \left(\frac{dC_L}{dT}\right)\left(\frac{\partial T}{\partial t}\right) = \frac{\varepsilon}{m} \tag{4}$$

and

$$\frac{\partial \rho_L}{\partial t} = \left(\frac{d\rho_L}{dC_L}\right)\left(\frac{\partial C_L}{\partial t}\right) = \left(\frac{d\rho_L}{dC_L}\right)\frac{\varepsilon}{m} \tag{5}$$

where m is the slope of the liquidus on the phase diagram.

Substituting Equations (1), (2), (4) and (5) into Equation (3), and then expanding it into cylindrical coordinates, we get the following equation for pressure distribution:

$$\frac{\partial^2 P}{\partial r^2} + \frac{\partial^2 P}{\partial z^2} + A\frac{\partial P}{\partial r} + B\frac{\partial P}{\partial z} + C = 0 \tag{6}$$

where A, B and C are defined as follows:

$$A = \frac{1}{r} + \frac{2}{g_L}\frac{\partial g_L}{\partial r} + \frac{1}{\rho_L}\frac{\partial \rho_L}{\partial r} + \alpha\left(\frac{\partial C_L}{\partial r}\right),$$

$$B = \frac{2}{g_L}\frac{\partial g_L}{\partial z} + \frac{1}{\rho_L}\left(\frac{\partial \rho_L}{\partial z}\right) + \alpha\left(\frac{\partial C_L}{\partial z}\right),$$

$$C = g\rho_L\left[\frac{2}{g_L}\frac{\partial g_L}{\partial z} + \frac{2}{\rho_L}\frac{\partial \rho_L}{\partial z} + \alpha\left(\frac{\partial C_L}{\partial z}\right)\right] - \frac{\varepsilon\mu}{m\gamma g_L}\left[\frac{1}{\rho_L}\frac{d\rho_L}{dC_L} + \alpha\right]$$

with

$$\alpha = \frac{\beta}{(1 - k)C_L} \quad .$$

The boundary conditions are shown in Figure 3. Since the mold wall is impermeable, $v_r = 0$ at the wall, and at the centerline, $v_r = 0$ because of symmetry. At the solidus isotherm the boundary condition satisfies continuity of the solidifying eutectic liquid[4,5]; v_r and v_z are the velocity components of the eutectic liquid, U_{Er} and U_{Ez} are the velocity components of the solidus isotherm (eutectic temperature), and ρ_{SE} and ρ_{LE} are the densities of eutectic solid and liquid, respectively. Within the bulk liquid pool, we assume no convection; P_0 is the pressure at the top of the liquid pool, ρ_{LO} is the density of the bulk liquid, and h is the height of the liquid pool.

Calculation of Macrosegregation

From the measured shape of mushy zone, temperature distribution in the mushy zone, solidification rate and cooling rate, all the unknown

variables (except g_L) involved in A, B and C of Equation (6) can be determined with the help of a phase diagram and a density versus liquid composition diagram (e.g., Figure 2). To initiate calculations g_L is approximated using the Scheil Equation (i.e., Equation (1) with β and $\vec{v}$ equal to zero). Now, with the boundary conditions given in Figure 3, Equation (6) can be solved for the pressure distribution in the mushy zone. Once the pressure distribution is known, the velocity of interdendritic liquid in the mushy zone is calculated using D'Arcy's Law. With the obtained velocity distribution, we integrate Equation (1) to obtain new values of g_L which are substituted into A, B and C to recalculate a new pressure and velocity distribution. This procedure is repeated until g_L stops changing. This final g_L distribution is the correct one. Finally, with this correct g_L distribution in the mushy zone, the local average composition, $\bar{C}_S$, can be calculated by using Equation (25) presented in Flemings and Nereo[4].

Results of calculations using this procedure are compared with experiments on laboratory-scale ESR apparati which are described below.

APPARATUS AND EXPERIMENTAL PROCEDURE

Two different types of experimental apparatus were employed and these are each described below. The first (employed for Al-4% Cu alloy) is a small scale ESR unit. This unit is comprised of a DC power source, a water cooled mold, a consumable electrode, and slag layer as in conventional ESR, Figure 4.

The second type of apparatus employed is one which simulates the solidification behavior of the ESR process, but does not employ slag. This unit, used for Sn-15% Pb alloy, comprises a source of molten alloy drops, a cooled mold, and a heat source to simulate the heat input of the ESR process, Figure 5.

Small Scale ESR Units

A sketch of the apparatus is shown in Figure 4. The power supply is a D.C. arc-welder capable of providing up to 1600 amp and 40 volts for a total power of 55 KW. The electrode mount is connected to a feed screw about 6 feet long which is driven by one of two gear reduction boxes in series with an electric motor. The driving speed of the electrode can be controlled and operated with a speed in the range of 0.2 - 14 cm/min. The electrodes used were aluminum alloy 2024, 1 inch in diameter by 6 feet long.

The dimensions of the copper mold were 3 inches in diameter by 9 inches high. A thin wash of graphite powder or alumina powder was applied to the mold wall in order to avoid the attack of the mold by the slag (45% LiCl - 55% KCl). Two mold designs were used; the better of the two is shown in Figure 6. With this design it was easy to replace the mold wall whenever the mold failed due to the slag attack. It was also convenient to insert up to 5 thermocouples into the ingot during a run.

About 250 c.c. of liquid slag of eutectic composition (45 wt% LiCl and 55 wt% KCl) was poured into the mold, and melting was initiated with a power of 10 KW. The cooling water was turned on, and then the power was lowered to between 2 and 4 KW. The amperage was kept constant by adjusting the driving speed of the electrode, and the electrode position was recorded during a run. When thermal data were obtained, five chromel-alumel thermocouples were inserted into the mold and pushed to predetermined positions (shown as X's in Figure 6) immediately after the electrode passed these positions.

Cooling curves were used to determine the shape of mushy zone, temperature distribution, cooling rates and solidification rates. Thermal data for two ingots (Nos. 1 and 2) were obtained with the mold shown in Figure 6.

Ingot No. 3 was made in a mold in which cooling water ran through an annulus. No thermal data were measured, but instead this

- 20 -

ingot was doped with about five grams of Al-50% Cu to reveal the liquid pool shape.

Simulated ESR Apparatus

A sketch of the apparatus is shown in Figure 5. The stainless steel mold is 3-1/4 inches in diameter and 13 inches long. The metal pool inside the mold is heated with six, 3 inch long, resistance heaters connected in parallel. These heaters are positioned inside holes drilled into a 3 inches long by 1-1/4 inches diameter stainless steel bar. Power input is controlled with a transformer.

Cooling water runs through a movable cooling jacket surrounding the mold. Both the resistance heaters and the cooler are fixed to the same system used for driving the electrodes in making the Al-4% Cu ingots. Thermal measurements are made with three chromel-alumel thermocouples located inside three vertical stainless steel tubes. The tubes are fixed, but the position of the thermocouples is varied during a run by sliding them up and down inside the tubes.

Flow of liquid from the top container is controlled by an adjustable valve. Heating of the melt in the top container is done with two 1.5 inch wide band heaters which are controlled by a thermocouple hooked up with a temperature controller. A stirrer was used to insure uniform temperature and composition in the liquid supply.

Tin (99.9%) and lead (99.9%) were melted and well stirred in a crucible furnace. About one-fourth of the charge was poured into the stainless steel mold until the liquid level rose to almost the top of the resistance heaters (about 3.5 inches from the bottom of the mold). The remaining alloy was then poured into the top container. With the resistance heaters and the cooling jacket fixed, the initial position and the shape of the mushy zone were determined by moving the three thermocouples up and down and locating the positions of the liquidus and solidus temperatures of the alloy. Power input to the heaters and the position of the cooling jacket were adjusted until the desired position and shape of mushy zone were obtained.

Chemical Analysis

Chemical analysis of macrosegregation in the ingots was by X-ray fluorescence. A General Electric X-ray diffraction unit (Model XRD 3, Type 1) was used with a Mo tube. The primary white radiation from the tube fluoresced the samples on an area of 0.32 cm. diameter. This area covered many dendrite arms (secondary dendrite arm spacing is about 30 - 70μ) and, therefore, the compositions measured were local average compositions.

The secondary radiation from the sample was received by a Si (Li) X-ray detector and the intensity of the characteristic line (K_α for Cu and L_α for Pb) was compared with a standard intensity versus composition curve to determine the composition.

Standards were prepared from rapidly cooled thin sections of known compositions. The Al-Cu standards used were those prepared by Nereo[6]. The Pb-Sn standards were prepared by melting lead and tin together in a graphite crucible. About 5 grams of the liquid alloy was quickly removed from the crucible and dropped 1.5 feet onto a copper chill; the alloy solidified very rapidly as a splat. The central portion of the splat was similar to a thin disk (about 0.8 mm thick and 2 inches in diameter) with a very smooth and flat bottom surface. A rectangular plate (0.8 inch x 1.2 inches) was cut from the disk and polished with 600 grit metallographic paper for x-ray fluorescence. The remainder of the disk was analyzed by wet chemical analysis to serve as a standard.

RESULTS

Results of experiments and calculations are given first for the Al-4% Cu ingots as a group and then for the Sn-15% Pb ingots. It will be seen that considerably more segregation was achieved in the Sn-Pb ingots, and severe localized segregates (freckles) were readily obtained.

Aluminum-4% Copper Ingots

In Ingot 1, cooling curves were obtained from five thermocouples and used to construct the shape of the mushy zone at various times. After 6 minutes an approximate steady state was achieved, and the isotherms moved with a vertical speed of 0.053 cm/s; the liquidus and solidus are shown in Figure 7a at a time of 7 minutes after starting. Cooling rate did not vary with radius, and so the isotherms are parallel. This was also verified by measurements of dendrite cell size, $\bar{d}$, across the ingot; $\bar{d}$ is 61 microns with no variation. Figure 7c shows the macrosegregation; the overall analysis of the ingot is 4.4% Cu with positive segregation at the surface (4.6% Cu) and negative segregation at the centerline (4.25% Cu). Macroetching showed no evidence of localized segregates, such as "freckles" or "V"-segregates.

Calculations of flow lines (Figure 7b) and macrosegregation (Figure 7c) were done using the phase diagram and density data for the aluminum-copper system as given in Mehrabian et al[5]. The value of

viscosity used was 1.3 centipoise[7,8]. The value of γ used is 5×10^{-7} cm^2. This value of γ is of the same magnitude used by Mehrabian et al.[5] to obtain the best fit between their theoretical and experimental results of macrosegregation in Al-4.5% Cu ingots.

Flow is predominantly down and outwards, Figure 7b, and so segregation, calculated and observed, is negative at the center, Figure 7c.

Ingot 2 was cast in the same manner as Ingot 1 with the exception that an unusually thick (about 3 mm) coating of mold wash (graphite and powdered zirconia) was applied to the inside mold wall. As a result, cooling curves showed that isotherms were flat, and so solidification was unidirectional. Cooling rate during solidification was about equal to that observed in Ingot 1, and consequently dendrite cell size is also equal (61μ). Since solidification was unidirectional, no macrosegregation was detected in this ingot; nor was there any evidence of localized segregates found in an etched macrosection.

Thermal data for Ingot 3 were not measured, but with isotherm shape obtained by doping, as described earlier, the thermal history was constructed with a knowledge of the electrode melting rate and cooling rate (calculated from dendrite cell sizes) as shown by Mellberg and Sandberg[20]. The isotherm was not exactly symmetrical because the electrode was not centered exactly; however for calculations we assume

a symmetrical mushy zone (Figure 8a). The width of the mushy zone (vertical distance between the solidus and liquidus) is constant since cooling rate was also independent of radius as indicated by a constant dendrite cell size (61 microns) across the ingot.

The degree of macrosegregation for Ingot 3 is shown in Figure 8b. The extent of segregation is less than that of Ingot 1. Calculations with $\gamma = 3 \times 10^{-7}$ cm^2 agree remarkably well with experiment except that the minimum point in the experimental curve is off-center.

Sn-15% Pb Ingots

Ingots 4, 5 and 6 were produced in the apparatus shown in Figure 5. Figure 9a shows the shape of the mushy zone at 25 minutes in Ingot 4. At steady state, the isotherms moved with a vertical speed of 4.0×10^{-3} cm/s (about one order of magnitude less than that obtained in the Al-4% Cu ingots).

Macrosegregation is pronounced, Figure 9c. Composition varies from 11% Pb at the surface to 28% Pb at the center of the ingot. Although segregation is severe, microstructures show no evidence of freckles.

In this ingot, as well as in Ingots 5 and 6, the width of the mushy zone and the cooling rate vary from center to surface. This is seen in Figure 10 which shows a decrease in the secondary dendrite arm spacing from the center to the surface. Our calculations take into account this variation by making permeability (and, hence, γ) a function of the secondary dendrite arm spacing. Data of Streat and Weinberg[13] show that permeability varies with square of secondary dendrite arm spacing, d, for 25 < d < 60 microns. Accordingly, we select a value of γ at the centerline (γ_o) and vary γ according to

$$\gamma/\gamma_o = (d/d_o)^2 . \qquad (7)$$

Calculations of flow lines and macrosegregation are shown in Figures 9b and 9c, respectively. For calculations, the value of viscosity used was 2.2 centipoises.[10] With $\gamma_o = 3.7 \times 10^{-6}$ cm^2, the calculated result of macrosegregation agrees reasonably well with experiment. Since permeability in lead-rich Pb-Sn alloys[13] is reported to be $10^1 - 10^2$ greater than the value of permeability for aluminum alloys[11,12], it is reasonable that γ is on the order of 10^{-6} cm^2 assuming similar behavior of tin-rich and lead-rich Sn-Pb alloys.

The calculated flow pattern, shown in Figure 9b, shows that gravity has a very strong effect on the flow, causing the interdendritic liquid to flow from the surface towards the ingot center and up near the

center resulting in positive segregation in the center of the ingot. It will be seen that such flow (from "cold" to "hot" regions in the mushy zone), when sufficiently strong, leads to localized channels of increased flow and the formation of freckles.

For Ingot 5, the shape of the mushy zone at 14 minutes is constructed in Figure 11a. After 4 minutes steady state was achieved, and the isotherms moved with a vertical speed of 7.0×10^{-3} cm/sec.

In this ingot the resulting macrosegregation across the ingot is pronounced (Figure 11c). The composition ranges from 8% Pb at mid-radius to 28% Pb at the center of the ingot. Microstructures are shown in Figure 12; "freckles" are evident in Figures 12b and c.

A value of γ_o was selected by using the best value determined for Ingot 4 ($\gamma_o = 3.7 \times 10^{-6}$ cm^2) and adjusting for the decrease in secondary arm spacing at the centerline (Figure 10). This gives $\gamma_o = 2.4 \times 10^{-6}$ cm^2. Flow calculations show that $(\vec{v} \cdot \nabla T/\epsilon) < -1$ in equation (1), and hence $(\partial g_L/\partial C_L) > 0$ in these regions of the ingot. This phenomenon is discussed in more detail below. Essential points are that, when $\vec{v} \cdot \nabla T/\epsilon < -1$, (a) "freckles" can form, and (b) our method of quantitatively calculating macrosegregation is no longer valid.

Figure 11b shows calculated flow lines with permeability decreased to the point that their directions are observed just at the

onset of developing a flow instability. With $\gamma_o = 2.0 \times 10^{-7}$ cm^2, $(\vec{v} \cdot \nabla T / \varepsilon) > -1$ throughout the entire mushy zone. With permeability decreased by almost one order of magnitude, the flow is still towards the centerline and upwards at the center. Flow is strongly enhanced in Ingot 5 over that in Ingot 4, because the isotherms in the mushy zone are significantly deeper; this difference is apparent in Figures 9a and 11a. With $\gamma_o > 2.0 \times 10^{-7}$ cm^2, the flow is stronger than indicated in Figure 11b, and the formation of freckles is predicted as observed in Figure 12.

In Ingot 6, steady state solidification was achieved after 21 minutes, when the isotherms moved with a vertical speed of 6.3×10^{-3} cm/s. Secondary dendrite arm spacings are shown in Figure 10 where it is seen that this ingot solidified with the slowest cooling rate among the three Sn-15% Pb ingots.

The shape of mushy zone at 23 minutes is plotted in Figure 13a. Macrosegregation is shown in Figure 13c. As in Ingots 4 and 5 the extent of macrosegregation across the ingot is severe; composition varies from 11.5% Pb at the edge of the ingot to 38% Pb (eutectic composition) at the center of the ingot. The general region of the center-line comprises a big channel or "freckle"; other areas show no evidence of freckling.

- 29 -

As with Ingot 5, when permeability is selected to correspond
to the dendrite arm spacing in Figure 10 ($\gamma_o = 4.4 \times 10^{-6}$ cm^2),
calculations indicate $(\vec{v} \cdot \nabla T/\varepsilon) < -1$ in the central regions of the ingot
predicting the formation of a freckle. The flow lines shown in Figure
13b are calculated using $\gamma_o = 8 \times 10^{-7}$ cm^2; with greater values, the
instability develops. Figure 13b, however, does indicate that the overall
interdendritic flow is similar to that observed in Ingots 4 and 5.
Macrosegregation in Ingot 6 is more severe than in Ingot 5 because the
local solidification time is significantly greater (Figure 10).

DISCUSSION

Both the Al-Cu and Sn-Pb alloy studied (1) have a segregation
ratio k less than one and (2) have an interdendritic liquid that increases
progressively in density during solidification. Hence, in ingots with a
concave mushy zone, both exhibit negative segregation at the ingot
centerline when interdendritic fluid flow is primarily influenced by
feeding, and both exhibit positive segregation when gravity forces
predominate.

In this experimental study, the Al-Cu ingots showed negative
segregation while the Sn-Pb ingots showed positive segregation at the
centerline. This is because the Al-Cu ingots were made at much greater
vertical solidification rate (10 times) and with a smaller value of
permeability in the mushy zone than were the Sn-Pb ingots - both
factors which reduce the influence of gravity on interdendritic flow.

This effect of vertical solidification rate and depth of
mushy zone in macrosegregation is illustrated in Figure 14. Here,
macrosegregation has been calculated in Al-4.4% Cu ESR ingots of
geometry studied in this work, for different solidification conditions.
Calculated flow lines and macrosegregation are shown for two different
vertical solidification rates and for mushy zones of three different
degrees of concavity (i.e., three different "depths" where depth refers

to distance from the highest to the lowest point in the mushy zone).
Note that macrosegregation increases with increasing depth of mushy
zone. At the higher solidification rate (smaller local solidification
time) it is negative at the centerline and at the slower solidification
rate it is positive at the centerline. At these slower solidification
rates, gravity causes the interdendritic flow lines to curve inwards and
upwards near the center (Figures 14e and f).

According to macrosegregation theory[4,5], the important
dimensionless parameter affecting macrosegregation is $\vec{v} \cdot \nabla T/\varepsilon$. When
this is equal to $\beta/1 - \beta$ no macrosegregation results; when it is greater,
segregation is negative and when it is less, segregation is positive.
Figure 15a shows a plot, for Ingot 1, of $\vec{v} \cdot \nabla T/\varepsilon$ at the centerline
during solidification (i.e., as C_L increases from C_O to C_E). $\vec{v} \cdot \nabla T/\varepsilon$
is greater than $\beta/1 - \beta$ throughout solidification, resulting in a lower
composition of solid forming at any time during solidification than
would form in the absence of segregation (Figure 15b). Hence
segregation is negative here.

Figure 16 is a plot similar to that of Figure 15 in all
respects except that here $\vec{v} \cdot \nabla T/\varepsilon$ is less than $\beta/1 - \beta$ and so segrega-
tion is positive. This plot applies to the centerline of Ingot 4.

Note in Ingot 4 that $\vec{v} \cdot \nabla T/\varepsilon$ is never less than -1. At the
critical point where this occurs, flow velocity in the direction of

isotherm movement is greater than velocity of isotherms and "remelting" occurs. This is the criterion for formation of freckles[5]. $\vec{v} \cdot \nabla T / \varepsilon$ was calculated to be less than -1 in Ingots 5 and 6, and here, as expected and shown in Figure 12, "freckles" (channel type segregates) were observed.

CONCLUSIONS

1.   Calculations which predict macrosegregation in ESR ingots compare
     well with experimental results. The calculated interdendritic
     fluid flow patterns clearly demonstrate the influence of
     solidification shrinkage and gravity on the observed macrosegre-
     gation across experimental ESR ingots.

2.   The effects on macrosegregation of the important solidification
     parameters such as the depth of the mushy zone, the vertical
     solidification rate, and the width of the mushy zone on
     macrosegregation in ESR ingots can be quantitatively evaluated.

3.   The computer model developed predicts the conditions which cause
     the formation of "freckles".

REFERENCES

1. R. C. Sun, J. W. Pridgeon, Union Carbide Corporation, Materials Systems Division, Technology Department, Kokomo, Indiana, September 1969, Report No. 7649.

2. A. Mitchell, S. Joshi, Met. Trans., v. 4 (1973), pp. 631-642.

3. B. Z. Paton, et al., Fifth International Symposium on ESR Process, October 1974, pp. 323-344.

4. M. C. Flemings, G. E. Nereo, Trans. Met. Soc. AIME, v. 239 (1967), pp. 1449-1461.

5. R. Mehrabian, M. Keane, M. C. Flemings, Met. Trans., v. 1 (1970), pp. 1209-1220.

6. G. E. Nereo, Sc.D. Thesis, Department of Metallurgy, Massachusetts Institute of Technology (1966).

7. E. Rothwell, J. Inst. Metals, v. 90 (1961/1962), pp. 389-394.

8. E. Gebhardt, M. Becker, J. Dorner, Metallkunde, v. 44 (1953), pp. 510-518.

9. R. Mehrabian, M. A. Keane, M. C. Flemings, Met. Trans., v. 1 (1970), pp. 3238-3241.

10. H. R. Thresh, A. F. Crawley, Met. Trans., v. 1 (1970), pp. 1531-1535.

11. T. S. Piwonka, M. C. Flemings, Trans. TMS-AIME, v. 236 (1966), pp. 1157-1165.

12. D. Apelian, M. C. Flemings, R. Mehrabian, Met. Trans., v. 5 (1974), pp. 2533-2537.

13. M. J. Streat and F. Weinberg, Met. Trans. B., v. 7b (1976), pp. 417-423.

14. E. C. Ellwood and J. M. Silcock, J. Inst. Metals, v. 74 (1948), pp. 457-467.

15. H. R. Thresh, A. F. Crawley and D. W. G. White, Trans. TMS-AIME, v. 242 (1968), pp. 819-822.

- 35 -

16. H. J. Fisher, A. Philips, Trans. TMS-AIME, v. 200 (1954),
     pp. 1060-1070.

17. A. Lee and G. V. Raynor, Proc. Phys. Soc., v. B67 (1954),
     pp. 737-747.

18. C. Tyzack and G. V. Raynor, Acta Cryst., v. 7 (1954), pp.
     505-510.

19. Metals Handbook, v. 8, A.S.M., Metals Park, Ohio, 1973, p. 330.

20. P. O. Mellberg and H. Sandberg, Scand. J. Metallurgy, v. 2
     (1973), pp. 83-86.

16. M. C. Flemings, A. Phillips, Trans. TMS-AIME, v. (1956)
pp. 1060-1070.

17. R. Lee and G. C. Apparisco, Phys. Soc., v. 76 (1920)
pp. 715-711.

18. E. Brosch and G. V. Mayer, Acta Cryst., v. 8 (1955), p.
305-310.

19. Metals Handbook, v. 8, 8th Ed., Metals Park, Ohio, 1973, p. 256.

20. J. W. Powers and E. Wilberg, Metals Science Quarterly, v. 3
(1964) 51-60.
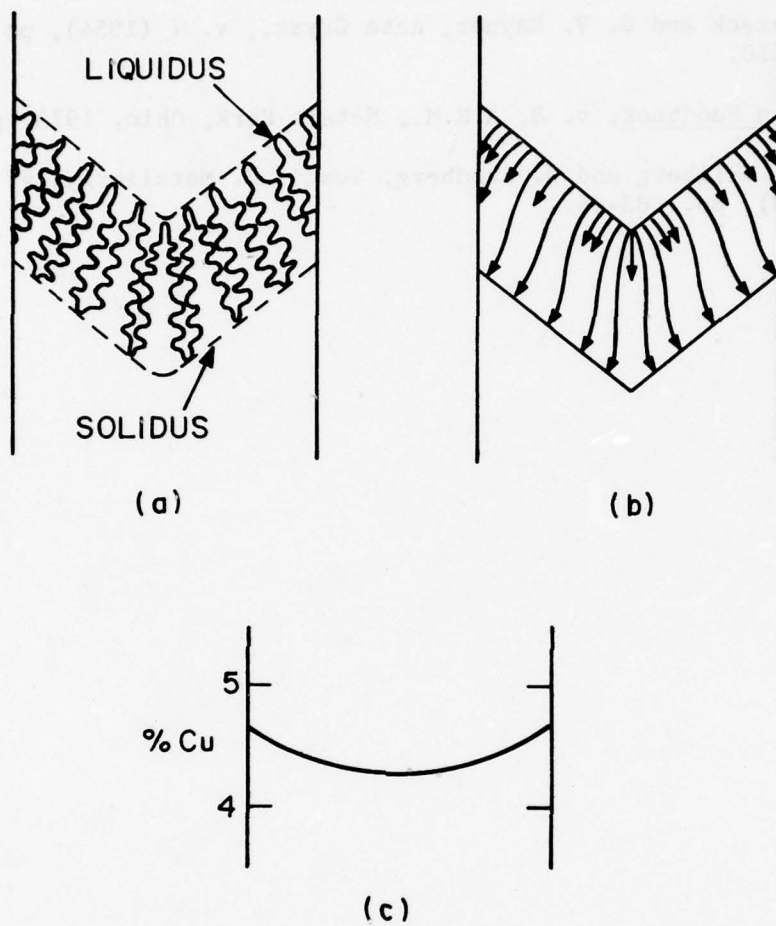
Figure 2-1: Macrosegregation in an Al-4.4%Cu ESR ingot. (a) Mushy zone; (b) flow lines for interdendritic liquid; (c) macrosegregation.
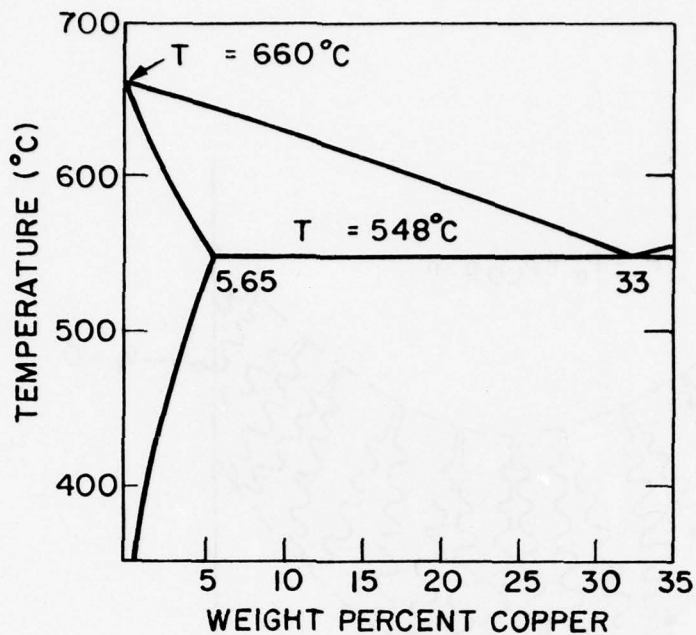
(a)
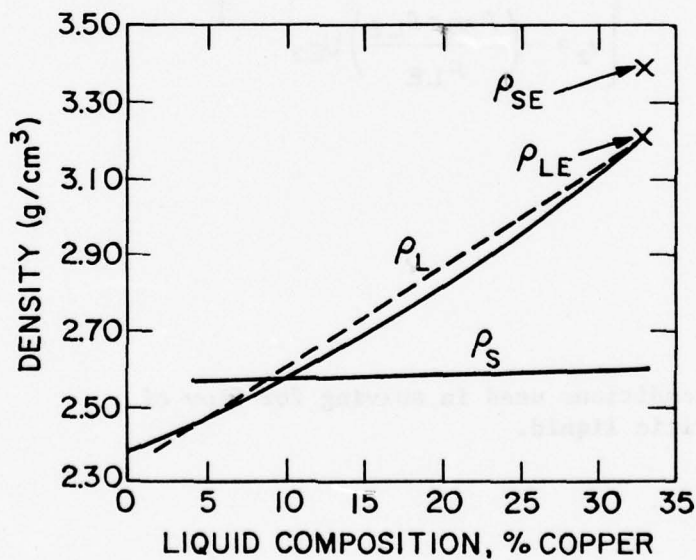
(b)

Figure 2-2: Tin-lead system. (a) Phase diagram (from reference 19); (b) densities of solid and liquid phases during solidification computed with data from references 15 – 18.

- 38 -
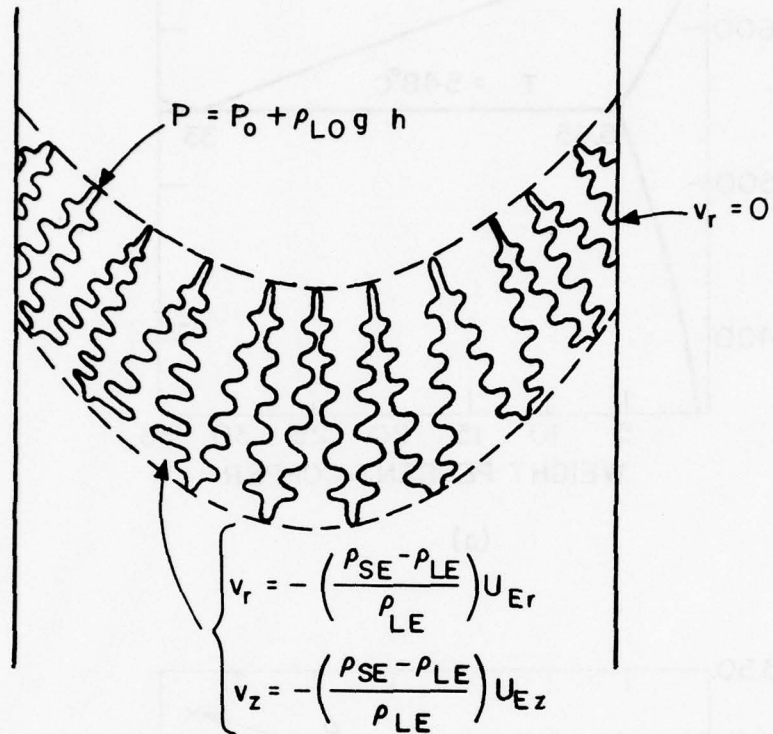
Figure 2-3: Boundary conditions used in solving for flow of interdendritic liquid.
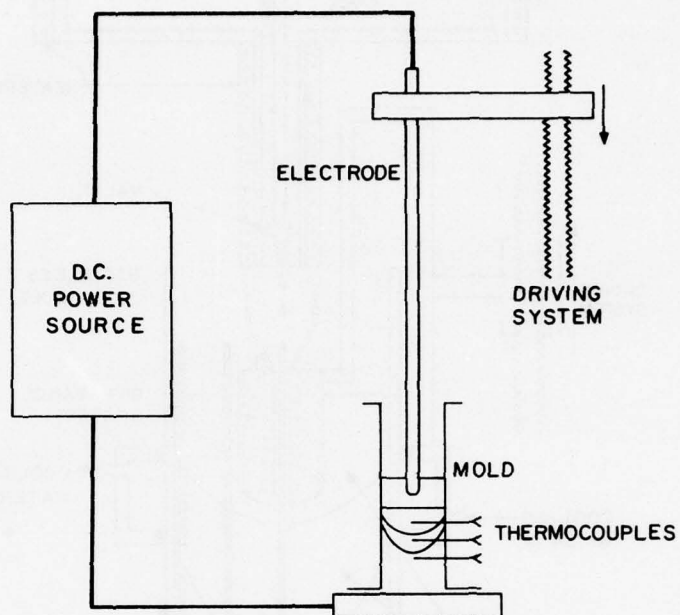
Figure 2-4: **The experimental set-up used to study macrosegregation in Al-4%Cu ESR ingots.**
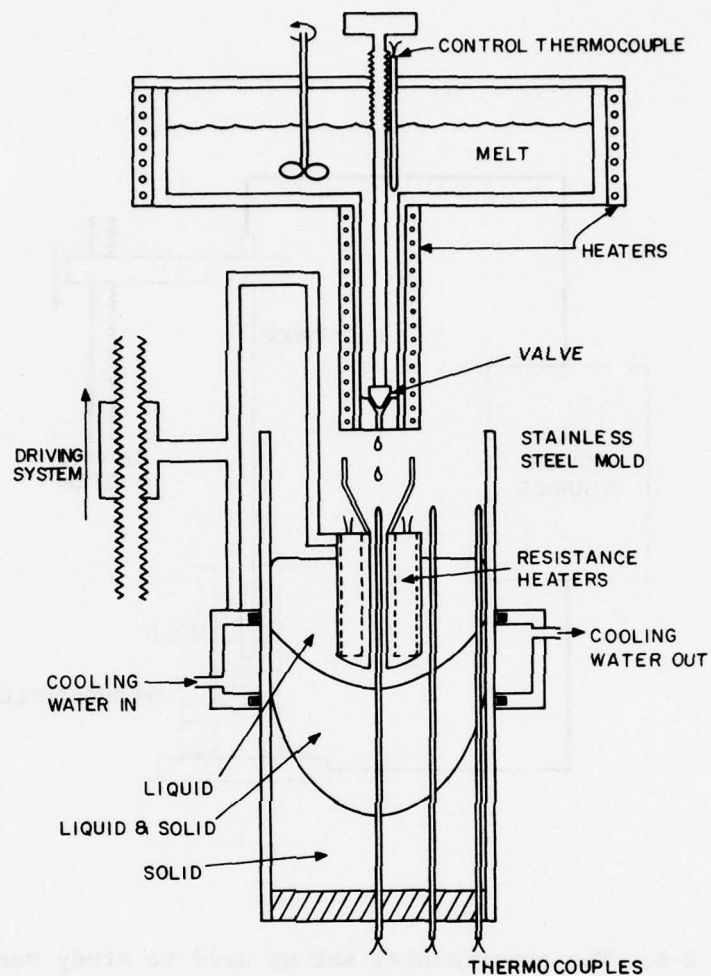
Figure 2-5: Apparatus used as an analog ESR process to produce Sn-15%Pb ingots.
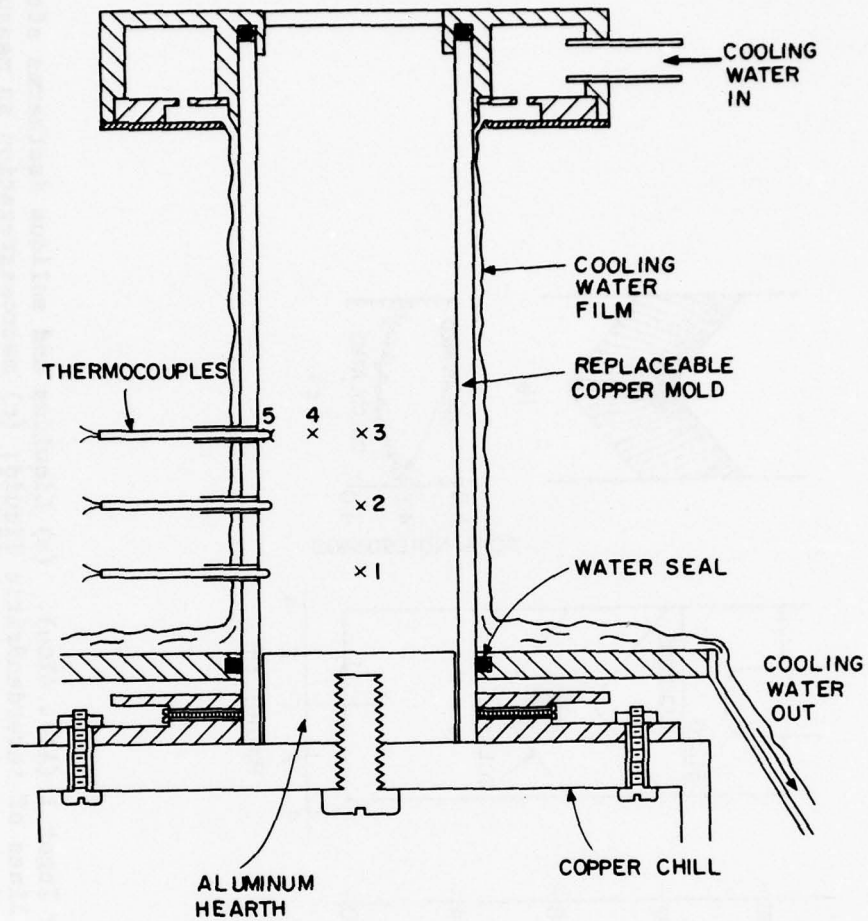
Figure 2-6: Design with replaceable mold wall. Numbers indicate thermocouples.
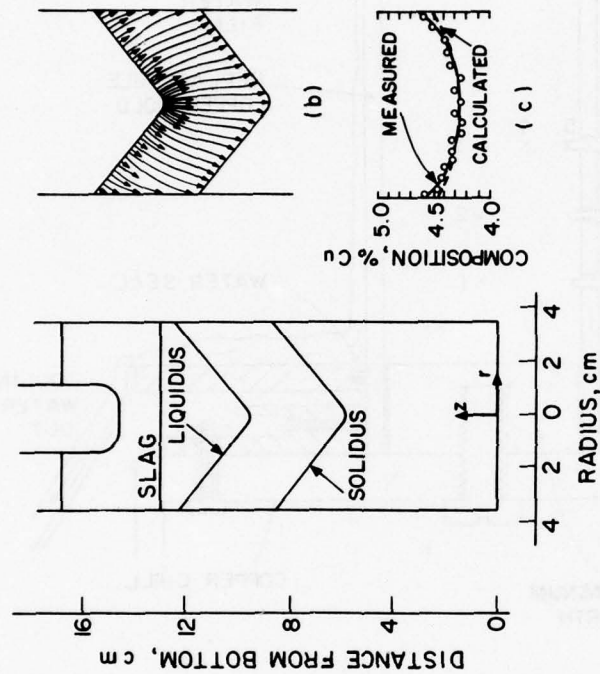
Figure 2-7: Results obtained for Ingot 1 (Al-4.4%Cu). (a) Liquidus and solidus isotherms after 7 minutes; (b) flow lines of interdendritic liquid; (c) macrosegregation as measured (solid curve) and calculated with $\gamma = 5 \times 10^{-7}$ cm^2 (broken curve).
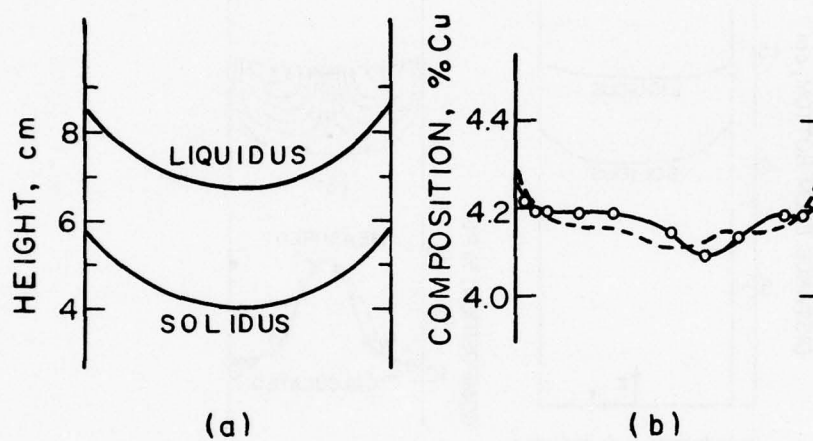
Figure 2-8: Ingot 3 (Al-4.2%Cu). (a) Position of isotherms used for calculations (b) macrosegregation by experiment (solid curve) and by calculation with $\gamma = 3 \times 10^{-7}$ cm^2 (broken curve).
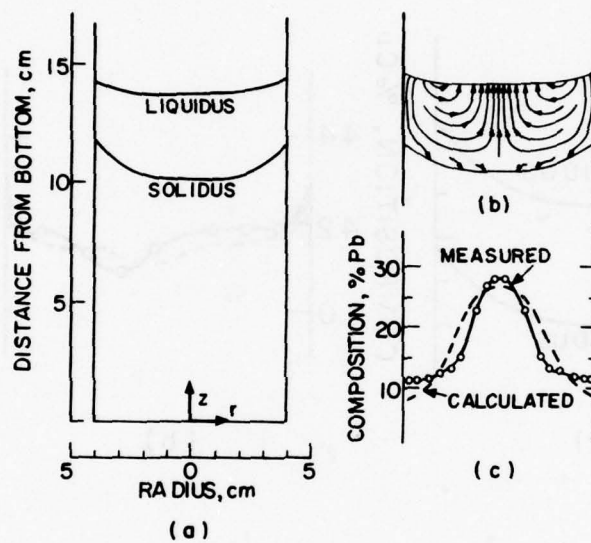
Figure 2-9: Results obtained for Ingot 4 (Sn-15%Pb). (a) Liquidus and solidus isotherms after 25 minutes; (b) flow lines of interdendritic liquid; (c) macrosegregation as measured (solid curve) and calculated with $\gamma_0 = 3.7 \times 10^{-6}$ cm^2 (broken curve).
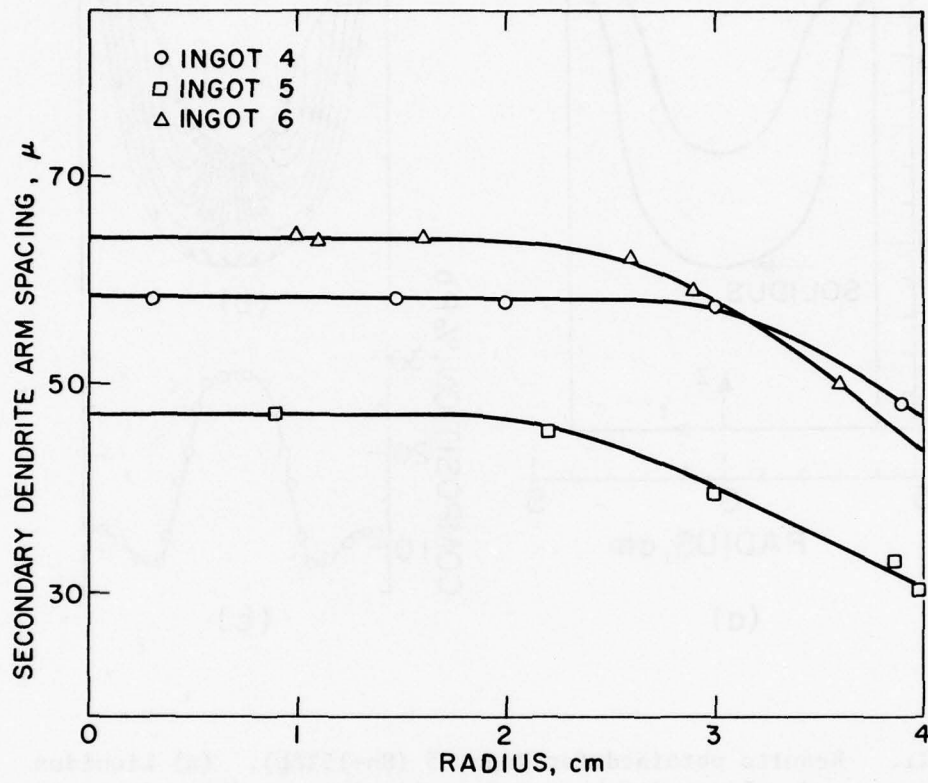
Figure 2-10: Secondary dendrite arm spacings in the Sn-15%Pb ingots.
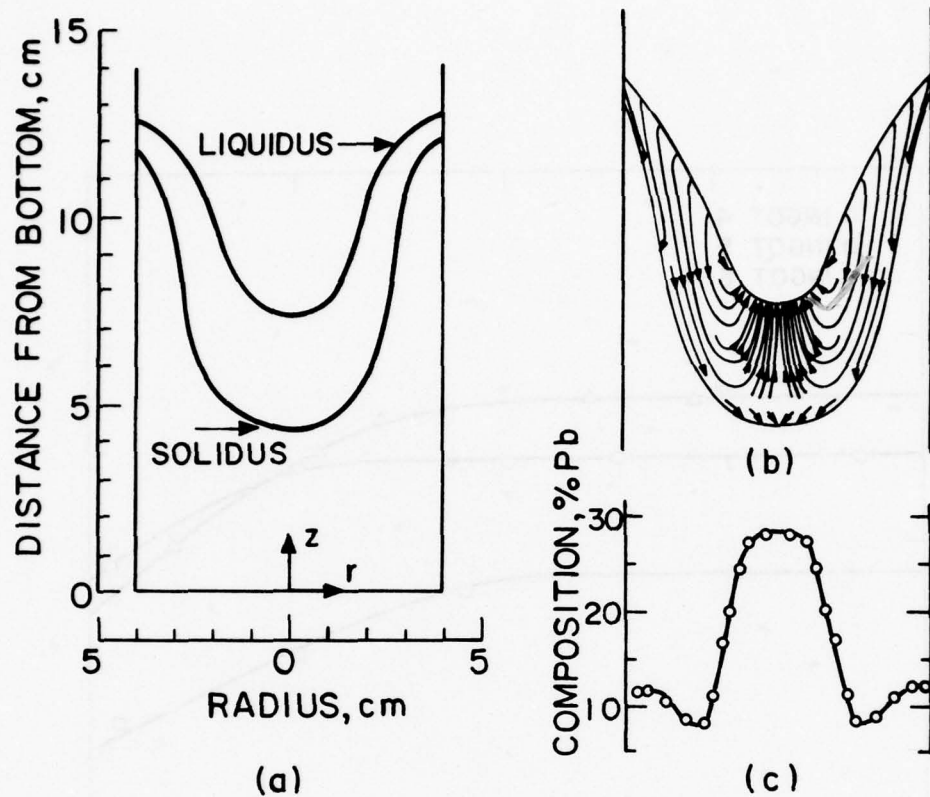
Figure 2-11. Results obtained for Ingot 5 (Sn-15%Pb). (a) Liquidus and solidus isotherms after 14 minutes; (b) calculated flow lines of interdendritic liquid with $\gamma_o = 2 \times 10^{-7}$ cm^2; (c) macrosegregation as measured.
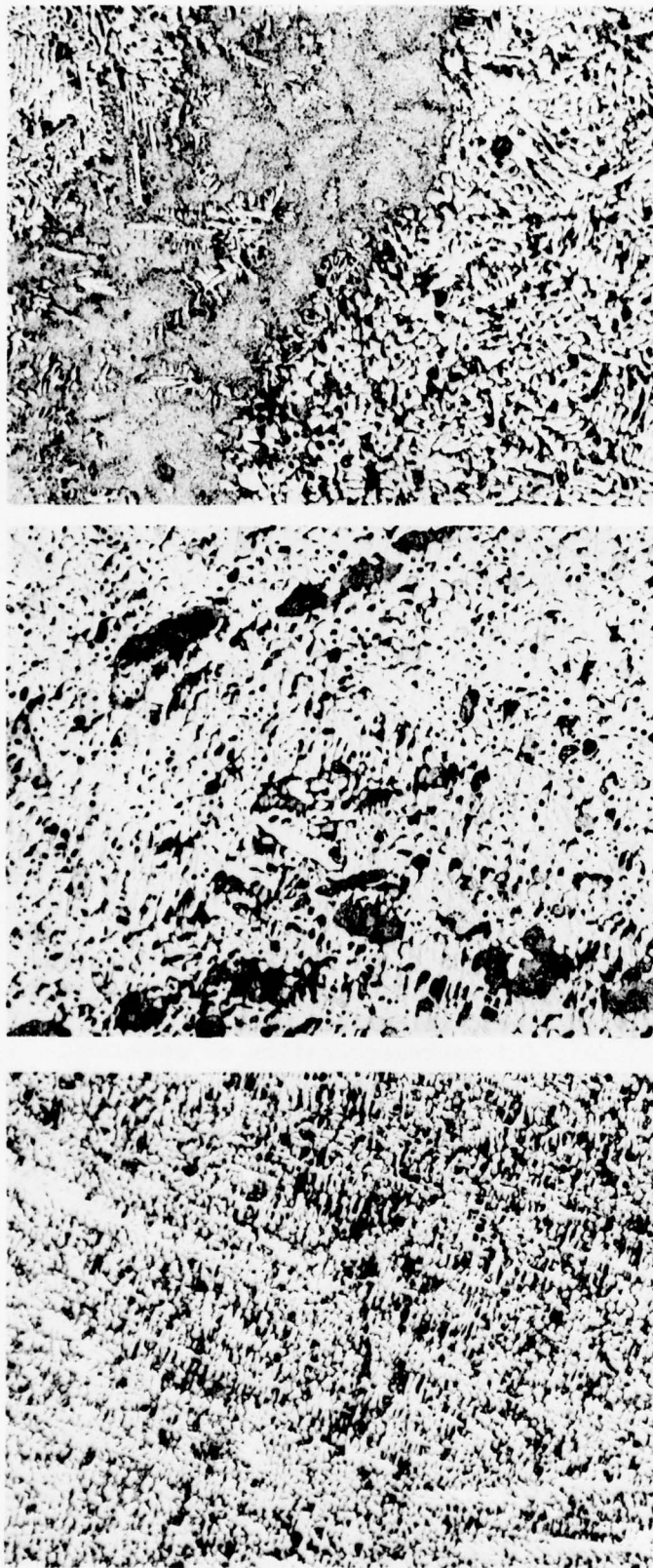
Figure 2-12: Structure of ingot 5 (Sn-15%Pb): (a) near surface; (b) 1.5 cm radius; (c) center. Mag. 25.6X.
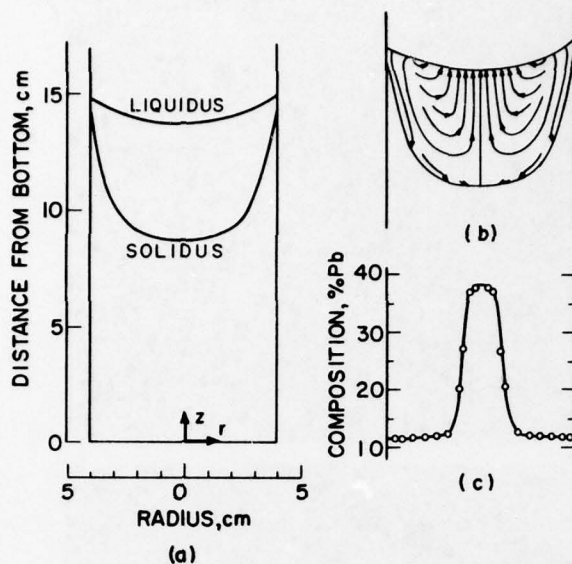
Figure 2-13: Results obtained for Ingot 6 (Sn-15%Pb). (a) Liquidus and solidus isotherms after 21 minutes; (b) flow lines of interdendritic liquid calculated with $\gamma_o = 8 \times 10^{-7}$ cm^2; (c) macrosegregation as measured.

INCREASING DEGREE OF MACROSEGREGATION WITH INCREASING DEPTH OF MUSHY ZONE

$R = 5.3 \times 10^{-2} \dfrac{cm}{sec}$

$Z_L - Z_S = 3.8$ cm

% Cu

5

4

(a)

NO EFFECT OF $(Z_L - Z_S)/R$

$r = 3.4$ cm

5

4

(b)

CHANGING FROM "−" $\bar{\xi}$ TO "+" $\bar{\xi}$
MACROSEGREGATION WITH INCREASING $(Z_L - Z_S)/R$

5

4

(c)

INCREASING DEGREE OF MACROSEGREGATION WITH INCREASING DEPTH OF MUSHY ZONE

$R = 5.3 \times 10^{-3} \dfrac{cm}{sec}$

$Z_L - Z_S = 5$ cm

% Cu

10

0

(d)

$r = 3.4$ cm

10

0

(e)

10

0

(f)
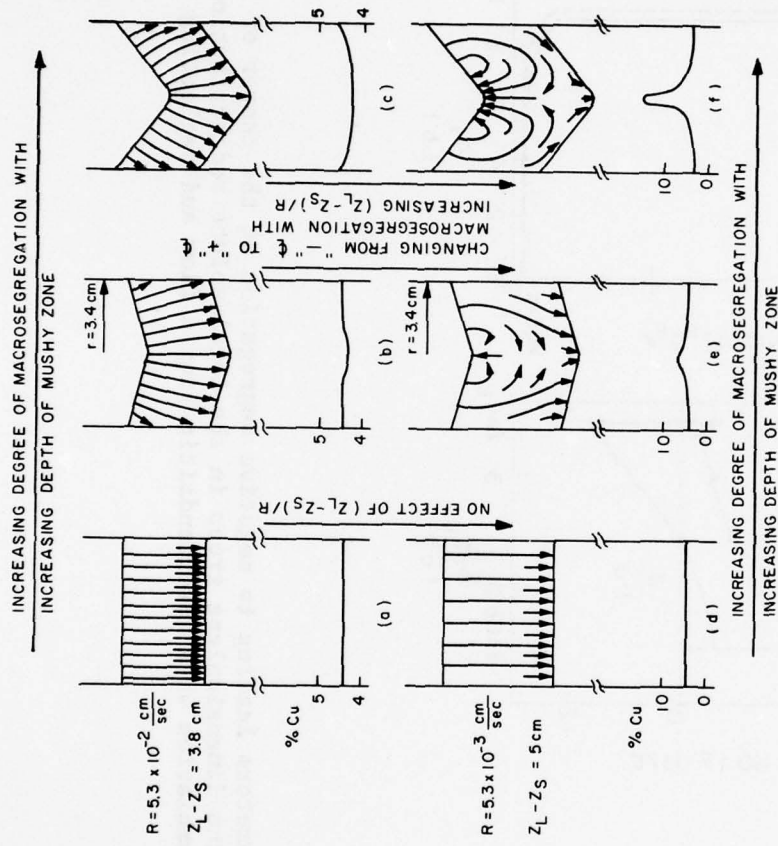
Figure 2-14:   Effects of mushy zone shape and solidification rate on macrosegregation in Al-4.4%Cu.
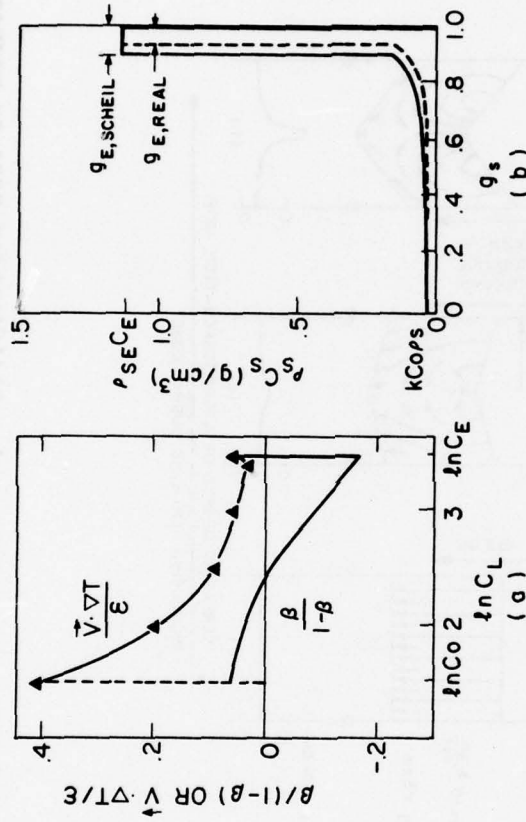
Figure 2-15: Parameters leading to negative segregation at the center of Ingot 1 (Al-4%Cu). (a) Values of the dimensionless group in the local solute redistribution equation; (b) solute accumulation with interdendritic liquid flow and neglecting flow (Scheil equation).
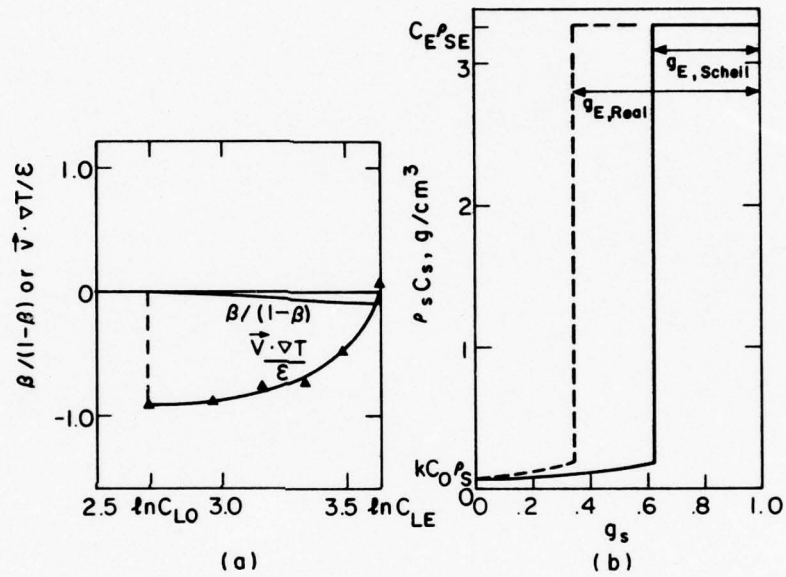
Figure 2-16: Parameters leading to positive segregation at the center of Ingot 4 (Sn-15% Pb). (a) Values of the dimensionless group in the local solute redistribution equation; (b) solute accumulation with interdendritic liquid flow and neglecting flow (Scheil equation).

Chapter III

MACROSEGREGATION IN ROTATED ELECTROSLAG REMELTED INGOTS

This chapter will be published in Metallurgical Transactions B, 1978.

Abstract

A computer model is presented for predicting macrosegregation in rotated electroslag ingots. Sample calculations of segregation are carried out for ingots of the model alloy Sn-12% Pb in which the liquid density increases during solidification and for two hypothetical alloys; in one, the liquid density decreases during solidification, and in the other, liquid density first increases and then decreases during solidification.

In alloys such as Sn-Pb in which liquid density increases during solidification, segregation is positive at the ingot centerline and if solidification is sufficiently slow, "freckles" form near the centerline. Positive segregation and freckles are found at the outer periphery of the ingot when liquid density decreases during solidification. Positive segregation and freckles are found at midradius when liquid density first increases and then decreases during solidification, and when the solidus isotherm changes shape abruptly at midradius (with density increasing during solidification).

Ingot rotation, by introducing a radial component to the force field, alters interdendritic flow behavior and therefore macrosegregation. Modest rotation speeds eliminate "freckles" and reduce macrosegregation in all modeling studies conducted. Greater rotational speeds can accentuate the segregation.

Experiments were conducted on simulated electroslag ingots of Sn–Pb alloy. The ingots were 8 cm dia., rotated at speeds up to 119 rpm and solidified at rates from 5.3×10^{-3} cm/sec to 1.36×10^{-2} cm/sec. Segregation behavior obtained agrees qualitatively and quantitatively with theory.

Introduction

In previous work by the authors[1], small-scale experimental ingots of Sn–15% Pb were solidified at low rates (approx. 5×10^{-3} cm/sec) in order to study the type of macrosegregation found in large commercial electroslag ingots. In the experimental ingots, severe segregation was produced, as measured by a large variation of composition across the ingots, and by severe-localized segregates, often called "freckles". Both types of macrosegregation are caused by the gravity-induced flow of interdendritic liquid within the mushy zone during solidification. In this study, we present a method of reducing the segregation by use of centrifugal force. For example, Fig. 1 shows experimental results obtained in a simulated electroslag ingot which solidified to a height of about

12 cm without rotation. Then the ingot was rotated at 45 rpm as solidification proceeded upwards; finally, the rotational speed was increased to 76 rpm. Fig. 1b shows the form of the very severe segregation when no rotation is employed; the composition at the center is eutectic composition for the Sn-Pb system. This indicates that during freezing, there was remelting of the dendrites which, in effect, leaves a "freckle" along the centerline of the ingot. This was verified by examination of the ingot structure. Fig. 2a shows that without rotation the ingot center is essentially one large freckle (entirely eutectic solid). When rotated at 45 rpm (Fig. 2b) freckles are still evident, but when the ingot is rotated at 76 rpm, there are no freckles. By rotating at 45 rpm, the center to surface segregation is reduced slightly. The greater rotational speed (76 rpm) reduced the segregation significantly in addition to eliminating the freckles.

Stewart et al[2] studied macrosegregation in rotated Al-3% Ag conventional type ingots. However, no significant effect of mold rotation on macrosegregation was found. This might be attributed to the fact that the test castings were solidified rapidly in small chill molds so that the effect of gravity on centrifugal force on interdendritic convection could not be observed. More recently, Keane[3] studied the effect of centrifugal force on macrosegregation in Al-4.5% Cu alloy. His work was on uni-directional solidification in the radial direction, thereby simulating a slice out of an ingot. However, only theoretical calculations were done; no experimental work was carried out.

In this paper, the equations describing the fluid flow and macro-segregation in rotated electroslag ingots are given. Results of calculations, based upon these equations, are presented to show the convection within the mushy zone during freezing and the macrosegregation resulting from the flow.

Finally, the macrosegregation obtained in several experimental ingots is shown to compare remarkably well with the macrosegregation predicted by the calculations.

MACROSEGREGATION THEORY

The equations which describe the convection of the interdendritic liquid and the macrosegregation across rotated electroslag ingots are similar to those employed for stationary electroslag ingots and given before[1]. The major difference is that Darcy's Law, which gives the liquid velocity inside the mushy zone, now contains a term for the centrifugal force so that

$$\vec{v} = -\frac{K}{\mu g_L} (\nabla P + \rho_L g \vec{z} - \rho_L \omega^2 r \vec{r}) \tag{1}$$

where $\vec{v}$ is the interdendritic liquid velocity, K is the specific permeability, P is pressure, μ is the viscosity of the interdendritic liquid, g_L is the fraction liquid, ρ_L is the density of the interdendritic liquid, g is acceleration due to gravity, ω is the rotation speed, r and z are

coordinates, and $\vec{z}$ and $\vec{r}$ are the axial and the radial unit vectors in cylindrical coordinates, respectively. When equation (1) is combined with the local solute redistribution equation and the equation of continuity in the mushy zone[1], we get the following equation which describes the pressure distribution inside the mushy zone:

$$\frac{\partial^2 P}{\partial r^2} + \frac{\partial^2 P}{\partial z^2} + A\frac{\partial P}{\partial r} + B\frac{\partial P}{\partial z} + C = 0 \qquad (2)$$

where A and B are defined as before[1] while C is now defined as follows:

$$C = g\rho_L \left[\frac{2}{g_L}\frac{\partial g_L}{\partial z} + \frac{2}{\rho_L}\frac{\partial \rho_L}{\partial z} + \alpha(\frac{\partial C_L}{\partial z}) - \alpha(\frac{\partial C_L}{\partial r})\frac{\omega^2 r}{g}\right]$$

$$- \frac{\varepsilon\mu}{m\gamma g_L}\left[\frac{1}{\rho_L}\frac{d\rho_L}{dC_L} + \alpha\right] - 2\omega^2\left[\rho_L + r\frac{\partial \rho_L}{\partial r} + \frac{\rho_L r}{g_L}\frac{\partial g_L}{\partial r}\right] \qquad (3)$$

In equation (3), $\alpha = \beta/C_L(1-k)$, k is the partition ratio, C_L is the composition of the interdendritic liquid, ε is the cooling rate, m is the slope of the liquidus on the phase diagram, and γ is a constant defined as K/g_L^2.

Equation (2) is solved for the boundary conditions previously given[1] except that the pressure at the liquidus isotherm is now given by:

$$P(\text{liquidus}) = P_o + \rho_{Lo}gh + \rho_{Lo}\omega^2 r^2/2 \qquad (4)$$

where P_o is the pressure at the top of the liquid pool, ρ_{Lo} is the density of the bulk liquid pool, and h is the height of the liquid pool.

Calculation of Macrosegregation

Macrosegregation in nonrotated ingots is demonstrated in Figure 3 which shows the effect of vertical solidification rate on the convection of interdendritic liquid within the mushy zone and the resulting macrosegregation profiles for ingots with three different isotherm shapes. Calculations are for Sn-12.2% Pb alloy with $\gamma = 1.2 \times 10^6 \text{cm}^2$ in an ingot with a diameter of 8 cm.

When the isotherms are both horizontal, as in unidirectional solidification (Figs. 3a and 3d), the flow of interdendritic liquid is purely vertical only to feed solidification shrinkage and so there is no macrosegregation. When the isotherms are concave with respect to the liquid pool, then gravity causes the solute-rich and more dense liquid to flow downwards towards the center and then upwards at the center. Because there is flow of solute-rich liquid towards the center, segregation is positive at the center and negative at the ingot surface. The effect of increasing the concavity of the isotherms as in Figs. 3c and 3f, at both solidification rates, is to increase the degree of segregation, but the effect of decreasing the vertical solidification rate (hence

increasing local solidification time) is more pronounced. In fact, when
R is reduced to 3.5×10^{-3} cm/sec, as in Fig. 3f, the upward flow of
interdendritic liquid is sufficiently strong, that liquid remelts
dendrites and produces channels for increased flow. This remelting
phenomenon produces what is commonly called "freckles" in remelted ingots
and is predicted by macrosegregation theory when $\vec{v} \cdot \nabla T/\varepsilon < -1$[1,7].
When $\vec{v} \cdot \nabla T/\varepsilon < -1$, our calculations are not truly valid and only approx-
imate, and so the calculated macrosegregation curve in Fig. 3f is
indicated by a broken line. Likewise, subsequent curves drawn with
broken lines indicate that $\vec{v} \cdot \nabla T/\varepsilon < -1$ in some portion of the ingot.

Although not demonstrated in Fig. 3, at a greater vertical
solidification rate, the segregation would be negative at the center
and increase to a positive value at the surface. In such instances,
the solidification time is so short that gravity induced flow is minor;
flow only satisfies continuity requirements to feed solidification
shrinkage and so flow of solute-rich liquid diverges from the center[1].

The effect of rotating the mold during solidification is shown
in Fig. 4. Here, the ingot depicted in Fig. 3f is repeated in Fig. 4a
as a reference case of an ingot which, when solidified with no rotation
(ω=0), has severe segregation including freckles centrally located. When
the mold is rotated at a modest rate (ω= 8.7 rad/s, Fig. 4b), freckles do
not result and the macrosegregation is reduced. At a greater speed, Fig. 4c,

as contrasted to Fig. 3. Again the effect of increasing the concavity of
the mushy zone is to increase the degree of macrosegregation, but the
effect of increasing the local solidification time (e.g., by decreasing
the vertical solidification rate from 1.68 x 10^{-2} cm/sec to 5.6 x 10^{-3} cm/sec)
is more pronounced. Indeed, in Fig. 6f upward flow is so great near the
ingot surface that freckles form.

Now in this case, the effect of rotating the mold is to shift
the positive segregation at the ingot surface to the ingot center, and
at a particular speed, the severity of the segregation is minimized.
This is shown in Fig. 7 where the nonrotated mold of Fig. 7a is the same
as that of Fig. 6f to serve as a basis. When the rotational speed is
excessive (Fig. 7d, $\omega = 21$ rad/s), segregation is strongly positive at
the center and freckles form. Of the speeds shown segregation is
minimum for $\omega = 13$ rad/s.

The case of liquid density increasing to a maximum and then
decreasing is particularly interesting; calculations for this case are
given in Figs. 8 and 9. In nonrotated ingots, Fig. 8, positive segrega-
tion appears neither at the center nor at the surface but rather at an
intermediate radial position. Since the overall density change is not
as great in previous two calculations, the degree of segregation is not
as severe and the vertical solidification rate is reduced to 1 x 10^{-3} cm/sec
before freckles are predicted (Fig. 8d). Note that the convection in the

lower segment of the mushy zone, where density increases, is down and
towards the center whereas in the upper segment, where density decreases,
flow is upwards. These calculations indicate that the convection of
interdendritic liquid depends strongly on the manner in which the density
of liquid varies during solidification and when convection is sufficiently
strong, freckles form at the ingot center (Fig. 3f), ingot surface
(Fig. 6f), or at an intermediate radial position (Fig. 8d).

The effect of rotation in the ingot of Fig. 8d is shown in Fig. 9.
The segregation at the location of the peak is reduced by rotation,
Figs. 9b – d, but when the ingot is rotated at an excessive speed (Fig. 9d,
ω = 13 rad/s), the greater centrifugal force at the ingot surface prevails
and causes the formation of freckles at the ingot surface.

The quantitative effect of the centrifugal force on the macro-
segregation is more clearly shown in Fig. 10 for the case of the ingot in
Fig. 4. In Fig. 10, $\Delta C/C_o$ is plotted vs. ω^2 where ΔC is the composition
of Pb at the ingot center minus the composition at the surface, and C_o is
the overall ingot composition.

The effect of centrifugal force is to decrease $\Delta C/C_o$ at all solidifi-
cation rates, but the effect of rotation decreases as the solidification
rate increases. For example, at a solidification rate as high as 5.6 x
10^{-2} cm/sec, macrosegregation across the ingot is very slight, and rotation
has hardly any effect on the macrosegregation.

It is most important to note that, although the solidification rate strongly affects macrosegregation, the optimum rotational speed for minimizing macrosegregation is independent of the solidification rate; $\omega = 12$ rad/sec to achieve $\Delta C = 0$ in this ingot at all solidification rates.

In the foregoing, macrosegregation theory is applied in order to show results of calculations given for ingots solidified with no rotation and for ingots solidified with rotation. In our previous paper[1], we showed that calculations compared well with two nonrotated ingots of Al-4% Cu and three of Sn-15% Pb alloy. Here, we compare calculations for rotated ingots of tin-rich Sn-Pb alloys.

APPARATUS AND EXPERIMENTAL PROCEDURE

The apparatus is shown in Fig. 11; this apparatus is a modified version of the simulated electroslag system previously used by the authors to study macrosegregation in stationary ingots[1]. The major changes are (1) the mold is attached to a turntable which can be rotated at desired speeds; (2) the resistance heaters inside the mold rotate with it, and (3) the output from thermocouples, which also rotate, is obtained with the help of a slip ring and brushes.

As shown in Fig. 11, the thermocouples were located inside three vertical stainless steel tubes. One thermocouple was located inside the central stainless steel tube; this thermocouple was slid up and down in order to trace the positions of the solidus and the liquidus isotherms at the ingot center. However, due to the mold rotation, the thermocouples inside the other two stainless steel tubes could not be slid up and down. Therefore, inside each of these tubes, three thermocouples were located and fixed at different heights. These six thermocouples were connected to the slip ring for thermal measurement. The experimental procedure was the same as employed in the case of no mold rotation[1], except that the mold was rotated during solidification.

EXPERIMENTAL RESULTS

In addition to the ingot described in Fig. 1, five ingots (No.'s 8 - 12) were rotated during solidification. Experimental results obtained from these ingots are summarized in Fig. 12. Ingots 8 - 10 solidified at similar rates (approx. 6×10^{-3} cm/sec) and with mushy zones of similar geometry. Without rotation, an ingot solidified at this speed would have severe macrosegregation with freckles at the centerline (e.g., Fig. 1b with $\omega = 0$ and Fig. 2a). With rotation at 83 rpm (Ingot 8), the positive centerline segregation is reduced and freckles are eliminated. With increasing rotational speeds (Ingots 9 and 10), the centerline segregation decreases even more, and the overall macrosegregation profile becomes

w-shaped to the extent that at a sufficiently high rotational speed, freckles form along the outer surface of the ingot. These results, of course, are in agreement with Fig. 4.

Ingots 11 and 12 are examples of mushy zones with isotherms that rise rapidly near the mold wall. In Ingot 11, notice that freckles formed between midradius and the full radius of the ingot corresponding to the approximate location where the isotherms rise rapidly. In Ingot 12, the effect is less severe because the rotational speed is less and the solidification rate about 60 percent greater. Results from these five ingots, indicate that rotation can be employed to decrease segregation, but since excess rotational speed acts to increase segregation, rotation should be done at a controlled rate, as also demonstrated in Figs. 4, 7, 9, and 10.

Results of calculations of the flow lines and comparison between calculated and experimental macrosegregation patterns are given in Fig.'s 13 - 17 for ingots 8 - 12, respectively. From thermal measurements, the liquidus and solidus isotherms at 30 minutes are shown in Fig. 13a for Ingot 8. With the moderate rotational speed (83 rpm) employed for this ingot, calculations of the flow lines show that interdendritic liquid is still significantly affected by the gravity force. This can be seen in Fig. 13b which shows that the liquid flows downwards from the ingot surface towards the center where it is diverted upwards. However, since this velocity of the upward moving liquid does not exceed the upward velocity of the isotherms,

there is no remelting of the dendritic structure and so freckles do not form. Rotation at this speed also significantly reduces the center to surface variation of composition. Fig. 13c shows that calculations agree well with experiment when the value of γ used in calculations is 1.2 x 10^6 cm^2.

Ingots 9 and 10 were solidified at similar casting speeds and isotherms as Ingot 8 but with greater rotational speeds. By increasing rotational speed to 97 rpm (Ingot 9) versus 83 rpm (Ingot 8), flow in the outer region of the ingot is no longer towards the center of the ingot and the upward flow of liquid in the central region is reduced; this is shown in Fig. 14b. Because of these changes in the flow lines, the composition at the surface in Ingot 9 (Fig. 14c) is greater than that in Ingot 8 (Fig. 13c), even though the positive segregation at the centerline is reduced somewhat. In short, the segregation curve takes on the W-shape evident in Fig. 13c. Calculations of macrosegregation agree remarkably well with experimental results with γ equal to 0.98 x 10^{-6} cm^2.

When the rotational speed is increased to 119 rpm, the flow of liquid towards the outer portion of the ingot is sufficiently strong that remelting (i.e., freckling) takes place at the surface of the ingot. This phenomenon is demonstrated in the results for Ingot 10 which are given in Fig. 15.

The calculations also show that $\vec{v} \cdot \nabla T/\epsilon < -1$ near the ingot surface, thereby predicting formation of freckles. To obtain the excellent agreement between calculations and experiment shown in Fig. 15c, a value of $1.3 \times 10^{-6} cm^2$ was chosen for γ. Microstructures showed no freckles across the entire ingot except at the ingot surface (Fig. 16) in agreement with calculations of Fig. 15c.

In Ingot 11, the shape of the mushy zone, shown in Fig. 17a, is different from those of Ingots 8 - 10. In particular, there is an abrupt change of the isotherm slopes beyond the midradius in this ingot. Macro-segregation is given in Fig. 17c where it is seen that the composition rises rapidly to about 25% Pb at a radial position of about 0.8 cm from the wall, where the isotherm slopes also increase rapidly. A value for γ of 3.3×10^{-6} cm^2 was used to calculate the flow pattern and macrosegregation shown in Fig. 17b and 17c, respectively. Although the agreement between the calculated and the measured macrosegregation is not as good as in Ingots 8 - 10, the calculations do predict the peaks in the segregation profile and predict freckle formation at the peaks. Microstructures showed clear evidence of freckling at about 0.8 cm from the ingot edge.

Ingot 12 was cast with a faster solidification rate than Ingot 11, i.e., 1.36×10^{-2} cm/sec, and even though the rotational speed, 54 rpm, is somewhat lower than that of Ingot 11. The resulting macrosegregation is much less with no evidence of freckles. The calculated flow pattern and

macrosegregation are shown in Figs. 18b and 18c, respectively, using a value of γ equal to 1.0×10^{-6} cm^2. The reduced segregation is due to an increase of about 60% in casting speed of Ingot 12 over that of Ingot 11 (see Fig. 12).

In the foregoing calculations, values of γ were chosen to obtain good agreement of theory with experiment, but the values chosen were self consistent as described below. First, for all ingots, permeability is assumed to vary with volume fraction liquid according to

$$K = \gamma g_L^2 \tag{5}$$

The applicability of equation (5) is based upon measurements of permeability in aluminum alloys[5,6], and it has been used previously to calculate inter-dendritic flow during solidification[7]. More recently, Weinberg and Streat[8] measured the permeability in partially solid lead-rich Pb-Sn alloy and showed, for a constant value of g_L, that

$$K = ad^2 \tag{6}$$

in which d is secondary dendrite arm spacing and a is a constant. Their results are consistent with values of d up to about 65 microns. Equations (5) and (6) predict that γ should be proportional to d^2 and Fig. 19 shows that the values of γ selected for Ingots 8 - 10, 12 and for another ingot previously reported[1,4] are consistent with this estimation. Since calculations are not valid when $(v \cdot \nabla T / \varepsilon) < -1$, only ingots with no freckles

are shown with the exception of Ingot 10 where freckles formed only at the surface layer of the ingot (Fig. 16).

CONCLUSIONS

1. Calculations which predict macrosegregation in rotated electroslag ingots compare well with experimental results.

2. Severe positive centerline macrosegregation can be significantly reduced and freckling in electroslag ingots can be eliminated if a suitable speed of mold rotation is applied during solidification. The optimum rotational speed for minimizing macrosegregation and eliminating freckles can be predicted by the calculations presented herein, and that optimum rotational speed for minimizing macrosegregation is independent of solidification rate.

3. The effect of centrifugal force on macrosegregation across electroslag ingots is affected by the solidification rate. At a high solidification rate (e.g., 10^{-2} cm/sec), the macrosegregation is slight and the centrifugal force has little effect on the macrosegregation. However, when macrosegregation is severe due to a very slow solidification rate (e.g., 10^{-3} cm/sec), rotation can be applied to minimize macrosegregation. However, if an excessive rotational speed (e.g., 150 rpm) is selected, the concentration profile is reversed.

For example, in alloys with an interdendritic liquid of increasing density during solidification, segregation is positive at the center and if the local solidification time is great enough, there will be freckles at the center. Excessive rotation of the mold during solidification reverses the concentration profile from positive center segregation to negative center segregation, and the location of the freckles moves from the central region of the ingot to the surface.

On the other hand, in alloys with decreasing density, excessive rotation reverses the center segregation from negative to positive, and moves the location of freckles from the surface of the ingot to the central region.

4. Freckles can form at intermediate radial positions in remelted ingots, in those alloys with a density variation of interdendritic liquid which increases to a maximum and then decreases. The same holds true when there is an abrupt increase in slope of the solidus isotherm as in Fig. 17. In both cases, a decrease in local solidification and/or mold rotation (if not excessive) eliminates the freckles.

REFERENCES

1. S. Kou, D. R. Poirier, and M. C. Flemings, "Macrosegregation in Electroslag Remelted Ingots", to be published in _Proceedings of the Electric Furnace Conference_, Iron and Steel Society of AIME, December 1977.

2. M. J. Stewart, L. C. MacAulay and F. Weinberg: Met. Trans., 1971, vol. 2, p. 169.

3. M. A. Keane, Sc.D. Thesis, Department of Materials Science and Engineering, Massachusetts Institute of Technology, 1973.

4. S. Kou, Ph.D. Thesis, Department of Materials Science and Engineering, Massachusetts Institute of Technology, 1978.

5. T. S. Piwonka and M. C. Flemings: Trans. TMS-AIME, 1966, vol. 236, p. 1157.

6. D. Apelian, M. C. Flemings and R. Mehrabian: Met. Trans., 1974, vol. 5, p. 2533

7. R. Mehrabian, M. A. Keane and M. C. Flemings: Met. Trans., 1970, vol. 1, p. 1209.

8. M. J. Streat and F. Weinberg: Met. Trans., 1976, vol. 7b, p. 417.
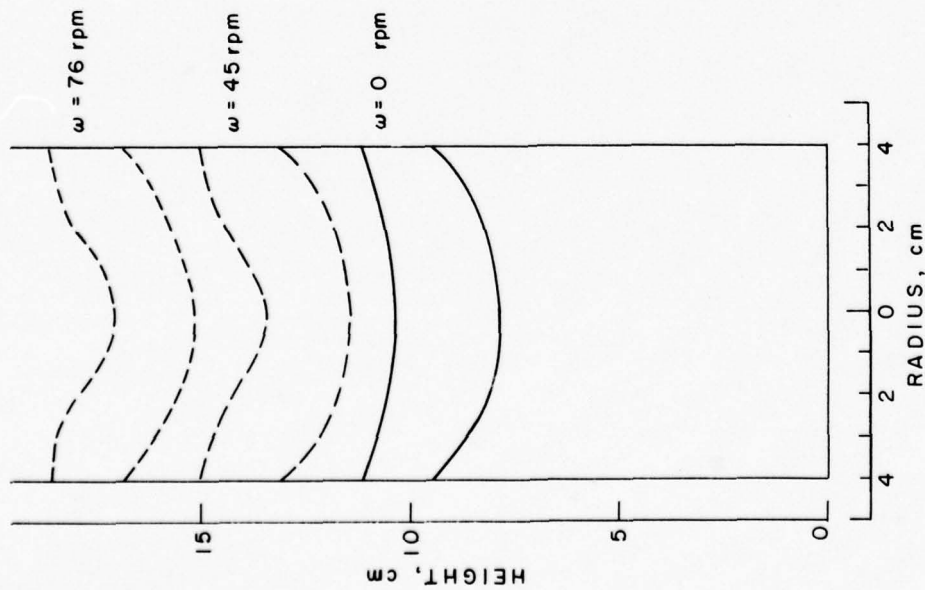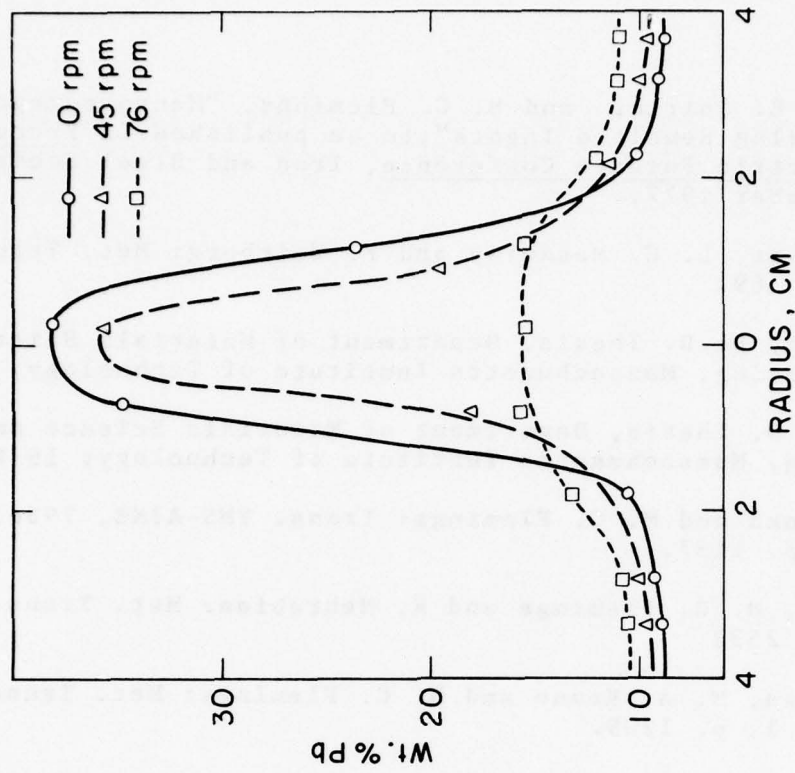
Figure 3-1. Effect of rotation on macrosegregation in Sn-12% Pb ingot. (a) Shape of mushy zone; (b) macrosegregation across the ingot.

(c)

(b)

(a)
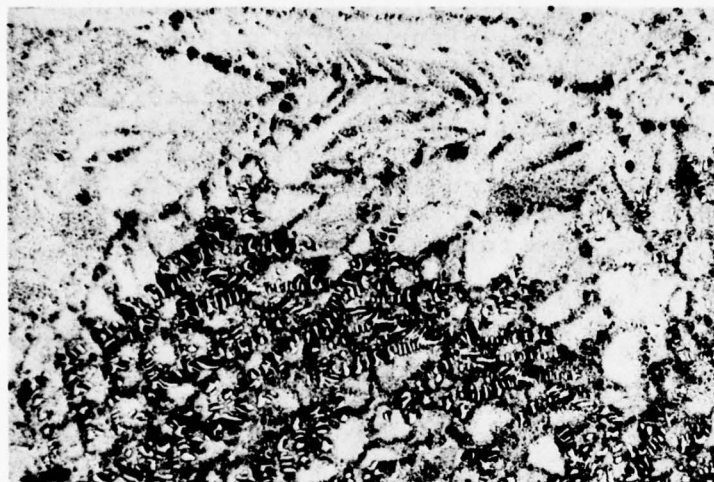
Figure 3-2. Structure of ingot of Figure 1 at center. (a) No rotation; (b) rotated at 45 rpm; (c) rotated at 76 rpm. Magnification 25.6X.

Figure 3-3.   Calculation of macrosegregation in nonrotated
                Sn-12.2% Pb ingots. Proceeding across illustrates
                the effect of increasing the concavity of the
                liquidus and solidus isotherms; proceeding from
                top to bottom shows the role of decreasing solidifi-
                cation rate. In (f), the macrosegregation profile
                is drawn with a broken curve to indicate that cal-
                culations predict the remelting of dendrites at the
                center, i.e., the formation of "freckles".
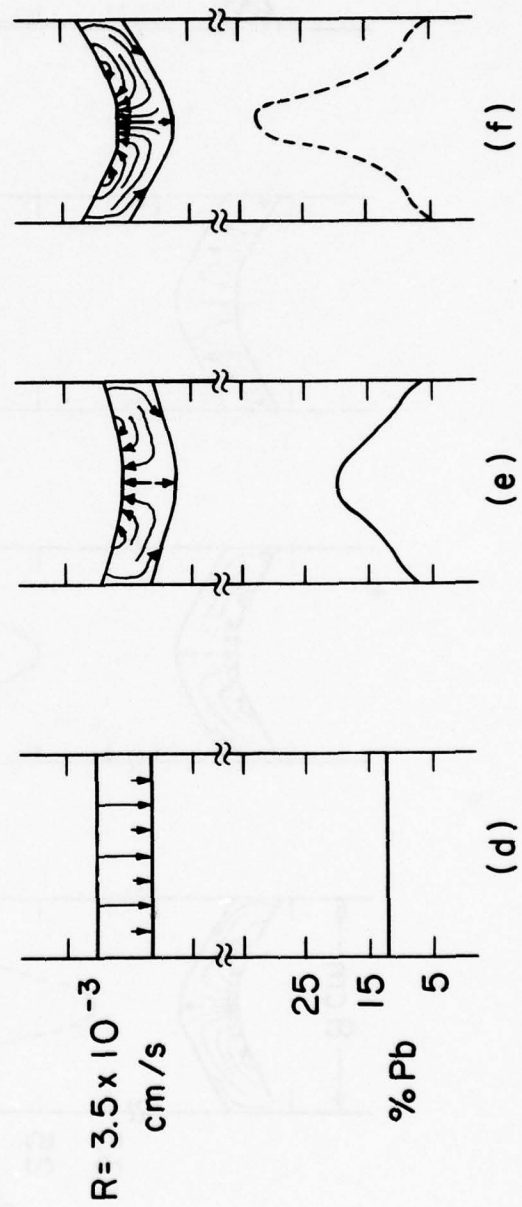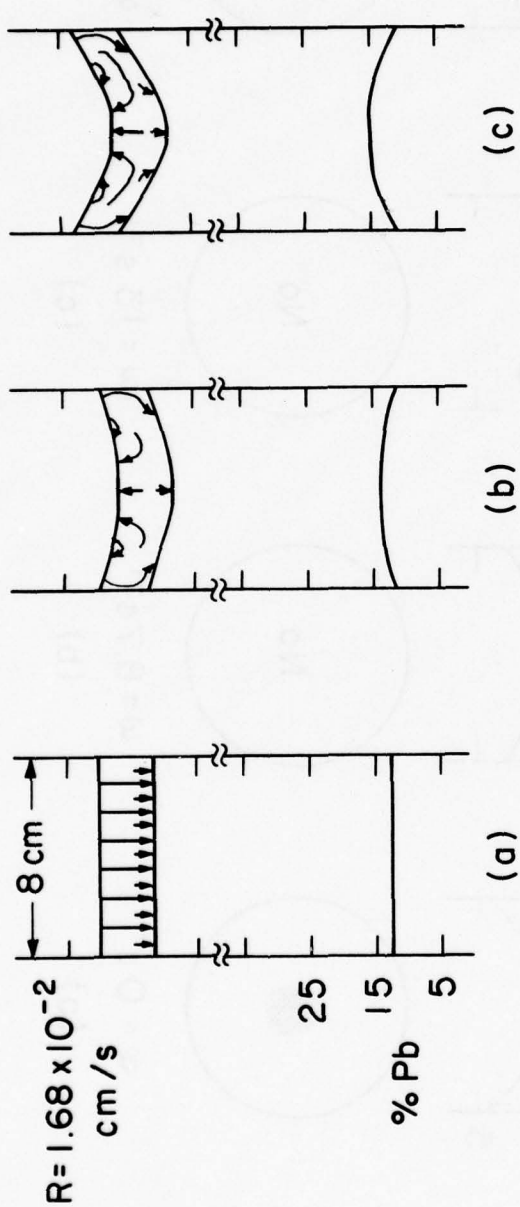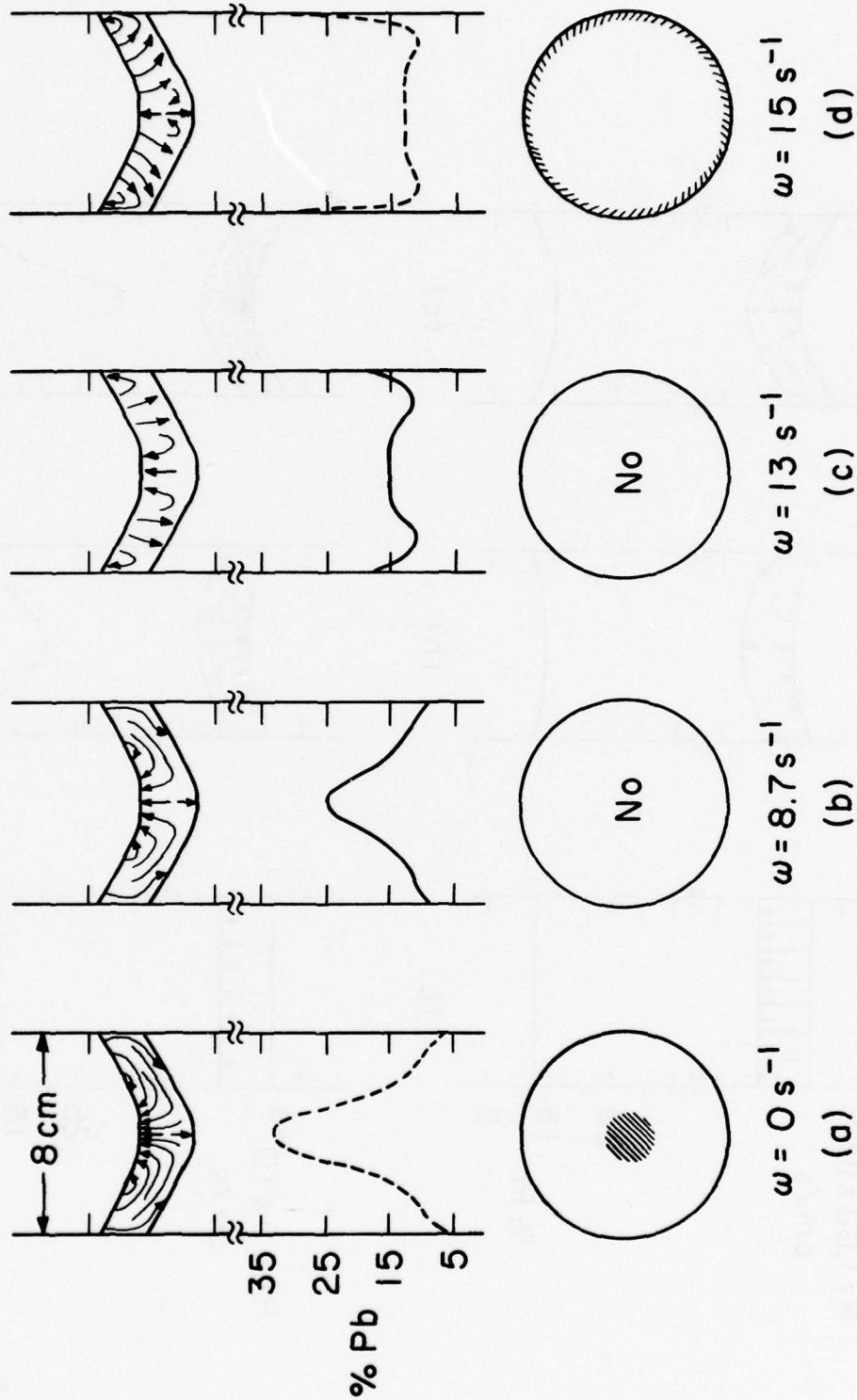
Figure 3-4. Effect of rotation on flow of interdendritic liquid and macrosegregation in Sn-12.2% Pb ingots. Proceeding from (a) to (d), calculations are for increasing rotational speed. Calculations predict remelting along the center in (a) and at the surface of (d).

-76-
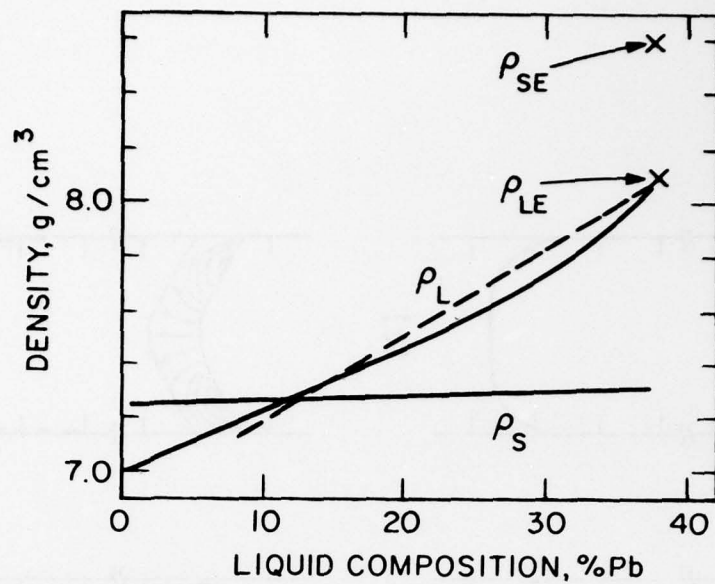
(a)
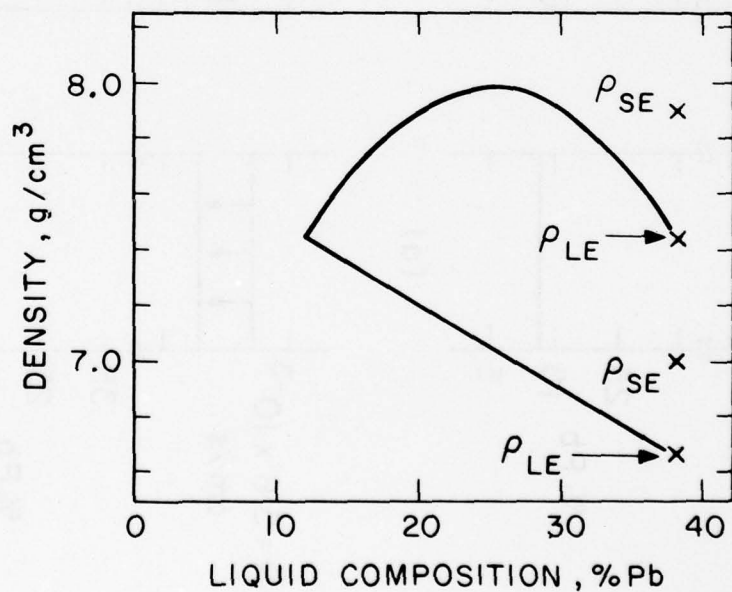
(b)

Figure 3-5. Density used for calculations. (a) Actual values of
density; density of interdendritic liquid increases
during solidification. (b) Hypothetical cases of
liquid density which decreases and of liquid density
which first increases and then decreases.
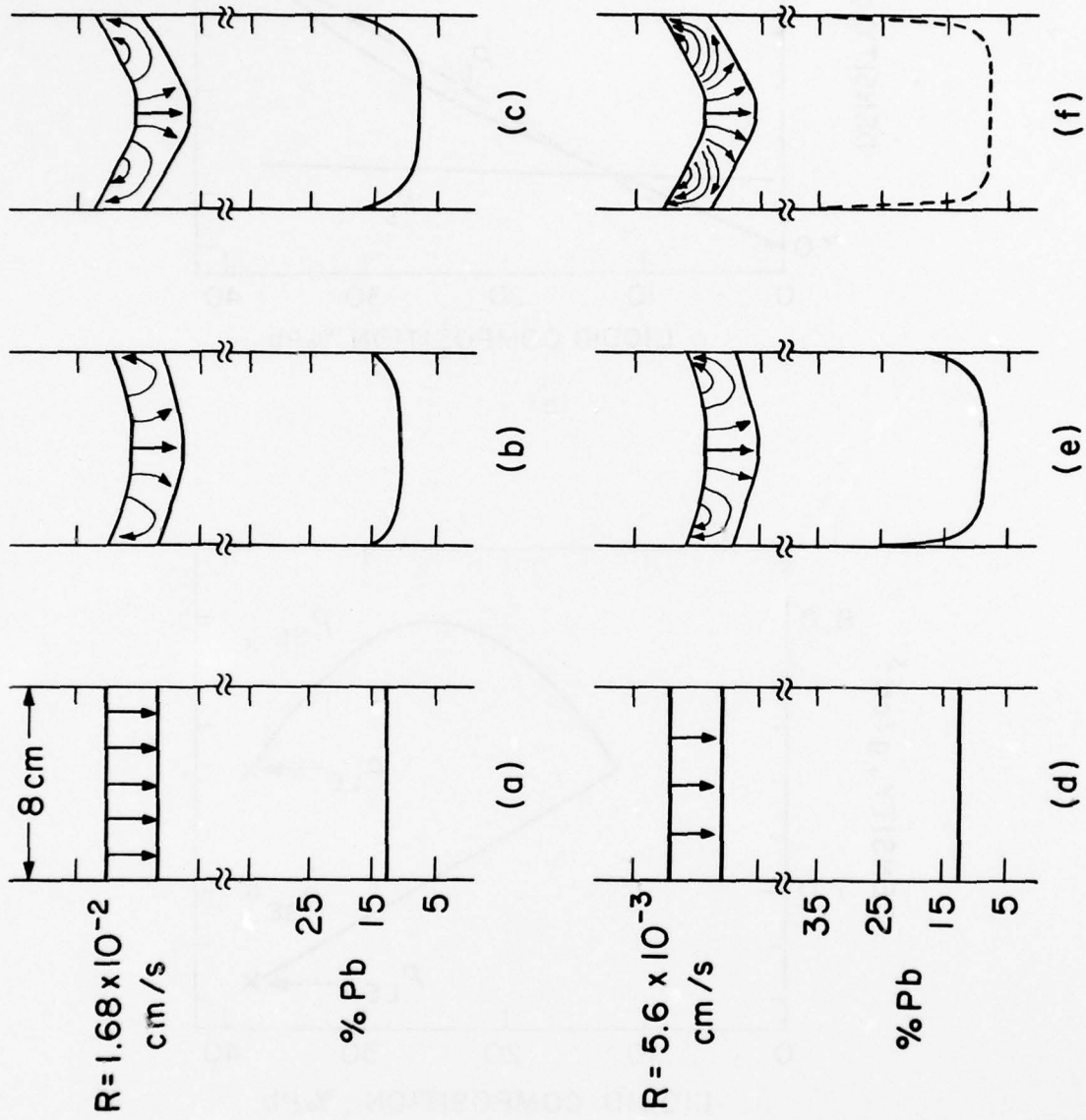
Figure 3-6. Calculation of macrosegregation in nonrotated Sn-12.2% Pb ingots assuming a decreasing density of liquid during solidification. As in Figure 3, proceeding across shows effect of increasing concavity of mushy zone and proceeding down, the role of decreasing solidification rate. Remelting is predicted at the surface in (f).
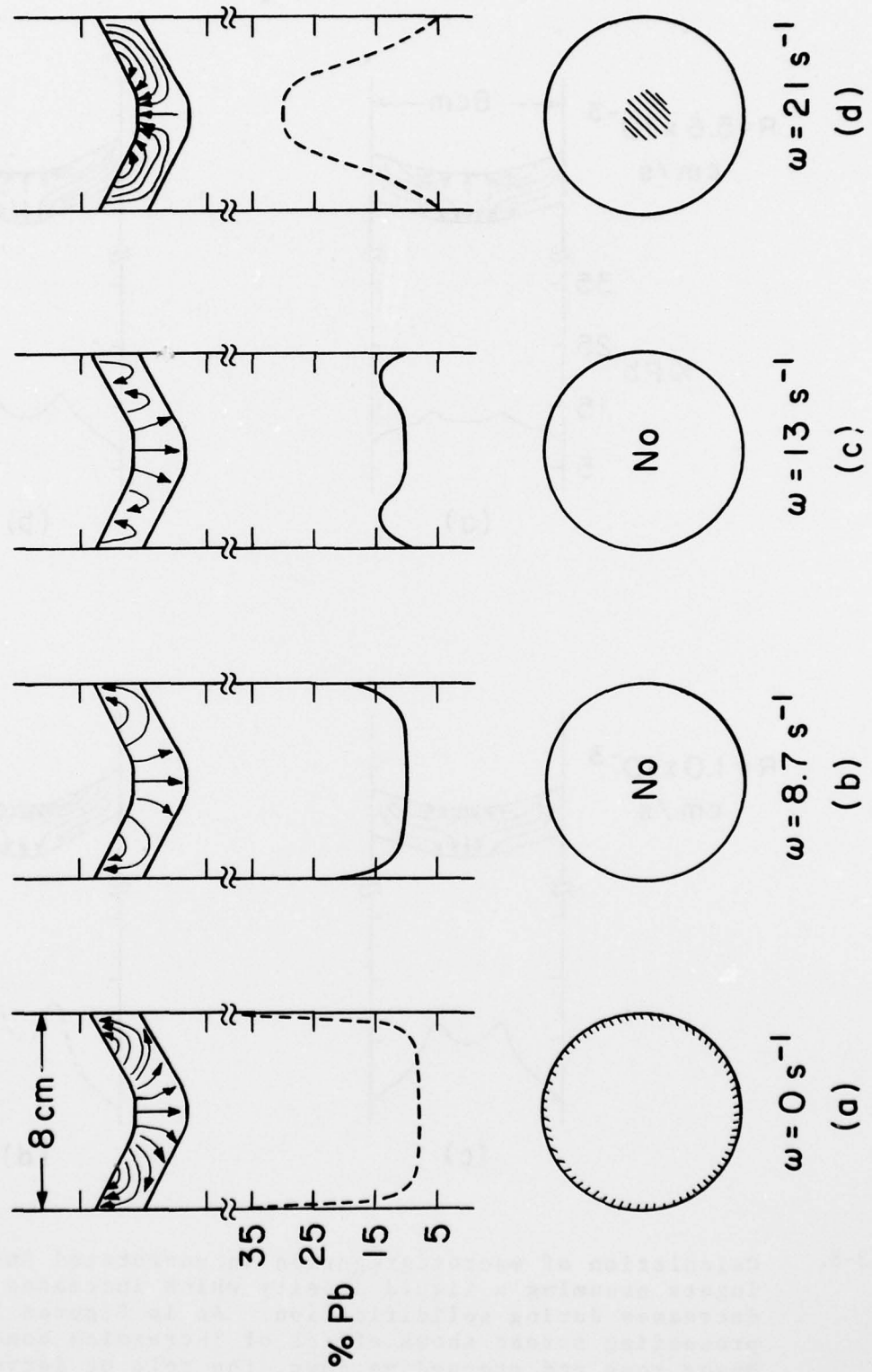
Figure 3-7. Effect of rotation on flow of interdendritic liquid and macrosegregation in Sn-12.2% Pb ingots assuming a decreasing density of liquid during solidification. Calculations predict remelting at the surface in (a) and along the center in (d).

-79-
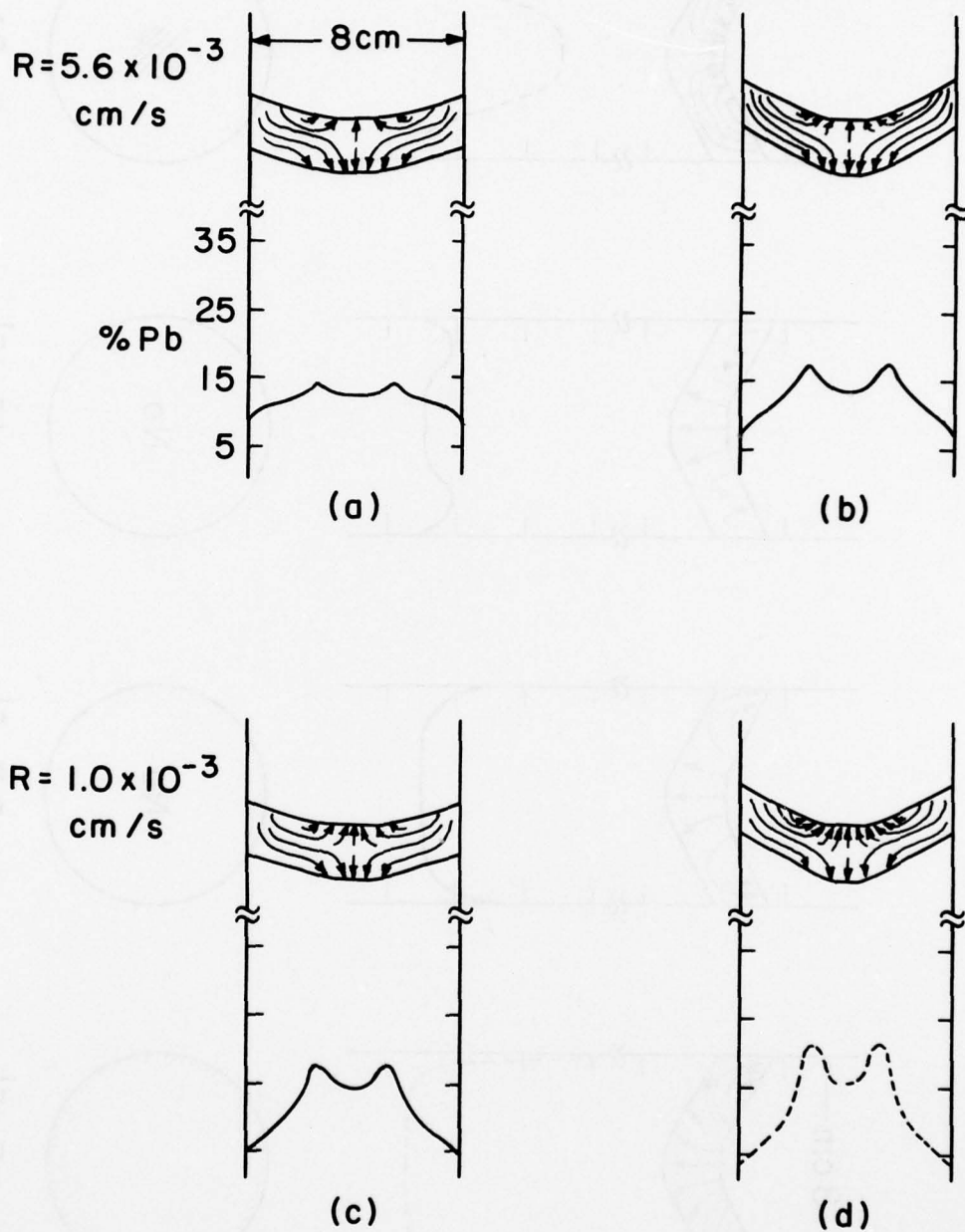
Figure 3-8. Calculation of macrosegregation in nonrotated Sn-12.2% Pb ingots assuming a liquid density which increases and then decreases during solidification. As in Figures 3 and 6, proceeding across shows effect of increasing concavity of mushy zone and proceeding down, the role of decreasing solidification rate. Remelting is predicted at the radial position of the peak in (d).

-80-
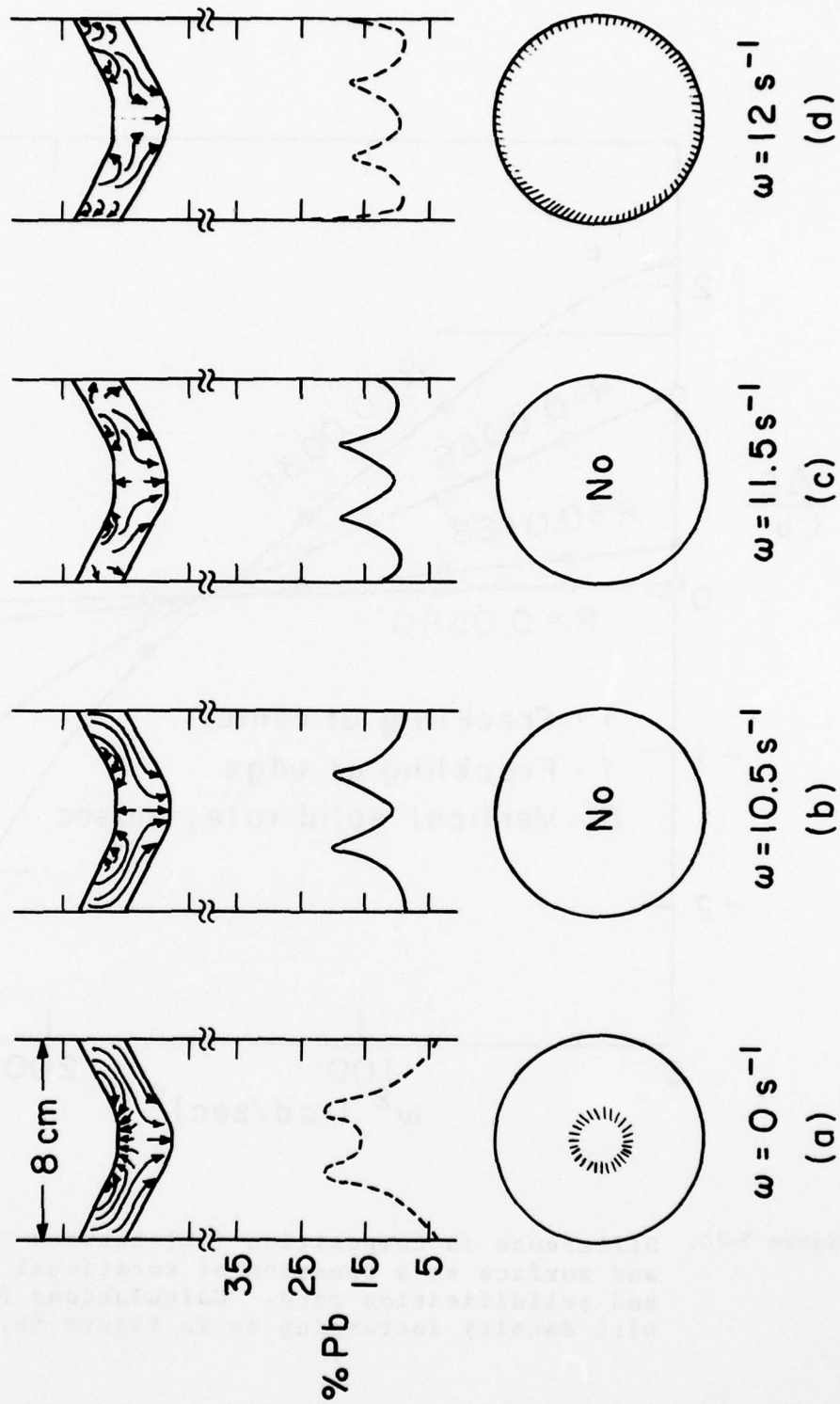
Figure 3-9. Effect of rotation on flow of interdendritic liquid and macrosegregation in Sn-12.2% Pb ingots assuming the same density variation used in Figure 8. Calculations predict remelting at the peak in (a) and at the surface in (d).
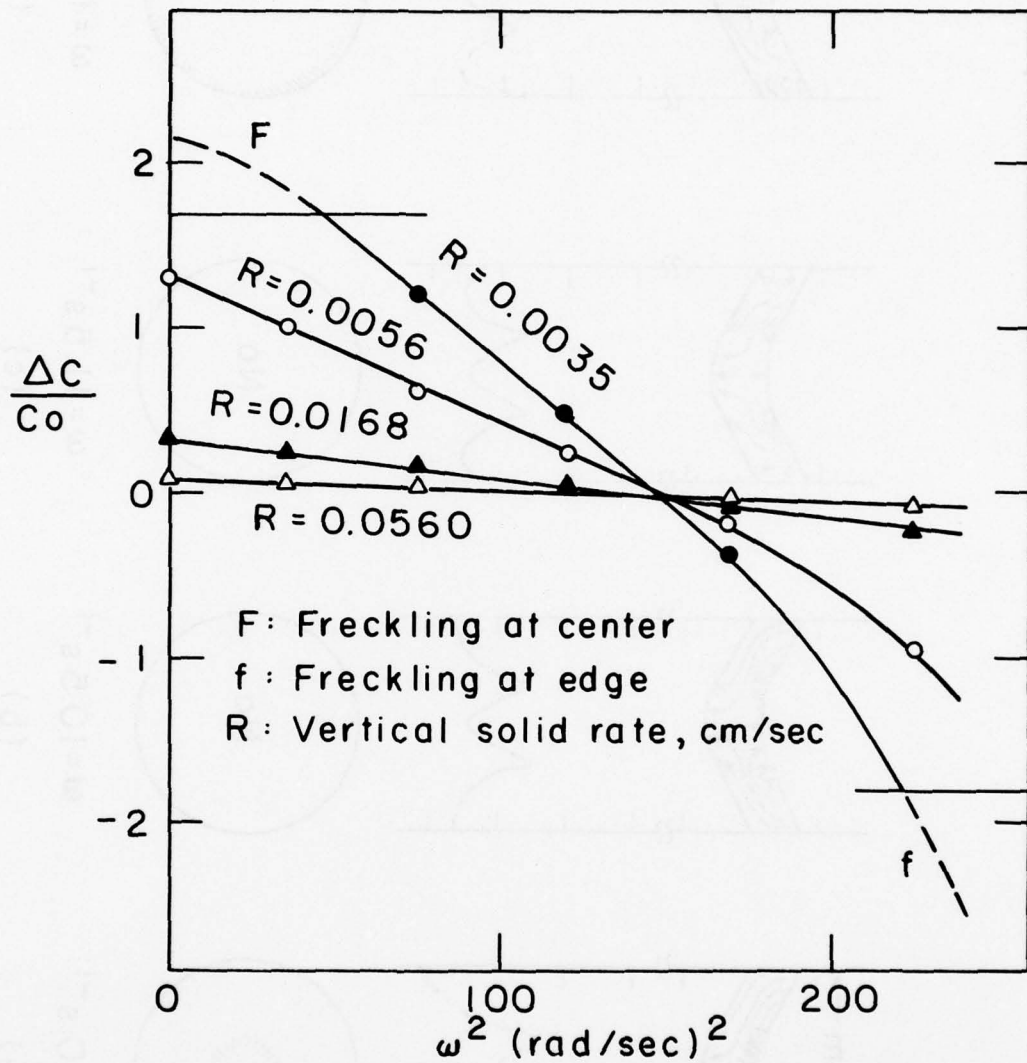
Figure 3-10. Difference in composition (ΔC) between center and surface as a function of rotational speed and solidification rate. Calculations for alloy with density increasing as in Figure 5a.
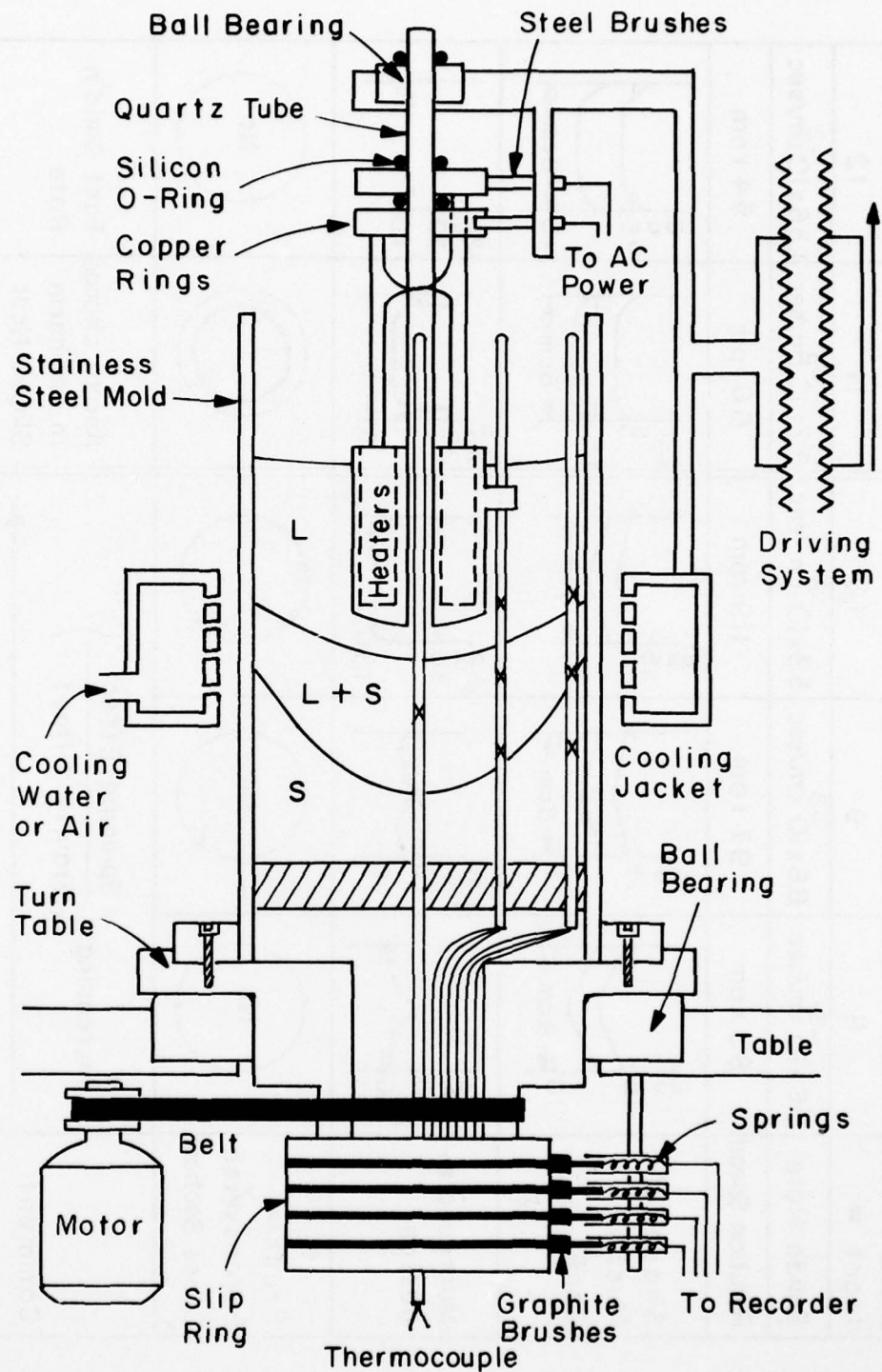
Figure 3-11. Apparatus for rotating ingots during solidification.
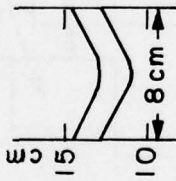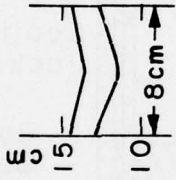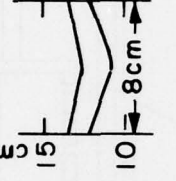
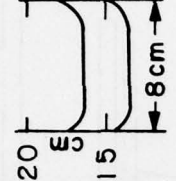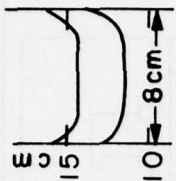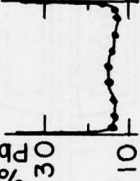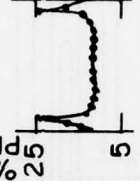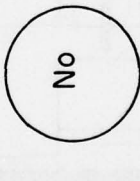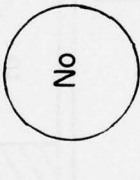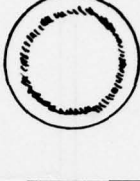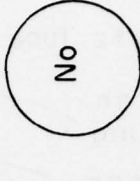| Ingot #	8	9	10	11	12
Solid'n Rate	5.6×10^{-3} cm/sec	6.6×10^{-3} cm/sec	5.3×10^{-3} cm/sec	8.3×10^{-3} cm/sec	1.36×10^{-2} cm/sec
Rotation Speed	83 rpm	97 rpm	119 rpm	66 rpm	54 rpm
Shape of Mushy Zone	(graph, 8 cm)	(graph, 8 cm)	(graph, 8 cm)	(graph, 8 cm)	(graph, 8 cm)
Macrosegregation	(Pb % graph)	(Pb % graph)	(Pb % graph)	(Pb % graph)	(Pb % graph)
Freckle (Transverse Cross Section)	No	No	(circle)	(circle)	No
Comment				Abrupt change in Isotherm Slopes Near Edge	Fast Solid'n Rate

Increasing $\left(\dfrac{\text{Spinning Effect}}{\text{Gravity Effect}} \right)$

Decreasing $\left(\dfrac{C_{center} - C_{edge}}{C_{origional}} \right)$

Figure 3-12. Summary of experimental ingots rotated during solidification.

Figure 3-13. Results for Ingot 8. (a) Mushy zone;
(b) calculated flow lines for interdendritic
liquid; (c) experimental and calculated segre-
gation ($\gamma = 1.2 \times 10^6 \text{cm}^2$).

Figure 3-14.   Results for Ingot 8. (a) Mushy zone;
(b) calculated flow lines for inter-
dendritic liquid; (c) experimental and
calculated segregation ($\gamma = 0.98 \times 10^{-6} cm^2$).

Figure 3-15. Results for Ingot 10. (a) Mushy zone; (b) calculated flow lines for inter-dendritic liquid; (c) experimental and calculated segregation ($\gamma = 1.3 \times 10^{-6} \mathrm{cm}^2$).

Figure 3-16.   Structure of surface of Ingot 10.
Magnification 128X.

Figure 3-17.   Results for Ingot 11.   (a) Mushy zone;
(b) calculated flow lines for interdendritic
liquid; (c) experimental and calculated
segregation ($\gamma = 3.3 \times 10^{-6} cm^2$).
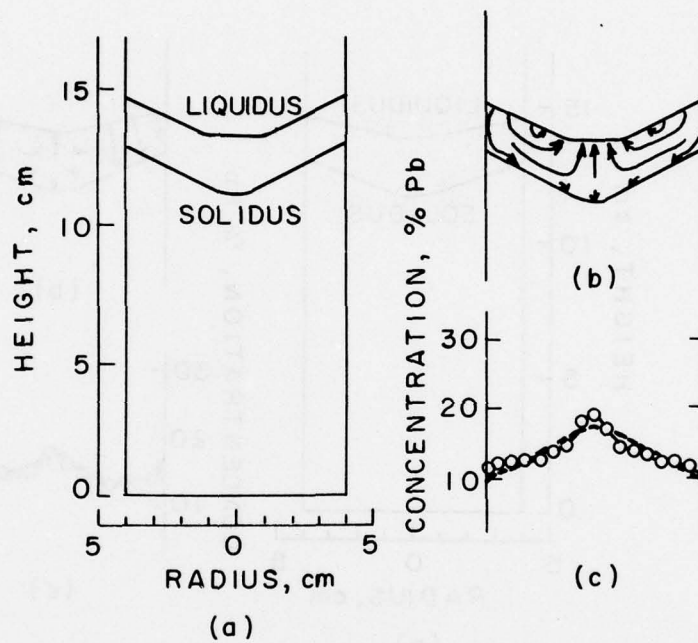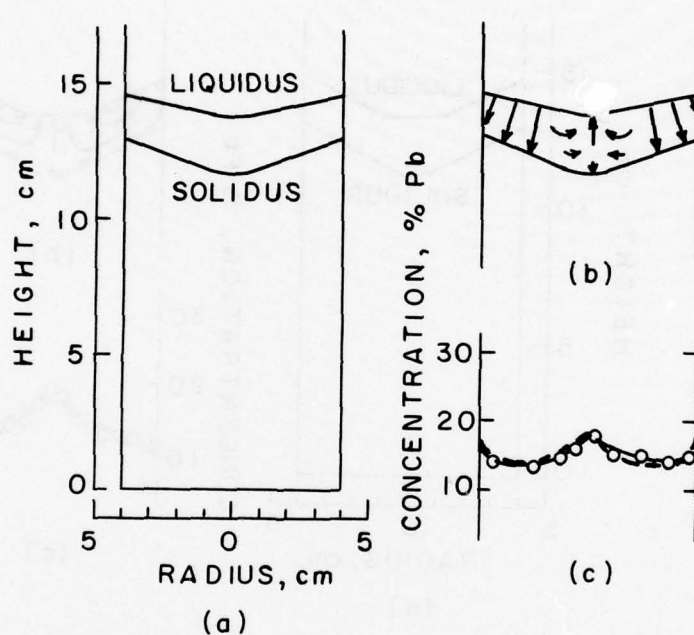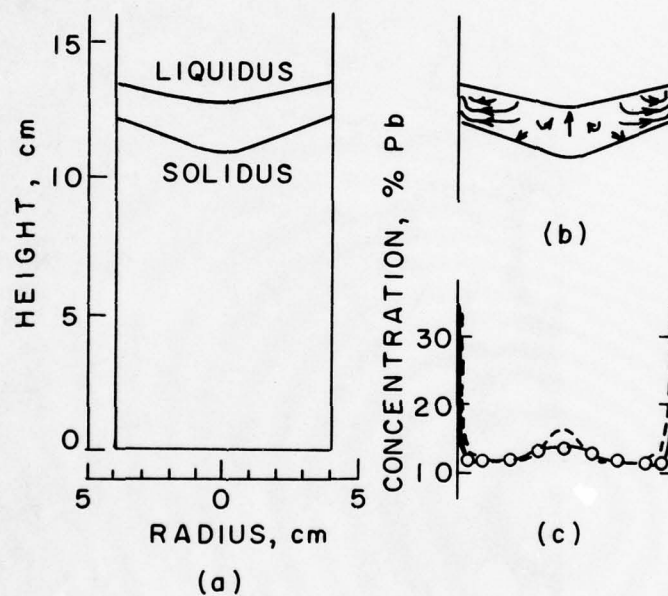
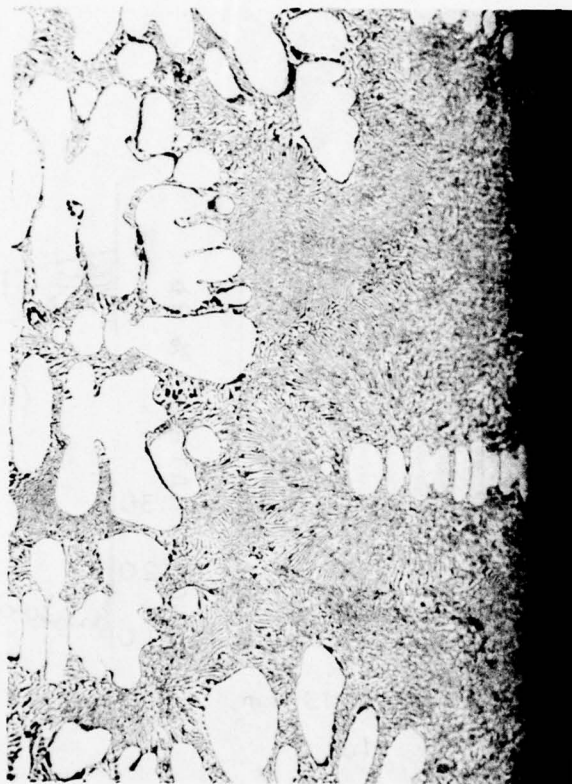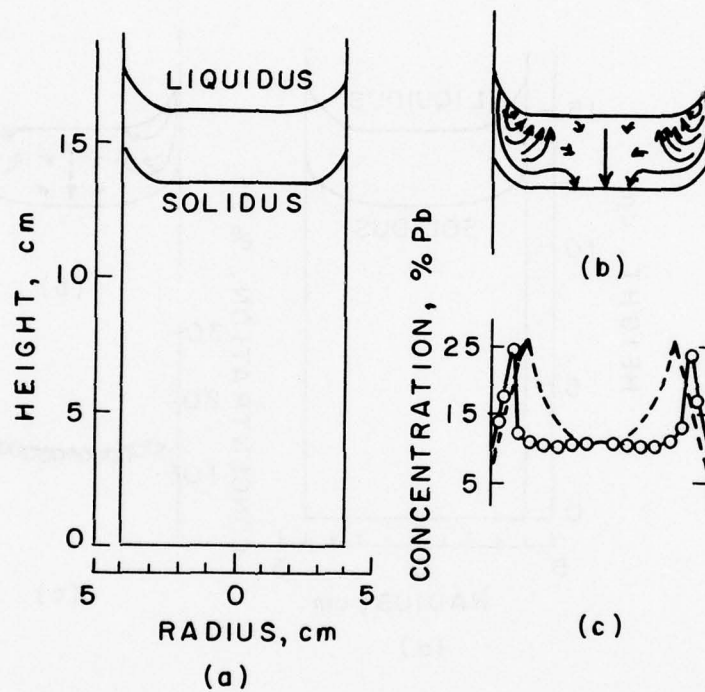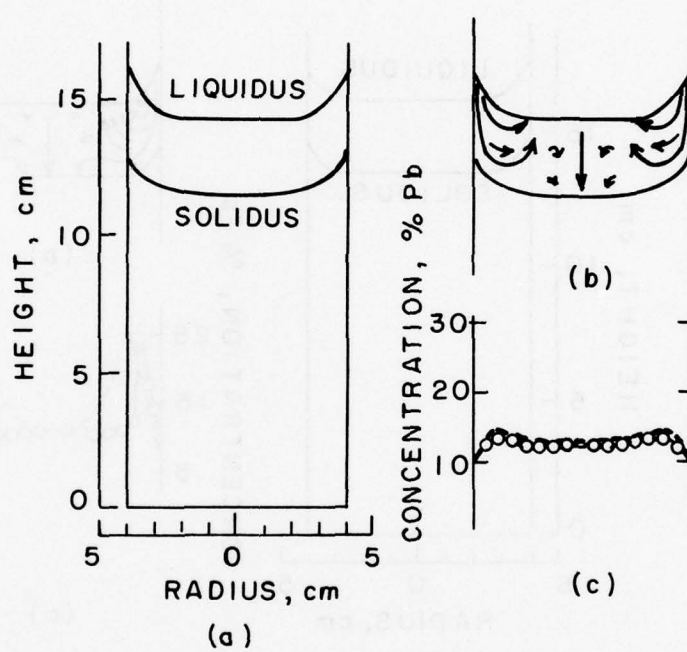Figure 3-18. Results for Ingot 12. (a) Mushy zone;
(b) calculated flow lines for inter-
dendritic liquid; (c) experimental and
calculated segregation (γ = 1.0 x 10^{-6}cm^2).
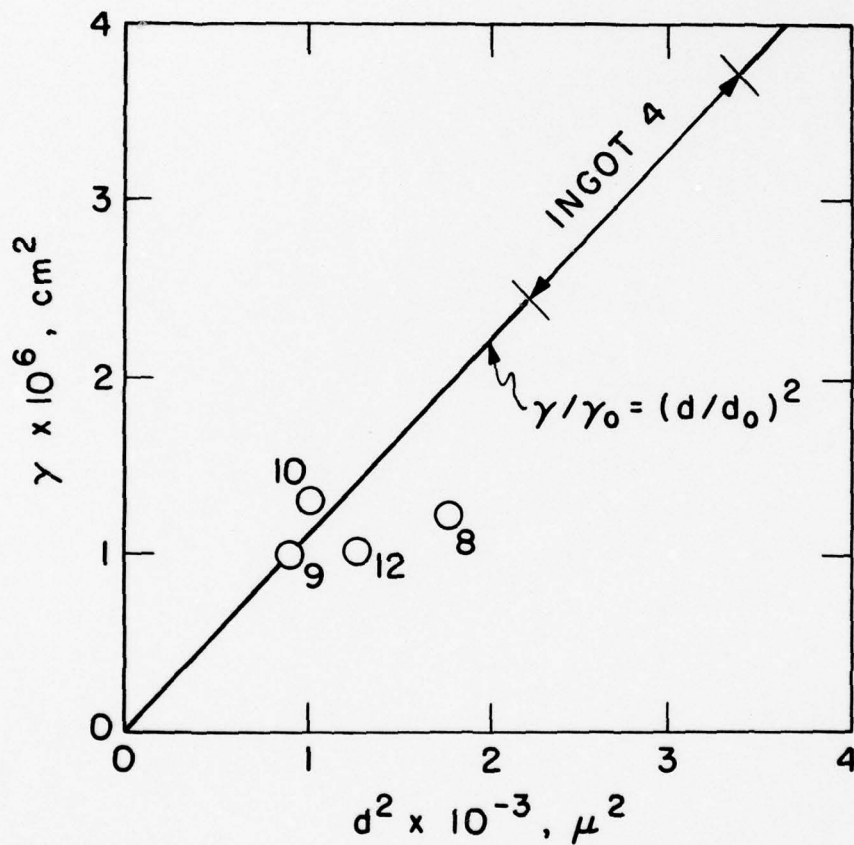
Figure 3-19. Summary of values of γ used for calculating macrosegregation.

Chapter IV

SEGREGATION IN AN ELECTROSLAG REMELTED INGOT OF MARAGING STEEL

ABSTRACT

The basic approach used to calculate macrosegregation in ESR ingots
of binary alloys is extended to treat the case of an ESR ingot of a
multicomponent maraging steel. Both calculations and experiment show very
slight segregation at the center of an ingot with a cross section
dimension of 20.3 cm by 20.3 cm.

Preliminary to the primary work on macrosegregation, results of
experiment and analysis are presented to describe the microsegregation in
maraging steel. Segregation ratios of 1.1, 1.4 and 2.9, are determined for
cobalt, nickel, and molybdenum, respectively, and the dendritic
microsegregation of these elements can be described by assuming no diffusion
in the solid during solidification and an effective partition ratios of
0.98, 0.97 and 0.80 for cobalt, nickel, and molybdenum, respectively.

MICROSEGREGATION

In order to calculate the convection of interdendritic liquid within
the mushy zone and the macrosegregation in any alloy, it is necessary to
characterize the partitioning of solutes between solid and liquid at the
solid-liquid interface during solidification. This partitioning, of
course, results in microsegregation which can be calculated when values of

equilibrium partition ratios are known. These are known for simple binaries (e.g., Pb-Sn and Al-Cu), but for multicomponent alloys (e.g., maraging steel), equilibrium partition ratios are not generally known and experimental work is necessary to determine the partition ratios of the alloy elements.

To determine the partition ratios, the approach used in this work is comprised of three steps: 1) the dendritic solidification of a sample of the alloy which is quenched from a temperature just below the solidification range so that there is no diffusion in the solid after solidification, 2) microprobe analyses to yield microsegregation profiles of the alloy elements, and 3) based upon the microsegregation profiles, the determination of the partition ratios of the alloy elements.

Experimental Approach

A small sample of maraging steel was melted in the apparatus shown in Figure 1. The apparatus was designed to study unidirectional solidification in nickel-base alloys and is described in more detail elsewhere.[1] The essential features of concern to this work are that the induction coil moves upwards at a controlled rate, the temperature is recorded by means of the thermocouple, and when the solidification front just passes the position of the thermocouple, the alumina tube and alloy are withdrawn rapidly from the hot zone so that the specimen is quenched.

A specimen, with the dimensions 5 mm diameter by 30 mm in length, was solidified at a rate of 8.33×10^{-2} mm/s under a thermal gradient of

12.1°C/mm; cooling rate during solidification was 1.01°C/s. Growth was unidirectional; a transverse section cut across primary dendrite arms is shown in Figure 2.

The microsegregation of this alloy was determined by electron-beam microprobe analysis of the area enclosed by the microhardness indentations shown in Figure 2. The electron-beam was directed across ten horizontal rows in this region in steps of two microns. The intensities of the X-rays, produced with a potential of 30 KV and beam diameter of approximately 1 - 2 microns, were corrected for absorption and fluorescence using the computer program of Cobley.[2] The data were reduced to yield the composition of each element as a function of the areal fraction viewed similar to work on microsegregation in stainless steels done by Sugiyama et al.[3] With negligible diffusion of alloy elements in the solid during solidification, such results can be viewed as a plot of the solid-interface composition versus fraction solid during solidification.

Analysis of Microsegregation

Figure 3 shows the microsegregation profiles of cobalt, molybdenum, and nickel. The alloy solidifies as a single phase with no second-phase particles (e.g., eutectic phases) forming at the end of solidification. Segregation ratios[+], therefore, are a true measure of dendritic coring; those

---

[+]The segregation ratio is a measure of the severity of microsegregation in dendritic alloys and is simply the ratio of maximum composition to minimum composition for an alloy element and is usually measured by electron beam microprobe analysis.

values are 1.1, 2.9, and 1.4 for cobalt, molybdenum and nickel, respectively.
The shape of the microsegregation profiles in Figure 3 indicates that in the
initial stages of solidification (fraction solid < 0.2), there was a solute-
rich layer in the liquid at the solid-liquid interface. Without such
enrichment, the shape of the microsegregation profiles would be as shown by
the broken curves for C_s^*.

When there is a solute-rich layer in the liquid at the solid-liquid
interface, an approximate relationship to determine interfacial composition
of solid, C_s^*, versus weight fraction solidified is[4]

$$C_s^* = kC_o(1 - f_s)^{k-1} \tag{1}$$

where C_o is the liquid composition before solidification, and k is the
effective partition ratio.[+] The effective partition ratio is defined as

$$k = C_s^*/C_L \tag{2}$$

where C_L is the composition of the interdendritic liquid outside of the thin
solute-rich layer. With a uniform composition of liquid (i.e., no solute-
rich layer), $C_L = C_L^*$ and $k = k_e = C_s^*/C_L^*$ (the equilibrium partition ratio).

For the microsegregation profiles obtained (Figure 3), a value of k
for each of the three alloy elements was determined by the least-square
method applied to the experimental results and curves generated by

_____

[+]This expression is also used to describe normal freezing of single crystals.
It does not give the initial transient, however.

equation (1) with different values of k. The value of k selected in this manner was used to calculate broken curves for the composition of solid shown in Figure 3. Also given are curves for the composition of the interdendritic liquid calculated by equation (2) with partition ratios of 0.80, 0.97, and 0.98, for Mo, Ni, and Co, respectively.

Freezing Range

The temperature during solidification is estimated by assuming that the constitutional supercooling in the interdendritic liquid is small and the change in liquidus temperature of the interdendritic liquid is related linearly to the compositional changes as follows:

$$\Delta T = \left(\frac{\partial T}{\partial C_L}\right)_{Mo} \cdot \Delta C_{L,Mo} + \left(\frac{\partial T}{\partial C_L}\right)_{Ni} \cdot \Delta C_{L,Ni} + \left(\frac{\partial T}{\partial C_L}\right)_{Co} \cdot \Delta C_{L,Co} \tag{3}$$

Here, T is temperature and C_L is subscripted according to the respective solutes. The decreases of liquidus temperature due to each alloy element are $(\partial T/\partial C_L)_{Mo} = -1.9°C/\%$, $(\partial T/\partial C_L)_{Ni} = -2.0$, and $(\partial T/\partial C_L)_{Co} = 1.7$ obtained from the respective binary phase diagrams with γ-iron[5]. Nickel is the predominant alloy element with a nominal composition of 18% so the liquidus temperature of Fe-18% Ni (1478°C) is used as a reference temperature and equation (3) becomes

$$T = 1478 - 2.0(C_{L,Ni} - 18) - 1.9C_{L,Mo} - 1.7C_{L,Co} \tag{4}$$

From Figure 3, liquid composition is known as a function of fraction solid; this information is combined with equation (4) and fraction solid of the alloy in the solidification range is thus calculated. This result is given in Figure 4, which shows a freezing range of about 19°C.

Density during Solidification

To calculate macrosegregation, the density of both phases during solidification must be evaluated. Macrosegregation results from the flow of interdendritic liquid within the mushy zone during solidification. This flow is due to solidification contraction between the liquid and solid phases and the gravity-induced flow (i.e., natural convection) which is caused by thermal and constitutional effects on liquid density.

The effect of a change in temperature and composition on the density, ρ, of the liquid is calculated by

$$\Delta\rho = (\frac{\partial\rho}{\partial T})\Delta T + (\frac{\partial\rho}{\partial C_L})_{Mo} \cdot \Delta C_{L,Mo} + (\frac{\partial\rho}{\partial C_L})_{Ni} \cdot \Delta C_{L,Ni} + (\frac{\partial\rho}{\partial C_L})_{Co} \cdot \Delta C_{L,Co} \quad (5)$$

$(\partial\rho/\partial T)$ is assumed to be that of pure liquid iron; thus $(\partial\rho/\partial T) = -1.45 \times 10^{-3}$ g/cm^3°C [6]. The effect of nickel and cobalt on the density change of the liquid phase is assumed to be equal to the values reported for these elements in their respective binary solutions with liquid iron. These data are reported by Saito[7] in the range of 1550° – 1650°C, and we assume that they apply in the solidification range. For nickel $(\partial\rho/\partial C_L)_{Ni} = 8.0 \times 10^{-3}$

g/cm^3-%, and for cobalt, $(\partial\rho/\partial C_L)_{Co} = 8.4 \times 10^{-3}$ g/cm^3-%. There are no data on the effect of molybdenum on the density of liquid iron, so we assume a linear variation of density for Fe-Mo alloys and compute that $(\partial\rho/\partial C_L)_{Mo} = 1.39 \times 10^{-2}$ g/cm^3-% using the densities of pure Mo[8] and Fe[6] at their melting points. Finally, to complete the evaluation of the terms in equation (5), we use the value of 7.02 g/cm^3 as the density of pure iron at 1550°C[6]. Then

$$\rho = 9.265 - 1.45 \times 10^{-3} T + 8.4 \times 10^{-3} \cdot C_{L,Co}$$
$$+ 8.0 \times 10^{-3} \cdot C_{L,Ni} + 1.4 \times 10^{-2} \cdot C_{L,Mo} \tag{6}$$

Since $C_{L,Co}$, $C_{L,Ni}$ and $C_{L,Mo}$ are fixed by temperature in the solidification range, then equations (4) and (6) can be combined to yield $\rho = \rho(T)$. This is shown in Figure 5.

The density of the solid phase is determined by calculation using the thermal expansion coefficient given by Touloukian[9] up to 1000°K and extrapolating that value to the solidification temperature range. The result for the density of the solid phase, ρ_s, is 7.59 cm^3/g at 1450°C. Since the solidification temperature range is only about 20°C, we assume that ρ_s is constant.

This result is shown in Figure 5 along with the result for the density of the liquid phase. From Figure 5, solidification shrinkage is about 2% at the beginning of solidification and 0.4% at the end of

solidification. Total change in density of the interdendritic liquid during
solidification is about 2% and most of that change is due to the enrichment
of molybdenum in the liquid during solidification.

STRUCTURE OF ESR INGOTS

An ESR ingot of maraging steel was cast at the laboratory of the
Army Materials and Mechanics Research Center and designated as ingot X-17.
The nominal composition of the alloy selected is 18% Ni, 9.5% Co, 4% Mo,
0.6% Ti, and 0.1% Al. The ingot has a cross-section of 20.3 cm by 20.3 cm,
with rounded corners, and a height of 43 cm. After casting, it was vacuum
annealed at 815°C and furnace cooled to allow for sectioning. Figure 6 is a
photograph of the sectioned ingot after macroetching. The ingot macrostructure
and seven tungsten "doping" marks are clearly visible. The casting speed used
was 0.0155 cm/s and was approximately constant for the upper four tungsten
marks shown in Figure 6. Each mark was made by the addition of 50 to 60 grams of
tungsten particles to the liquid metal pool in order to reveal the shape of
the liquidus isotherm at several intervals. The marks show that the liquidus
isotherm profile becomes hyperbolic in shape after the effect of the bottom
chill diminishes; this appears to be at approximately one section thickness
from the bottom.

In conjunction with the shapes of the liquidus isotherms, as revealed
by the marks in Figure 6, measurements of the secondary dendrite arm
spacings are used to calculate the shape of the mushy zone which is one of

the necessary parameters used to calculate macrosegregation. Therefore, metallographic samples were taken from the ingot in order to determine the variation of secondary dendrite arm spacing across the ingot. The result is shown in Figure 7 where it is seen that the dendrite arm spacing increases, as expected, from the surface to approximately the midspan of the ingot but then decreases unexpectedly. Apparently, the dendrite arm spacing, in the central region of the ingot, was influenced by the addition of the tungsten, most of which had settled to the center of the isotherms (Figure 6).

The liquidus isotherm of the mushy zone used for calculations is the sixth mark from the bottom in Figure 6. The position of the solidus isotherm corresponding to that liquidus is computed by first relating the secondary dendrite arm spacing, d, to local solidification time, t_f, by

$$d = A(\frac{t_f}{T_L - T_S})^n \tag{7}$$

where $T_L - T_S$ is the solidification temperature range of the alloy, and A and n are constants. Using the experimental data obtained by Joly[10] from a unidirectional ingot of maraging steel, $A = 41\mu$ and $n = 0.43$. The distance between the liquidus and the solidus is then determined by

$$Z_L - Z_S = R t_f \tag{8}$$

in which Z_L and Z_S are the positions of the liquidus and solidus isotherms, respectively, and R is the liquidus axial velocity, calculated from the ingot melt rate.

In calculating the shape of the mushy zone, it was felt that the secondary dendrite arm spacings in the central region of the ingot were unrealistic; therefore, the extrapolated values of the secondary dendrite arm spacings, shown in Figure 7, were used.+ The result of this calculation is shown in Figure 8. The two solid curves define the mushy zone used for macrosegregation calculations. Figure 8 also indicates an experimental difficulty (in addition to the effect of tungsten marking on cooling rate) which is that the intervals between marks is less than the width of the mushy zone in the central portion of the ingot.

Ten samples (in the form of drillings) for chemical analyses were taken from the maraging steel ingot. These samples were equally spaced from the surface to the center of the ingot. It is unclear what the effect of the tungsten marks is on the composition, particularly in the central region of the ingot.

Figure 9 is a plot of the alloying elements across the ingot from surface to center. Segregation is almost absent except that there is a slight decrease of composition near the center of the ingot for each element. We cannot state that this slight degree of segregation detected in the central region of the ingot would also be obtained in an unmarked ingot, since the tungsten marks do have a significant effect on solidification as discussed above.

_____

+The extrapolation corresponds to a ratio of 47.6 for the cooling rates between the surface and center of the ingot. This ratio was derived from an ESR ingot of the same size and casting rate of low alloy 4340 steel.[11]

CALCULATION OF MACROSEGREGATION

Equations (1) - (6) given in Chapter 1 of this report can be used to calculate interdendritic fluid flow and macrosegregation in an ESR ingot of a binary alloy. For a multicomponent alloy, as considered in this chapter, the equations are similar to those of Chapter 1, but, of course, there are additional terms which account for each of the alloy elements. The Appendix gives the equations used to calculate macrosegregation in the multicomponent alloy considered, herein. Density data used are from Figure 5, and Figures 3 and 4 are used to relate composition with temperature.

Calculations show that macrosegregation expected in ingot X-17 is minimal. Although surface to center compositional variations are predicted, these variations are very slight. Figure 10 shows the calculated results of molybdenum segregation for $\gamma_0 = 10^{-5}$ cm^2 and $\gamma_0 = 10^{-7}$ cm^2. For cobalt and nickel, the segregation is even less and so only the results for Mo are given.

Figure 10 shows slight positive segregation at the center of the ingot. This phenomenon was not reproduced experimentally, Figure 9, but, as mentioned, the addition of tungsten to dope the ingot significantly affected solidification in the central region of the ingot. However, we can state that in this size ingot, segregation in maraging steel is minimal at worse. This is predicted by calculation even when γ_0 is 10^{-5} cm^2 (Figure 10) which is a value selected to correspond to a highly permeable mushy zone.

CONCLUSIONS

1. The basic approach used to calculate macrosegregation in ESR ingots
   of binary alloys can be used to calculate macrosegregation in ESR
   ingots of multicomponent alloy. For multicomponent commercial
   alloys, this requires an analysis of the macrosegregation
   characteristics of the alloy. Necessary density data, which include
   the thermal and constitutional effects, are generally not known but
   must be estimated before calculations of macrosegregation can be made.

2. Macrosegregation is slight, at worse, in ESR ingots of maraging
   steel in the size studied (20 cm x 20 cm) herein. This was
   determined experimentally and by calculation.

3. The doping of steel ingots by tungsten marking to reveal pool shape
   causes experimental difficulties. Specifically, it appears that the
   amount of tungsten employed in this work significantly affects the
   dendrite arm spacing (and presumably the cooling rate) in the
   central portion of the ingot. In addition, the interval between marks
   was not great enough to exceed the width of the mushy zone along
   the center of the ingot.

4. During solidification of maraging steel, nickel and cobalt segregate
   only slightly and molybdenum segregates appreciably. Segregation
   ratios are 1.4, 1.1, and 2.9, respectively, for these elements.

5.   The microsegregation during the dendritic solidification of this
alloy results in microsegregation profiles which indicate that there
is a solute-rich liquid layer at the solid-liquid interface at least
near the beginning of freezing (fraction solid less than about 0.2).
To describe the microsegregation profiles obtained by microprobe
analyses, effective partition ratios for nickel, cobalt, and
molybdenum are 0.97, 0.98, and 0.80, respectively.

-104-

References

1. M. A. Neff, B. A. Rickinson, K. P. Young and M. C. Flemings; to be
   published in Met. Trans., 1978.

2. J. W. Cobley; "Magic IV-A Computer Program for Quantitative Electron
   Microprobe Analysis", Bell Telephone Laboratories, Allentown, Pa.

3. M. Sugiyama, T. Umeda and J. Matsuyama; Tetsu to Hagane, 1974,
   vol. 60, pp. 1094.

4. M. C. Flemings; Solidification Processing, McGraw-Hill, New York,
   1974, p. 42.

5. M. Hansen; Constitution of Binary Alloys, McGraw-Hill, New York, 1958.

6. L. D. Lucas; Compt. Rend., 1960, vol. 250, pp. 1850.

7. K. Saito et al; Senken Iko, 1969, vol. 25, pp. 67.

8. R. C. Weast; Hand Book of Chemistry and Physics, CRC Press, Cleveland,
   1976, B236.

9. Y. S. Touloukian; Thermophysical Properties of Matter, The TPRC Data
   Series, IFL/Plenum Data Company, New York, 1972, vol. 12, pp. 1183.

10. P. A. Joly, S.M. Thesis, Department of Metallurgy and Materials
    Science, Massachusetts Institute of Technology, 1971.

11. R. H. Frost, "Solidification of Electroslag Remelted Low Alloy Steel
    Ingots", AMMRC TR77-20, October, 1977.

APPENDIX

MACROSEGREGATION EQUATIONS FOR A MULTICOMPONENT ALLOY

For a differential element within the mushy zone, the continuity equation is

$$\frac{\partial}{\partial t} (\rho_S g_S + \rho_L g_L) = - \nabla \cdot \rho_L g_L \vec{v} \tag{A1}$$

where t is time, ρ_S and ρ_L are the densities of solid and liquid, g_S and g_L are the volume fraction of solid and liquid, respectively, and $\vec{v}$ is the velocity of the interdendritic liquid. The velocity of the interdendritic liquid is described by D'Arcy's law which is

$$\vec{v} = - \frac{K}{\mu g_L} (\nabla P + \rho_L \vec{g}) \tag{A2}$$

in which, K is the specific permeability of the flow space in the interdendritic interstices, μ is the liquid viscosity, P is pressure, and $\vec{g}$ is the gravitational acceleration. With $g_S + g_L = 1$ (no pore formation), constant solid density, and $K = \gamma g_L^2$, Equations (A1) and (A2) are combined to yield

$$(\rho_L - \rho_S) \frac{\partial g_L}{\partial t} + g_L \frac{\partial \rho_L}{\partial t} = \nabla \cdot (\frac{\gamma g_L^2 \rho_L}{\mu} \nabla P + \frac{\gamma g_L^2 \rho_L^2}{\mu} g) \tag{A3}$$

The composition of the interdendritic liquid for element i, C_{Li}, can be determined from its initial composition before freezing, C_{Li}^o, and its partition ratio k_i. For element j, then

$$C_{Lj} = C_{Lj}^o \left(\frac{C_{Li}}{C_{Li}^o}\right)^{\frac{1-k_j}{1-k_i}} \tag{A4}$$

We also assume that each alloy element linearly decreases the liquidus temperature of the solvent element and that the dendritic undercooling is negligible. Therefore, the composition of interdendritic liquid and temperature during freezing are related by

$$T = T_M + \sum_{j=1}^n m_j C_{Lj} \tag{A5}$$

where, $m_j = \partial T/\partial C_{Lj}$. By substituting Equation (A4) into (A5), we get that

$$T = T_M + \sum_{j=1}^n m_j C_{Lj}^o \left(\frac{C_{Li}}{C_{Li}^o}\right)^{\frac{1-k_j}{1-k_i}} \tag{A6}$$

Equation (A6) is differentiated with respect to time to obtain $\partial C_{Li}/\partial t$ which is then combined with the "local solute redistribution equation" (LSRE) for element i. The LSRE is

$$\frac{\partial C_{Li}}{\partial t} = -\left(\frac{1-k_i}{1-\beta}\right)\frac{C_{Li}}{g_L}\frac{\partial g_L}{\partial t} - \left(\frac{\vec{v} \cdot \nabla T}{\varepsilon}\right)\frac{\partial C_{Li}}{\partial t} \tag{A7}$$

where ∇T is the local temperature gradient, ε is the local cooling rate, and β is the solidification contraction. Combining Equation (A7) and the time derivative of Equation (A6) gives

$$\frac{\partial g_L}{\partial t} = -\frac{\varepsilon}{\overline{m}_i}\left(1 + \frac{\vec{v} \cdot \nabla T}{\varepsilon}\right)\left(\frac{1-\beta}{1-k_i}\right)\frac{g_L}{C_{Li}} \tag{A8}$$

where,

$$\bar{m}_i = \sum_{j=1}^{n} (\frac{C_{Lj}^{o}}{C_{Li}^{o}}) m_j (\frac{1 - k_i}{1 - k_i}) (\frac{C_{Li}}{C_{Li}^{o}})^{\frac{k_i - k_j}{1 - k_i}}$$

Equations (A2) and (A8) are then combined (with $K = \gamma g_L^2$), to arrive at

$$\frac{\partial g_L}{\partial t} = -\frac{\varepsilon}{\bar{m}_i} (\frac{1 - \beta}{1 - k_i})(1 - \frac{\gamma g_L}{\varepsilon \mu} (\nabla P + \rho_L \vec{g}) \cdot \nabla T) \frac{g_L}{C_{Li}} \tag{A9}$$

If we assume that the density of the interdendritic liquid is related to composition by

$$\rho = \rho_M + \sum_{j=1}^{n} h_j C_{Lj} \tag{A10}$$

where, $h_j = \partial \rho_L / \partial C_{Lj}$ then Equations (A4) and (A10) can be combined and differentiated with respect to time to give

$$\frac{\partial \rho}{\partial t} = \frac{\partial C_{Li}}{\partial t} \cdot \bar{h}_i \tag{A11}$$

where

$$\bar{h}_i = \sum_{j=1}^{n} h_j (\frac{C_{Li}^{o}}{C_{Li}^{o}}) (\frac{1 - k_i}{1 - k_i}) (\frac{C_{Li}}{C_{Li}^{o}})^{\frac{k_i - k_j}{1 - k_i}} \tag{A11}$$

Finally, substituting Equations (A9) and (A11) into (A3), we get

$$(\frac{\gamma g_L^2 \rho_L}{\mu} \nabla P + \frac{\gamma g_L^2 \rho_L^2}{\mu} \vec{g}) = -(\rho_L - \rho_S)(\frac{1 - \beta}{1 - k_i})(1 - \frac{\gamma g_L}{\varepsilon \mu} (\nabla P + \rho_L \vec{g}) \cdot \nabla T) \frac{g_L}{C_{Li}} \frac{\varepsilon}{\bar{m}_i}$$

$$+ g_L \bar{h}_i \frac{\varepsilon}{\bar{m}_i} \tag{A12}$$

Equation (A12) can be used to calculate the pressure distribution within the mushy zone since temperature is related directly to composition of the interdendritic liquid. Specifically in Equation (A12), the temperature gradient is

$$\nabla T = \bar{m}_i \nabla C_{Li} \tag{A13}$$

For application to a cylindrical ESR ingot, we expand Equation (A12) into cylindrical coordinates. The result is similar to Equation (6) of Chapter II except that coefficients A, B, and C have different definitions. The result is

$$\frac{\partial^2 P}{\partial r^2} + A \frac{\partial P}{\partial r} + \frac{\partial^2 P}{\partial z^2} + B \frac{\partial P}{\partial z} + C = 0 \tag{A14}$$

where,

$$A = \frac{2}{g_L} \frac{\partial g_L}{\partial r} + \frac{1}{\rho_L} \frac{\partial \rho_L}{\partial r} + \alpha_i \frac{\partial C_{Li}}{\partial r} + \frac{1}{r} \,,$$

$$B = \frac{2}{g_L} \frac{\partial g_L}{\partial z} + \frac{1}{\rho_L} \frac{\partial \rho_L}{\partial z} + \alpha_i \frac{\partial C_{Li}}{\partial z} \,,$$

$$C = g\rho_L [\frac{2}{g_L} \frac{\partial g_L}{\partial z} + \frac{2}{g_L} \frac{\partial \rho_L}{\partial z} + \alpha_i \frac{\partial C_{Li}}{\partial z}] - \frac{\mu\epsilon}{\bar{m}_i \gamma g_L} [\alpha_i + \frac{\bar{h}_i}{\rho_L}],$$

and

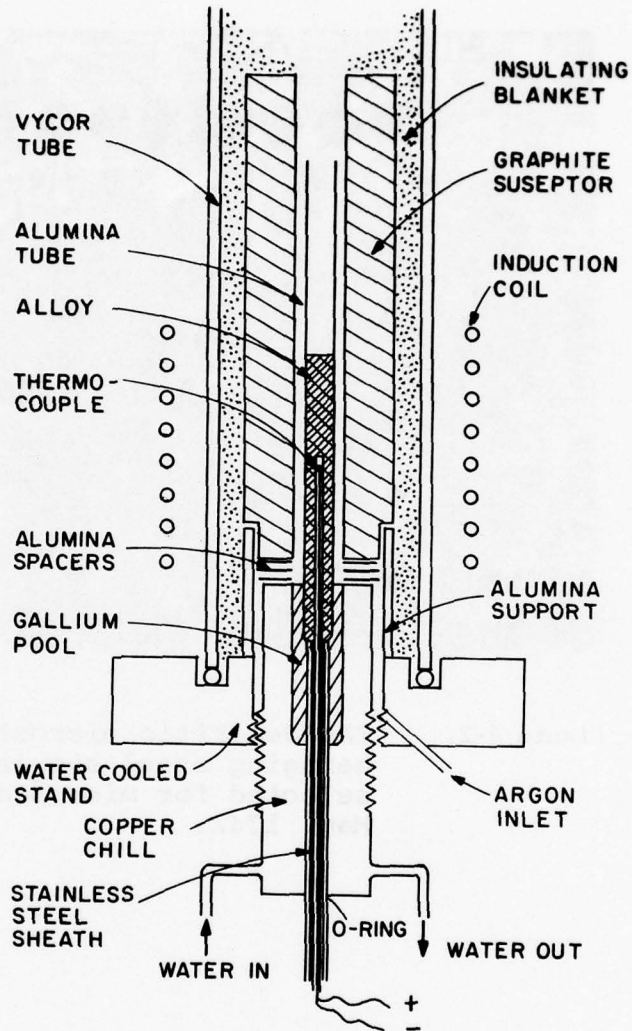$$\alpha_i = \frac{\beta}{(1 - k_i)C_{Li}}$$

Figure 4-1.   Apparatus used for obtaining
specimen for microsegregation
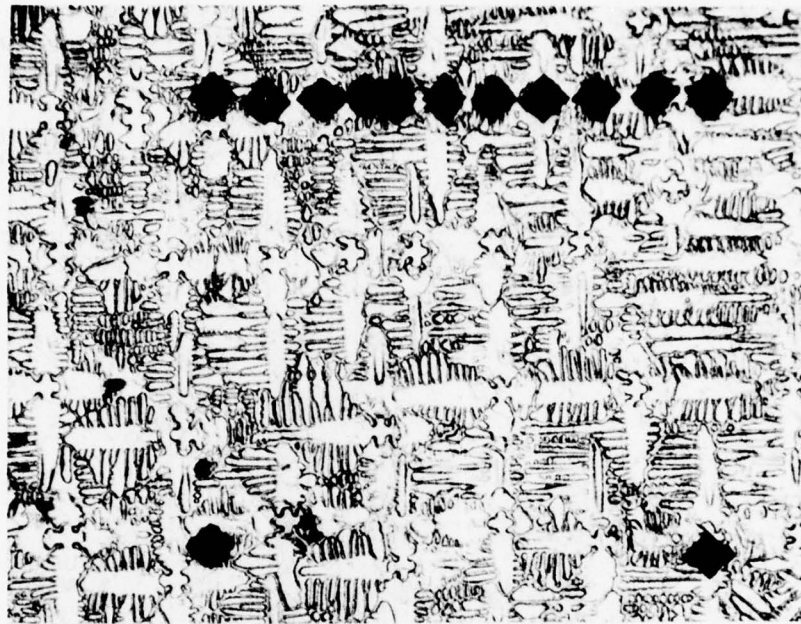analysis.

Figure 4-2.   The dendritic microstructure of
               maraging steel showing the area
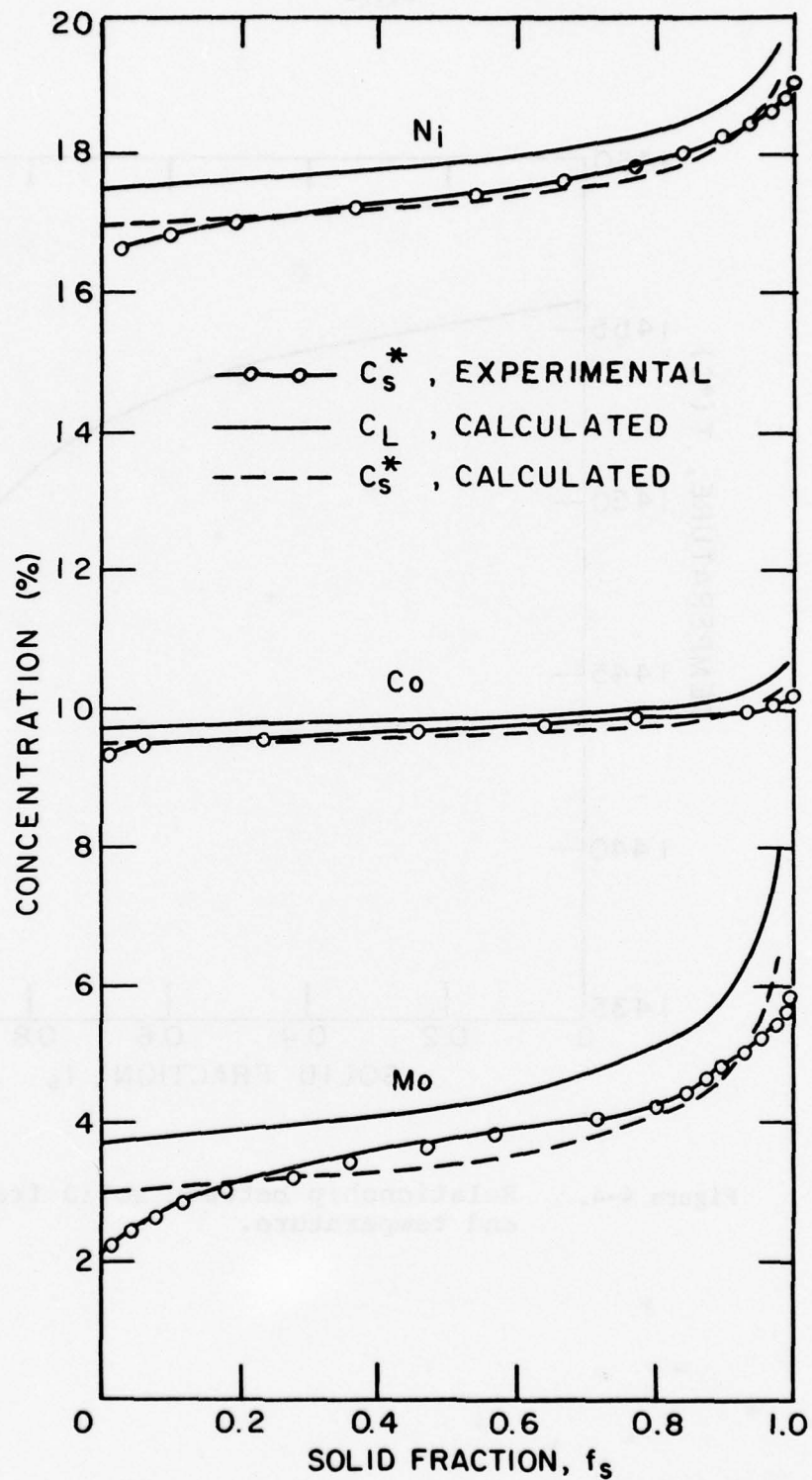   selected for microprobe analysis.
               Mag. 124X.

Figure 4-3. The compositions of the interface solid, C_s^*, and interdendritic liquid, C_L, during the solidification of maraging steel.

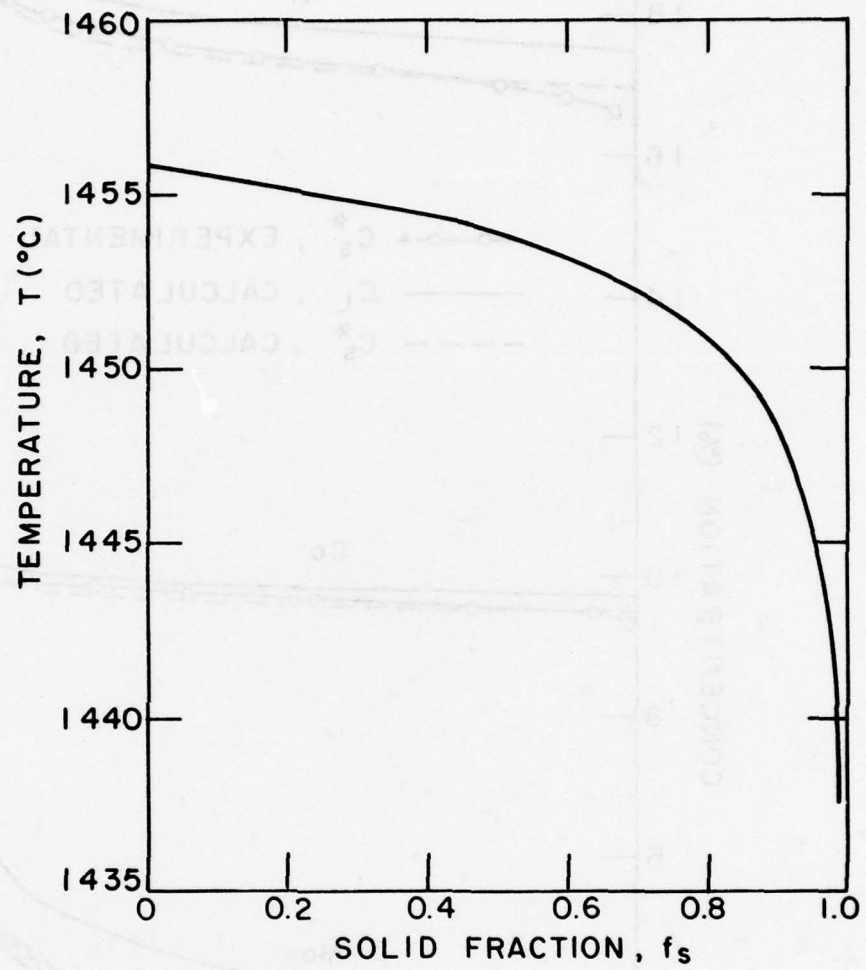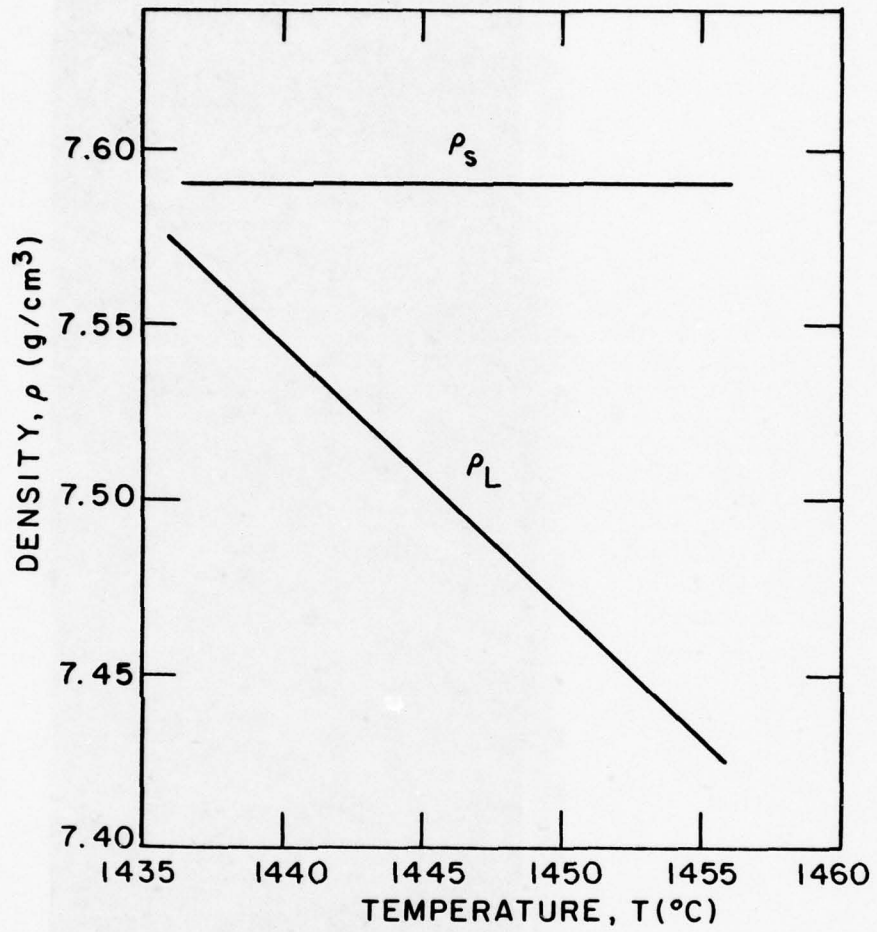Figure 4-4.   Relationship between solid fraction and temperature.

Figure 4-5.   Relationship between temperature, T, and density within the solidification range.

Figure 4-6. Macrostructure of maraging steel ingot
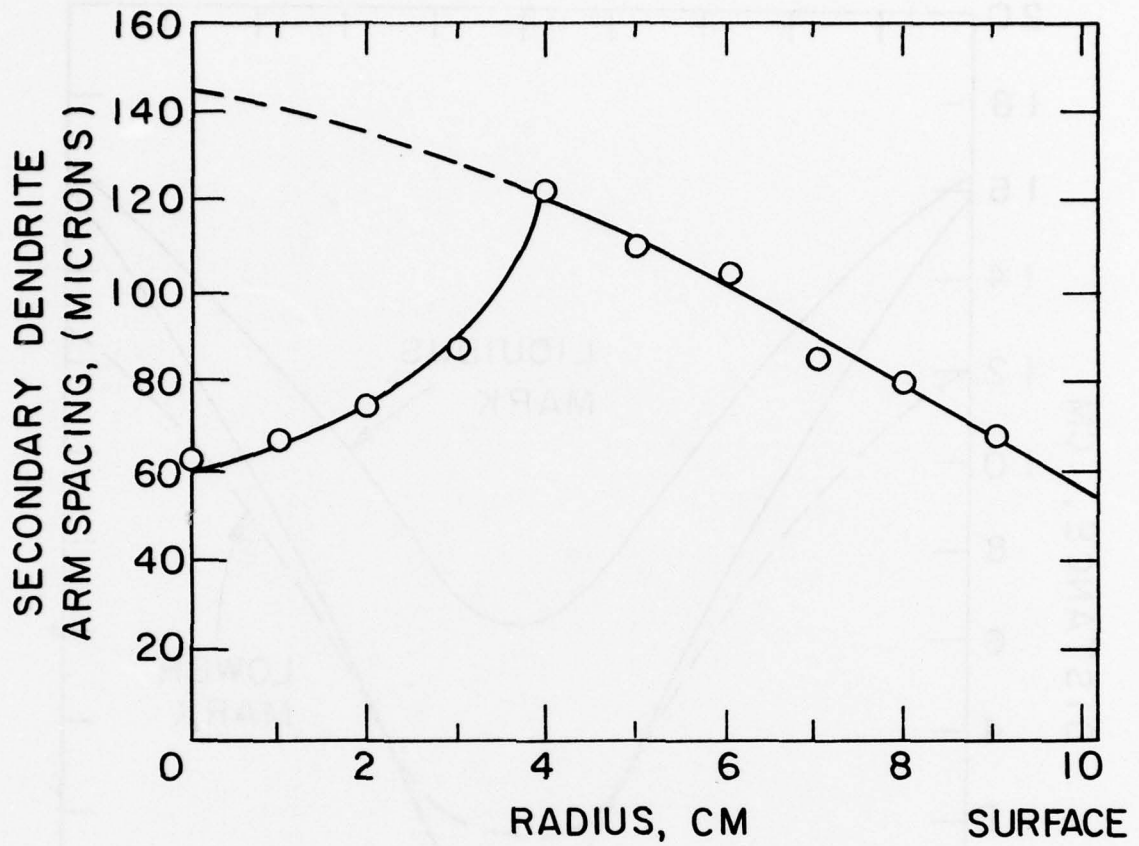(X-17) with seven tungsten doping marks.

Figure 4-7. Secondary dendrite arm spacing across the ESR ingot of maraging steel. The broken curve is extrapolated; open circles are measured values.
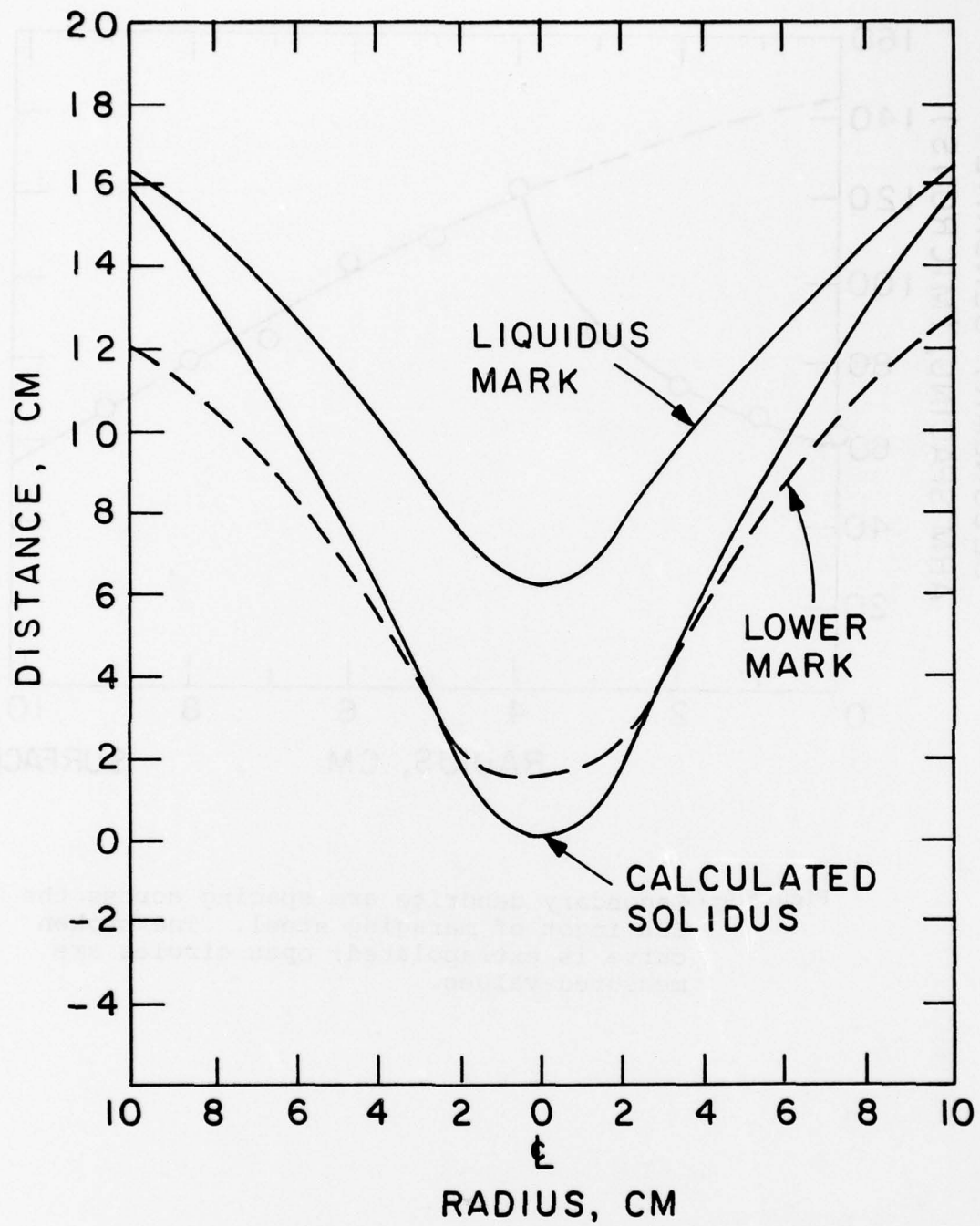
Figure 4-8. Shape of the mushy zone used for macro-
segregation calculations.
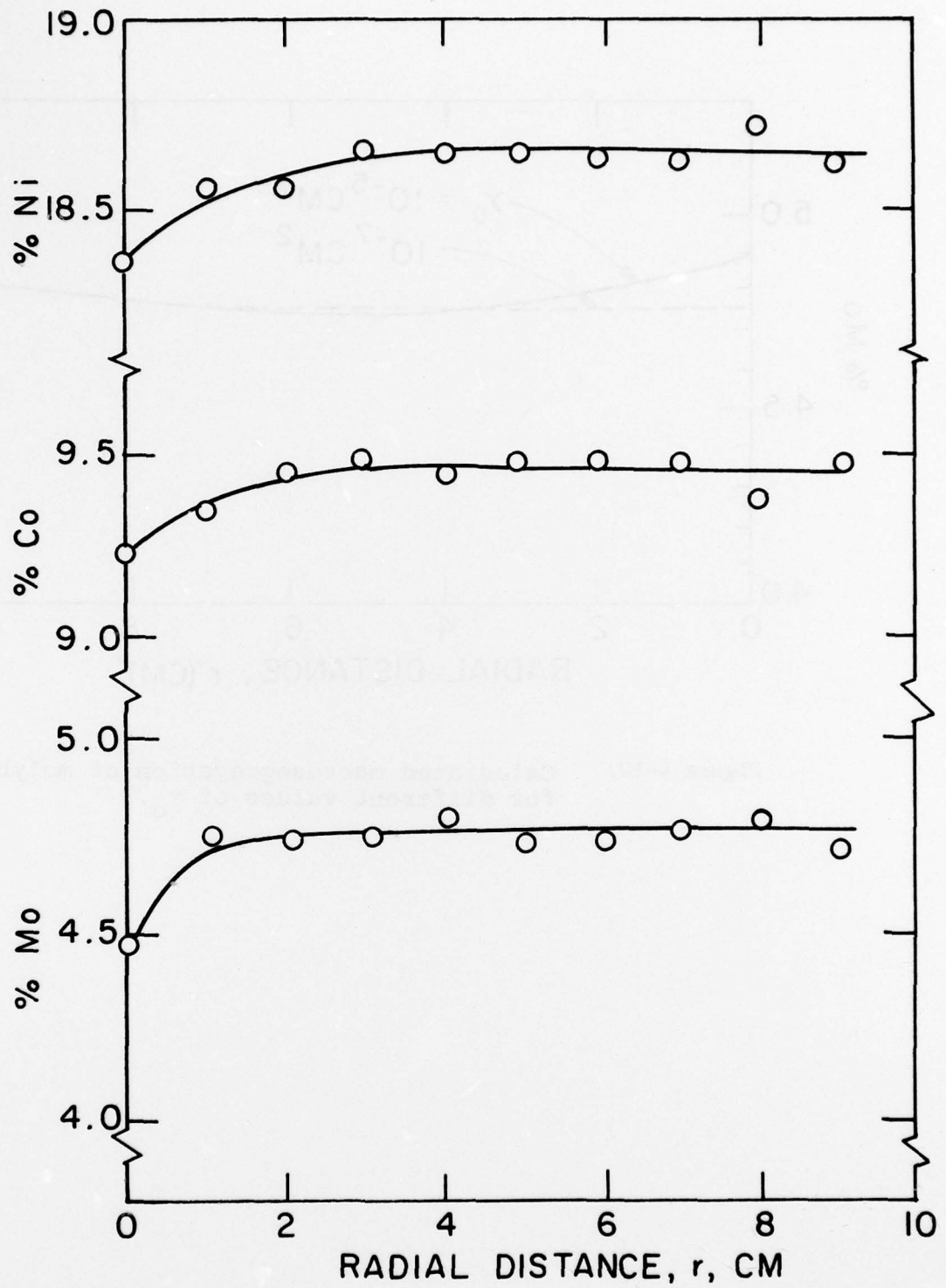
Figure 4-9.   Chemical analyses of the alloy elements
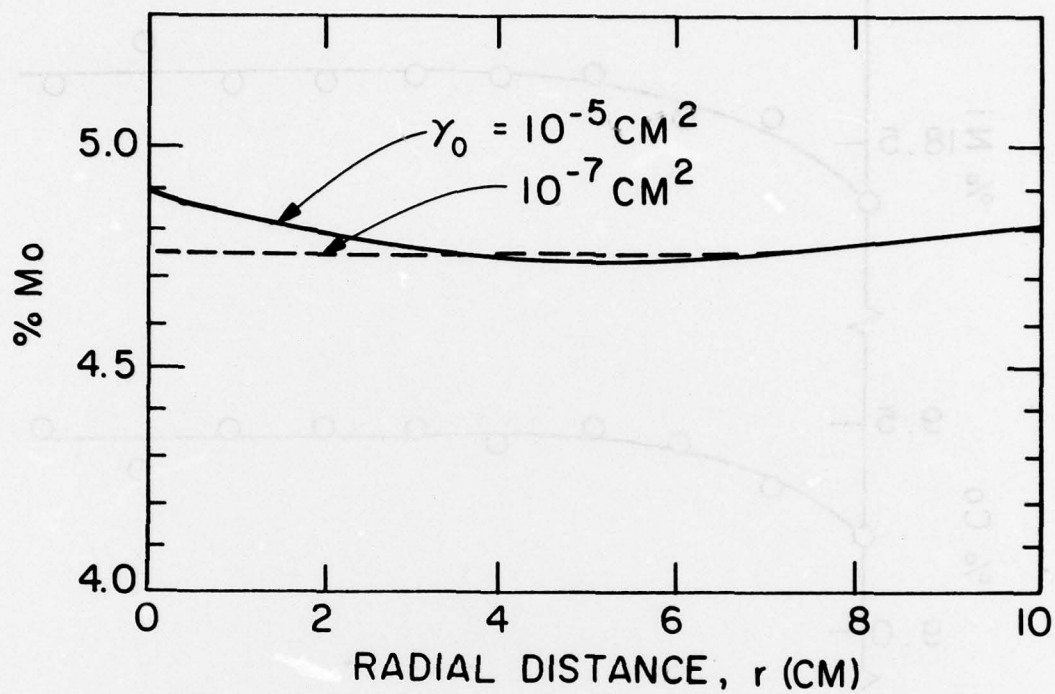   in the maraging steel ingot.

Figure 4-10.   Calculated macrosegregation of molybdenum
                for different values of γ_o.

DISTRIBUTION LIST

No. of Copies	To

1   Office of the Director, Defense Research and Engineering, The Pentagon, Washington, D. C.   20301

12   Commander, Defense Documentation Center, Cameron Station, Building 5, 5010 Duke Street, Alexandria, Virginia   22314

1   Metals and Ceramics Information Center, Battelle Columbus Laboratories, 505 King Avenue, Columbus, Ohio   43201

Office of the Deputy Chief of Staff for Research, Development, and Acquisition, Washington, D. C.   20310
2   ATTN: DAMA-ARZ

Commander, Army Research Office, P. O. Box 12211, Research Triangle Park, North Carolina   27709
1   ATTN: Information Processing Office
1   Dr. George Mayer

Commander, U. S. Army R&S Group (Eur), P. O. Box 65, FPO New York   09510
3   ATTN: Dr. R. Quattrone

Commander, U. S. Army Materiel Development and Readiness Command, 5001 Eisenhower Avenue, Alexandria, Virginia   22333
1   ATTN: DRCLDC, Mr. R. Zentner
1   DRCSA-S

Commander, U. S. Army Electronics Research and Development Command, Fort Monmouth, New Jersey   07703
1   ATTN: DRSEL-GG-DD
1   DRSEL-GG-DM
1   DRSEL-GG-E
1   DRSEL-GG-EA
1   DRSEL-GG-ES
1   DRSEL-GG-EG

Commander, U. S. Army Missile Research and Development Command, Redstone Arsenal, Alabama   35809
1   ATTN: DRDMI-ETR-LC, Dr. J. T. Davidson

Commander, U. S. Army Armament Research and Development Command, Dover, New Jersey   07801
2   ATTN: Technical Library

Commander, U. S. Army Natick Research and Development Command, Natick, Massachusetts   01760
1   ATTN: Technical Library
1   Dr. E. W. Ross
1   DRDNA-AAP, Mr. J. Falcone

1

No. of Copies	To

Commander, U. S. Army Satellite Communications Agency,
Fort Monmouth, New Jersey 07703
1 ATTN: Technical Document Center

Commander, U. S. Army Tank-Automotive Research and Development Command,
Warren, Michigan 48090
1 ATTN: DRDTA-RKA
2   DRDTA-UL, Technical Library

Commander, White Sands Missile Range, New Mexico 88002
1 ATTN: STEWS-WS-VT

Commander, Aberdeen Proving Ground, Maryland 21005
1 ATTN: STEAP-TL, Bldg. 305

Commander, U. S. Army Ballistic Research Laboratory, Aberdeen Proving
Ground, Maryland 21005
1 ATTN: Dr. J. Frasier
1   Dr. R. Vitali
1   Dr. G. L. Filbey
1   Dr. R. Karpp
1   Dr. W. Gillich

Commander, Harry Diamond Laboratories, 2800 Powder Mill Road,
Adelphi, Maryland 20783
1 ATTN: Technical Information Office

Commander, Picatinny Arsenal, Dover, New Jersey 07801
1 ATTN: SARPA-RT-S
1   Mr. A. Devine

Commander, Redstone Scientific Information Center, U. S. Army Missile
Research and Development Command, Redstone Arsenal, Alabama 35809
1 ATTN: DRDMI-TB

Commander, Watervliet Arsenal, Watervliet, New York 12189
1 ATTN: SARWV-RDT, Technical Information Services Office
1   Dr. T. Davidson
1   Mr. D. P. Kendall
1   Mr. J. F. Throop

Commander, U. S. Army Foreign Science and Technology Center,
220 7th Street, N. E., Charlottesville, Virginia 22901
1 ATTN: Mr. Marley, Military Tech

Commander, U. S. Army Aeromedical Research Unit, P. O. Box 577,
Fort Rucker, Alabama 36460
1 ATTN: Technical Library

2

Director, Eustis Directorate, U. S. Army Air Mobility Research and
Development Laboratory, Fort Eustis, Virginia 23604
1   ATTN: Mr. J. Robinson, DAVDL-E-MOS (AVRADCOM)
1   Mr. R. Berresford

U. S. Army Aviation Training Library, Fort Rucker, Alabama 36360
1   ATTN: Buildings 5906-5907

Commander, U. S. Army Agency for Aviation Safety, Fort Rucker, Alabama 36362
1   ATTN: Librarian, Building 4905

Commander, USACDC Air Defense Agency, Fort Bliss, Texas 79916
1   ATTN: Technical Library

Commander, U. S. Army Engineer School, Fort Belvoir, Virginia 22060
1   ATTN: Library

Commander, U. S. Army Engineer Waterways Experiment Station,
Vicksburg, Mississippi 39180
1   ATTN: Research Center Library

Aeronautic Structures Laboratories, Naval Air Engineering Center,
Philadelphia, Pennsylvania 19112
1   ATTN: Library

Naval Air Development Center, Aero Materials Department,
Warminster, Pennsylvania 18974
1   ATTN: J. Viglione

Naval Ship Research and Development Laboratory, Annapolis, Maryland 21402
1   ATTN: Dr. H. P. Chu

Naval Underwater Systems Center, New London, Connecticut 06320
1   ATTN: R. Kasper

Naval Research Laboratory, Washington, D. C. 20375
1   ATTN: Dr. J. M. Krafft - Code 8430
1   C. D. Beachem

Chief of Naval Research, Arlington, Virginia 22217
1   ATTN: Code 471

Naval Weapons Laboratory, Washington, D. C. 20390
1   ATTN: H. W. Romine

Director, Structural Mechanics Research, Office of Naval Research,
800 North Quincy Street, Arlington, Virginia 22203
1   ATTN: Dr. N. Perrone

No. of Copies	To

1   Ship Research Committee, Maritime Transportation Research Board, National Research Council, 2101 Constitution Ave., N. W., Washington, D. C. 20418

Air Force Materials Laboratory, Wright-Patterson Air Force Base, Ohio 45433
2   ATTN: AFML/MXE/E. Morrissey
1   AFML/LC
1   AFML/LLP/D. M. Forney, Jr.
1   AFML/MBC/Stanley Schulman
1   AFML/LNC/T. J. Reinhart
1   AFFDL (FB), Dr. J. C. Halpin
1   Dr. S. Tsai
1   Dr. N. Pagano

Air Force Flight Dynamics Laboratory, Wright-Patterson Air Force Base, Ohio 45433
1   ATTN: AFFDL (FBC), C. Wallace
1   AFFDL (FBCB), G. D. Sendeckyj

National Aeronautics and Space Administration, Washington, D. C. 20546
1   ATTN: Mr. B. G. Achhammer
1   Mr. G. C. Deutsch - Code RW

National Aeronautics and Space Administration, Marshall Space Flight Center, Huntsville, Alabama 35812
1   ATTN: R. J. Schwinghamer, EH01, Director, M&P Laboratory
1   Mr. W. A. Wilson, EH41, Building 4612

National Aeronautics and Space Administration, Langley Research Center, Hampton, Virginia 23365
1   ATTN: Mr. H. F. Hardrath, Mail Stop 129
1   Mr. R. Foye, Mail Stop 188A

National Aeronautics and Space Administration, Lewis Research Center, 21000 Brookpark Road, Cleveland, Ohio 44135
1   ATTN: Mr. S. S. Manson
1   Dr. J. E. Srawley, Mail Stop 105-1
1   Mr. W. F. Brown, Jr.

Wyman-Gordon Company, Worcester, Massachusetts 01601
1   ATTN: Technical Library

Lockheed-Georgia Company, 86 South Cobb Drive, Marietta, Georgia 30063
1   ATTN: Materials & Processes Engrg. Dept. 71-11, Zone 54

National Bureau of Standards, U. S. Department of Commerce, Washington, D. C. 20234
1   ATTN: Mr. J. A. Bennett

1   Mr. W. F. Anderson, Atomics International, Canoga Park, California 91303

Midwest Research Institute, 425 Coker Boulevard, Kansas City, Missouri 64110
1 ATTN: Mr. C. Q. Bowles
1   Mr. J. C. Grosskreutz

1 Mr. A. Hurlich, General Dynamics Convair, Mail Zone 572-00,
   P. O. Box 1128, San Diego, California 92112

Virginia Polytechnic Institute and State University, Dept. of Engineering
Mechanics, 230 Norris Hall, Blacksburg, Virginia 24061
1 ATTN: Prof. R. M. Barker
1   Assoc. Prof. G. W. Swift

Southwest Research Institute, 8500 Culebra Road, San Antonio, Texas 78284
1 ATTN: Mr. G. C. Grimes

IIT Research Institute, Chicago, Illinois 60616
1 ATTN: Dr. I. M. Daniel

1 Dr. R. E. Johnson, Mgr., Mechanics of Materials-AEG, Mail Drop M88,
   General Electric Company, Cincinnati, Ohio 45215

1 Mr. J. G. Kaufman, Alcoa Research Laboratories, New Kensington,
   Pennsylvania 15068

1 Dr. L. Kaufman, MANLABS, 21 Erie Street, Cambridge, Massachusetts 02139

1 Mr. P. N. Randall, TRW Systems Group — 0-1/2210, One Space Park,
   Redondo Beach, California 90278

TRW Equipment, TRW Inc., 23555 Euclid Avenue, Cleveland, Ohio 44117
1 ATTN: Dr. E. A. Steigerwald, T/M-3296
1   Mr. J. A. Alexander

1 Dr. I. S. Tuba, Basic Technology, Inc., 7125 Saltsburg Road,
   Pittsburgh, Pennsylvania 15235

1 Mr. B. M. Wundt, 2346 Shirl Lane, Schenectady, New York 12309

1 Mr. W. A. Van der Sluys, Research Center, Babcock and Wilcox,
   Alliance, Ohio 44601

Battelle Memorial Institute, 505 King Avenue, Columbus, Ohio 43201
1 ATTN: Dr. E. Rybicki

1 Dr. K. R. Merckx, Battelle Northwest Institute, Richland, Washington 99352

General Electric Company, Schenectady, New York 12010
1 ATTN: Mr. A. J. Brothers, Materials and Processes Laboratory

5

General Electric Company, Knolls Atomic Power Laboratory, P. O. Box 1072,
Schenectady, New York   12301
1   ATTN: Mr. F. J. Mehringer

1   Mr. L. F. Coffin, General Electric Research Laboratory, P. O. Box 1088,
Schenectady, New York   12301

United States Steel Corporation, Monroeville, Pennsylvania   15146
1   ATTN: Dr. A. K. Shoemaker, Applied Research Laboratory

Westinghouse Electric Company, Pittsburgh, Pennsylvania   15235
1   ATTN: Mr. R. E. Peterson, Research Laboratories
1   Mr. E. T. Wessel, Research and Development Center

1   Mr. B. F. Langer, Westinghouse Nuclear Energy Systems, P. O. Box 355,
Pittsburgh, Pennsylvania   15230

1   Mr. M. J. Manjoine, Westinghouse Research Laboratory, Churchill Boro,
Pittsburgh, Pennsylvania   15235

Brown University, Providence, Rhode Island   02912
1   ATTN: Prof. J. R. Rice
1   Prof. W. N. Findley, Division of Engineering, Box D

Carnegie-Mellon University, Department of Mechanical Engineering,
Schenley Park, Pittsburgh, Pennsylvania   15213
1   ATTN: Dr. J. L. Swedlow

1   Prof. J. Dvorak, Chemical Engineering Department, Duke University,
Durham, North Carolina   27706

Westinghouse Electric Company, Bettis Atomic Power Laboratory,
P. O. Box 109, West Mifflin, Pennsylvania   15122
1   ATTN: Mr. M. L. Parrish

George Washington University, School of Engineering and Applied Sciences,
Washington, D. C.   20006
1   ATTN: Dr. H. Liebowitz

Lehigh University, Bethlehem, Pennsylvania   18015
1   ATTN: Prof. George R. Irwin
1   Prof. G. C. Sih
1   Prof. F. Erodgan

Massachusetts Institute of Technology, Cambridge, Massachusetts   02139
1   ATTN: Prof. T. H. H. Pian, Department of Aeronautics and Astronautics
1   Prof. F. J. McGarry
1   Prof. A. S. Argon, Room 1-312

6

1 Mr. William J. Walker, Air Force Office of Scientific Research, 1400 Wilson Boulevard, Arlington, Virginia 22209

1 Prof. R. Greif, Dept. of Mech. Eng., Tufts University, Medford, Massachusetts 02155

1 Dr. D. E. Johnson, AVCO Systems Division, Wilmington, Massachusetts 01887

1 Prof. B. Pipes, Dept. of Mech. Eng., Drexel University, Philadelphia, Pennsylvania 19104

1 Prof. A. Tetelman, Dept. of Materials Science, University of California, Los Angeles, California 90024

1 Prof. W. Goldsmith, Dept. of Mech. Eng., University of California, Berkeley, California 94700

1 Prof. A. J. McEvilly, University of Connecticut, Storrs, Connecticut 06268

1 Prof. D. Drucker, Dean of School of Engineering, University of Illinois, Champaign, Illinois 61820

University of Illinois, Urbana, Illinois 61820
1 ATTN: Prof. H. T. Corten, Dept. of Theoretical and Applied Mechanics, 212 Talbot Laboratory

1 Dr. M. L. Williams, Dean of Engineering, 240 Benedum Hall, University of Pittsburgh, Pittsburgh, Pennsylvania 15261

1 Prof. A. Kobayashi, Dept. of Mechanical Engineering, University of Washington, Seattle, Washington 98105

1 Mr. W. A. Wood, Baillieu Laboratory, University of Melbourne, Melbourne, Australia

1 Mr. Elmer Wheeler, Airesearch Manufacturing Company, 402 S. 36th Street, Phoenix, Arizona 85034

1 Mr. Charles D. Roach, U. S. Army Scientific and Technical Information Team, 6000 Frankfurt/Main, I. G. Hochhaus, Room 750, West Germany (APO 09710, NY)

1 Prof. R. Jones, Dept. of Civil Eng., Ohio State University, 206 W. 18th Avenue, Columbus, Ohio 43210

State University of New York at Stony Brook, Stony Brook, New York 11790
1 ATTN: Prof. Fu-Pen Chiang, Dept. of Mechanics

No. of Copies	To

E. I. Du Pont de Nemours and Company, Wilmington, Delaware 19898
1   ATTN: Dr. Carl Zweren, Industrial Fibers Div., Textile Fibers Dept.

Washington University, St. Louis, Missouri 63130
1   ATTN: Prof. E. M. Wu

Director, Army Materials and Mechanics Research Center,
Watertown, Massachusetts 02172
2   ATTN: DRXMR-PL
1   DRXMR-PR
1   DRXMR-X
1   DRXMR-CT
1   DRXMR-AP
1   DRXMR-E
2   DRXMR-EM
1   DRXMR-ER
1   DRXMR-D
4   Authors

UNCLASSIFIED

SECURITY CLASSIFICATION OF THIS PAGE (When Data Entered)

REPORT DOCUMENTATION PAGE		READ INSTRUCTIONS BEFORE COMPLETING FORM
1. REPORT NUMBER AMMRC TR 78-28	2. GOVT ACCESSION NO.	3. RECIPIENT'S CATALOG NUMBER
4. TITLE (and Subtitle) ELECTROSLAG REMELTING		5. TYPE OF REPORT & PERIOD COVERED Final Report, 12/1/74 11/30/77
		6. PERFORMING ORG. REPORT NUMBER
7. AUTHOR(s) D. R. Poirier, S. Kou, T. Fujii, and M. C. Flemings		8. CONTRACT OR GRANT NUMBER(s) DAAG46-74-C-0120
9. PERFORMING ORGANIZATION NAME AND ADDRESS Massachusetts Institute of Technology Cambridge, Massachusetts 02139		10. PROGRAM ELEMENT, PROJECT, TASK AREA & WORK UNIT NUMBERS D/A Project: IL162105AH84 AMCMS Code: 612105H840011 Agency Accession:
11. CONTROLLING OFFICE NAME AND ADDRESS Army Materials and Mechanics Research Center Watertown, Massachusetts 02172		12. REPORT DATE June 1978
		13. NUMBER OF PAGES 119
14. MONITORING AGENCY NAME & ADDRESS(if different from Controlling Office)		15. SECURITY CLASS. (of this report) Unclassified
		15a. DECLASSIFICATION/DOWNGRADING SCHEDULE

16. DISTRIBUTION STATEMENT (of this Report)

Approved for public release; distribution unlimited.

17. DISTRIBUTION STATEMENT (of the abstract entered in Block 20, if different from Report)

18. SUPPLEMENTARY NOTES

19. KEY WORDS (Continue on reverse side if necessary and identify by block number)

Low Alloy Steels	Electroslag Remelting (ESR)	Heat Flow
Solidification	Macrosegregation	Refining
Microstructure	Fluid Flow	

20. ABSTRACT (Continue on reverse side if necessary and identify by block number)

This report describes research on macrosegregation in ingots produced by the electroslag remelting (ESR) process. The work is on determining the severity of segregation in small experimental ingots, and comparing the segregation with calculations using macrosegregation theory.

Most experimental ingots were produced in an apparatus which simulates the solidification of an ESR ingot but does not employ slag. The unit comprises a source of melt droplets, a cooled mold, and a heat source to

DD FORM 1473 EDITION OF 1 NOV 65 IS OBSOLETE
1 JAN 73

UNCLASSIFIED
SECURITY CLASSIFICATION OF THIS PAGE (When Data Entered)

Block No. 20

ABSTRACT

simulate the heat input of the ESR process. This apparatus was also modified so that rotation occurred during ingot solidification. In these studies, ingots of Sn-15% Pb and Sn-12% Pb with a diameter of 8 cm were studied. In addition, results of experiments on an apparatus used to produce ingots of Al-4% Cu with a diameter of 7 cm are given. This apparatus consisted of a DC power source, a water-cooled mold, consumable electrodes, and a slag layer as in conventional ESR processing.

Equations for predicting flow of interdendritic liquid and macrosegregation in ESR ingots are given and used in a computer model to numerically calculate the macrosegregation. Agreement between calculations and the experimental ESR ingots of Al-Cu and Sn-Pb alloys, described above, is excellent. The influence of important parameters such as the shape and depth of the mushy zone and the local solidification time on the macro-segregation across the ESR ingots is quantitatively demonstrated. The important effect of the dimensionless group on the different types of macrosegregation observed is also discussed.

The most important finding is that the computer model can be modified to predict the effect of rotation on macrosegregation in ESR ingots and that prediction agrees with experiment.

Microsegregation theory and macrosegregation theory are applied to a multicomponent commercial steel. In this work, an ESR ingot of maraging steel of a cross-section, 20 cm x 20 cm, with rounded corners was studied.

Army Materials and Mechanics Research Center,
Watertown, Massachusetts 02172
ELECTROSLAG REMELTING
D. R. Poirier, S. Kou, T. Fujii, M. C. Flemings,
Massachusetts Institute of Technology,
Cambridge, Massachusetts 02139

AD

UNCLASSIFIED
UNLIMITED DISTRIBUTION

Key Words
Low Alloy Steels, Solidification
Microstructure, Electroslag Re-
melting, Macrosegregation, Fluid
Flow, Heat Flow, Refining

Final Report, AMMRC TR 78-28, June 1978, 119 pp.
illus-tables, Contract DAAG46-74-C-0120
D/A Project 1L162105AH84, AMCMS Code 612105H840011

This report describes research on macrosegregation in ingots produced by the electroslag remelting (ESR) process. The work is on determining the severity of segregation in small experimental ingots, and comparing the segregation with calculations using macrosegregation theory.

Most experimental ingots were produced in an apparatus which simulates the solidification of an ESR ingot but does not employ slag. The unit comprises a source of melt droplets, a cooled mold, and a heat source to simulate the heat input of the ESR process. This apparatus was also modified so that rotation occurred during ingot solidification. In these studies, ingots of Sn-15% Pb and Sn-12% Pb with a diameter of 8 cm were studied. In addition, results of experiments on an apparatus used to produce ingots of Al-4% Cu with a diameter of 7 cm are given. This apparatus consisted of a DC power source, a water-cooled mold, consumable electrodes, and a slag layer as in conventional ESR processing.

Equations for predicting flow of interdendritic liquid and macrosegregation in ESR ingots are given and used in a computer model to numerically calculate the macrosegregation. Agreement between calculations and the experimental ESR ingots of Al-Cu and Sn-Pb alloys, described above, is excellent. The influence of important parameters such as the shape and depth of the mushy zone and the local solidification time on the macrosegregation across the ESR ingots is quantitatively demonstrated. The important effect of the dimensionless group on the different types of macrosegregation observed is also discussed.

The most important finding is that the computer model can be modified to predict the effect of rotation on macrosegregation in ESR ingots and that prediction agrees with experiment.

Microsegregation theory and macrosegregation theory are applied to a multicomponent commercial steel. In this work, an ESR ingot of maraging steel of a cross-section, 20 cm x 20 cm, with rounded corners was studied.